Chapter 2E: Description of the Reanalysis Systems (Extended Version)

Chapter Leads:
Jonathon S. Wright (Tsinghua University, China)
Masatomo Fujiwara (Hokkaido University, Japan)
Craig Long (National Oceanic and Atmospheric Administration, USA)

Chapter Co-Authors:
James Anstey (Environment & Climate Change Canada, University of Victoria, Canada)
Simon Chabrillat (Royal Belgian Institute for Space Aeronomy, Belgium)
Gilbert P. Compo (University of Colorado, USA)
Rossana Dragani (European Centre for Medium-Range Weather Forecasts, UK)
Wesley Ebisuzaki (National Oceanic and Atmospheric Administration, USA)
Yayoi Harada (Japan Meteorological Agency, Japan)
Chiaki Kobayashi (Japan Meteorological Agency, Japan)
Will McCarty (National Aeronautics and Space Administration, USA)
Andrea Molod (National Aeronautics and Space Administration, USA)
Kazutoshi Onogi (Japan Meteorological Agency, Japan)
Steven Pawson (National Aeronautics and Space Administration, USA)
Adrian Simmons (European Centre for Medium-Range Weather Forecasts, UK)
David G. H. Tan (European Centre for Medium-Range Weather Forecasts, UK)
Susann Tegtmeier (GEOMAR Helmholtz Center for Ocean Research Kiel, Germany)
Krzysztof Wargan (National Aeronautics and Space Administration, USA)
Jeffrey S. Whitaker (National Oceanic and Atmospheric Administration, USA)
Cheng-Zhi Zou (National Oceanic and Atmospheric Administration, USA)

Summary

Information on key components of twelve global atmospheric reanalysis systems with output data available in 2018 is summarized, including brief descriptions of the forecast models, assimilation schemes, and observational data used in these systems. Details of the execution streams and archived data products are also provided. Tables are used extensively to facilitate comparison of different reanalysis systems, and are arranged so that readers interested in one or more systems can easily find and compare relevant information. The information in this chapter will be referred to in the interpretation of results presented in the other chapters of the S-RIP report. This chapter is not intended to provide a complete description of the reanalysis systems; readers requiring further details are encouraged to refer to the cited literature and the online documentation provided for the reanalysis systems. Condensed versions of the material in this chapter have been provided by Fujiwara et al. (2017) and in the core S-RIP report.

Table of contents

2.1 Introduction

An atmospheric reanalysis system consists of a global forecast model, input observations, and an assimilation scheme that blends input observations with short-range forecasts. These systems produce global atmospheric data that represents best estimates (analyses) of past atmospheric states. The information collected in these analyses is then propagated forward in time and space by subsequent forecasts. In this chapter, we provide summary descriptions of the key components of the twelve global atmospheric reanalysis systems listed in Table 2.1. Our descriptions of these systems are by necessity incomplete. Further details may be found in the cited literature, particularly the publications listed in Table 2.1, or in the technical documentation compiled and provided by the reanalysis centres. A list of acronyms and some key terms used in this chapter is provided in Appendix B.

Table 2.1: List of global atmospheric reanalysis systems considered in this report.

Reanalysis system	Reference	Description
ERA-40	Uppala et al. (2005)	Class: full input (extended) Centre: ECMWF Coverage: September 1957 to August 2002
ERA-Interim	Dee et al. (2011)	Class: full input (satellite era) Centre: ECMWF Coverage: January 1979 to present
ERA-20C	Poli et al. (2016)	Class: surface input (extended) Centre: ECMWF Coverage: January 1900 to December 2010 Note: A companion ensemble of AMIP-style simulations (ERA-20CM; Hersbach et al., 2015) is also available.
ERA5	forthcoming; see also the ECMWF newsletter article by Hersbach and Dee (2016)	Class: full input (extended) Centre: ECMWF Coverage: currently January 2000 to present; planned to extend backward in time to January 1979 by the end of 2018 and to January 1950 by the end of 2019.
JRA-25 / JCDAS	Onogi et al. (2007)	Class: full input (satellite era) Centre: JMA Coverage: January 1979 to January 2014 Note: January 2005 through January 2014 are from JCDAS, a real-time extension of JRA-25.

JRA-55	Kobayashi et al. (2015) Harada et al. (2016)	Class: full input (extended) Centre: JMA Coverage: January 1958 to present Note: Two ancillary products are also available, namely JRA-55C (which only assimilates conventional observational data and covers November 1972 to December 2012; see Kobayashi et al., 2014) and JRA-55AMIP (which assimilates no observational data but uses the same boundary conditions as JRA-55 and JRA-55C).
MERRA	Rienecker et al. (2011)	Class: full input (satellite era) Centre: NASA GMAO Coverage: January 1979 to February 2016
MERRA-2	Gelaro et al. (2017)	Class: full input (satellite era) Centre: NASA GMAO Coverage: January 1980 to present Note: A number of related products are available, including an AMIP ensemble (Collow et al., 2017) and output from various 'replay' simulations (e.g., Orbe et al., 2017).
R1	Kalnay et al. (1996) Kistler et al. (2001)	Class: full input (extended) Centre: NOAA/NCEP and NCAR Coverage: January 1948 to present
R2	Kanamitsu et al. (2002)	Class: full input (satellite era) Centre: NOAA/NCEP and the DOE AMIP-II project Coverage: January 1979 to present
CFSR / CFSv2	Saha et al. (2010) Saha et al. (2014)	Class: full input (satellite era) Centre: NOAA/NCEP Coverage: January 1979 to present Note: Official data coverage by CFSR (CDAS-T382) extends through December 2010; production was migrated to the CFSv2 (CDAS-T574) analysis system starting from 1 January 2011. Although it has a different horizontal resolution (Table 2.2) and includes minor changes to physical parameterizations, CFSv2 can be considered as a continuation of CFSR for most purposes.

NOAA-CIRES 20CR v2	Compo et al. (2011)	Class: surface input (extended) Centre: NOAA and the University of Colorado CIRES Coverage: November 1869 to December 2012 Note: A newer version covering 1851–2011 (20CR version 2c) has been completed and made available in 2015.

We classify reanalysis systems according to their observational inputs and temporal coverage. The three classes of reanalysis systems include "full input" systems (which assimilate surface and upper-air conventional and satellite data), "conventional input" systems (which assimilate surface and upper air conventional data but do not assimilate satellite data), and "surface input" systems (which assimilate surface data only). Some reanalysis centres also provide companion "AMIP-type" simulations, which do not assimilate any observational data and are constrained by applying observed sea surface temperatures, sea ice, and other boundary conditions on the atmospheric forecast model. We also broadly distinguish reanalyses of the "satellite era" (1979–present) from reanalyses that provide data for dates before January 1979, with the latter referred to as "extended" reanalyses.

Four reanalyses produced by ECMWF are considered: ERA-40, ERA-Interim, ERA-20C, and ERA5. ERA-40 (Uppala et al., 2005) is an extended full input reanalysis covering 45 years from September 1957 through August 2002. No satellite data were assimilated for dates prior to January 1973; ERA-40 is therefore a conventional input reanalysis from September 1957 through December 1972. ERA-40 represented an important improvement relative to the first generation of modern reanalysis systems and continues to be used in many studies that require long-term atmospheric data. ERA-Interim (Dee et al., 2011) is a full input reanalysis of the satellite era (1979–present) that applies several corrections and modifications to the system used for ERA-40. Major focus areas during the production of ERA-Interim included improving the representations of the hydrologic cycle and the stratospheric circulation relative to ERA-40, as well as improving the consistency of the reanalysis products in time. ERA5 is intended as the full input replacement for ERA-Interim, with finer resolution in time and space (see also Section 2.2 and Appendix A) and the ability to assimilate several new types of observational data (see also Section 2.4). ERA5 is the first full input reanalysis to be conducted together with an ensemble of data assimilations, which allows for a much more robust characterization of uncertainty in the analysis state. ERA5 will be an extended reanalysis covering 1950 to present. Although only outputs for recent years (2000 to present) have been released as of this writing, these products are evaluated in some chapters of the S-RIP report. We therefore document the structure of the ERA5 system in tandem with the other reanalysis systems described in this chapter, with the important caveat that some aspects of this structure may not be final. ERA-20C (Poli et al., 2016) is a surface input reanalysis of the twentieth century (1900–2010). ERA-20C directly assimilates only surface pressure and surface wind observations, and can therefore generate reanalyses of the atmospheric state that extend further backward in time. Data from ERA-20C extend up to 0.01 hPa, but the lack of upper-air observational constraints means that these data should be used with caution in the upper troposphere and above. We omit the earlier ECMWF reanalysis products FGGE (Bengtsson et al., 1982) and ERA-15 (Gibson et al., 1997), as well as recent coupled atmosphere–ocean reanalysis efforts at ECMWF using the CERA data assimilation system (Laloyaux et al., 2016; Buizza et al., 2018).

Two reanalyses produced by JMA and cooperating institutions are considered: JRA-25/JCDAS and JRA-55. JRA-25 (Onogi et al., 2007), a joint effort by JMA and CRIEPI, was the first reanalysis produced using the JMA forecast model and data assimilation system. This reanalysis originally covered 25 years from 1979 through 2004, and was extended an additional 10 years (through the end of January 2014) as JCDAS using an identical system. JRA-55 (Kobayashi et al., 2015) is an extended full input reanalysis with coverage from 1958 through the present. JRA-55 is the first reanalysis system to apply a 4D-Var data assimilation scheme (see Section 2.3) to upper-air data during the pre-satellite era (note however that ERA-20C has also used 4D-Var to assimilate surface observations during the pre-satellite era, while ERA5 is planned to extend backward in time to 1950). Along with the JRA-55 reanalysis, JMA has provided two companion products: JRA-55C (Kobayashi et al., 2014), a conventional input reanalysis that excludes satellite observations from the assimilation, and JRA-55AMIP, an ensemble of AMIP-type forecast model simulations without data assimilation. As of this writing, these companion products only extend through December 2012, although extensions to later dates are planned for both.

Two full input reanalyses produced by NASA GMAO are considered: MERRA and MERRA-2. MERRA (Rienecker et al., 2011) was conceived by NASA GMAO as a reanalysis of the satellite era (starting in January 1979), with particular focus on leveraging the large amounts of data produced by NASAs EOS satellite constellation and improving the representations of the water and energy cycles relative to earlier reanalyses. MERRA production was discontinued after February 2016. Motivated by the inability of the MERRA system to ingest some recent data types, GMAO has developed the follow-on reanalysis MERRA-2 (Gelaro et al., 2017). MERRA-2, which covers 1980–present, includes substantial upgrades to the model (Molod et al., 2015) and changes to the data assimilation system and input data (McCarty et al., 2016). Several new data sources are used that were not assimilated by MERRA, including hyperspectral radiances from IASI and CrIS, microwave radiances from ATMS, temperature and ozone profiles from Aura MLS, and GNSS-RO bending angles. One significant and unique feature of MERRA-2 is the assimilation of aerosol optical depth (AOD) observations (Randles et al., 2017; Buchard et al., 2017), with analysed aerosols fed back to the forecast model radiation scheme. An earlier NASA reanalysis (Schubert et al., 1993, 1995) covering 1980–1995 was produced by NASA's DAO (now GMAO) using the GEOS-1 data assimilation system; this reanalysis is no longer publicly available and is not included in the S-RIP intercomparison.

Four reanalyses produced by NOAA/NCEP and cooperating organizations are considered: NCEP-NCAR R1, NCEP-DOE R2, CFSR/CFSv2, and NOAA-CIRES 20CR v2. NCEP-NCAR R1 (Kalnay et al., 1996; Kistler et al., 2001) was the first modern reanalysis system with extended temporal coverage (1948–present). This system, which uses a modified 1995 version of the NCEP forecast model, remains in widespread use. NCEP-DOE R2 covers the satellite era (1979–present) using essentially the same model structure as R1, but corrects some important errors and limitations (Kanamitsu et al., 2002). More recently, NCEP has produced CFSR using a 2007 version of the NCEP Climate Forecast System model (Saha et al., 2010). CFSR contains a number of improvements relative to R1 and R2 in both the forecast model and data assimilation system, including higher horizontal and vertical resolutions, more sophisticated model physics, and the ability to assimilate satellite radiances directly (rather than temperature retrievals). CFSR also was the first coupled global reanalysis of the atmosphere–ocean–sea ice system (joined more recently by the CERA-20C and CERA-SAT reanalyses conducted at ECMWF, neither of which is described in this chapter). Production of CFSR was transitioned to a newer version of the NCEP data as-

similation system (CFSv2; Saha et al., 2014) on 1 January 2011. This transition from CFSR to CFSv2 should not be confused with the transfer of CFSv2 production from NCEP EMC to NCEP operations, which occurred at the start of April 2011. The data assimilation system used in CFSv2 has a different horizontal resolution and includes minor changes to physical parameterizations. Because CFSv2 has been touted as a continuation of CFSR, we treat CFSR and CFSv2 as a paired system in this chapter, including brief descriptions of differences between the original and updated systems where relevant. However, we note that subsequent chapters of this report document many significant differences between CFSR and CFSv2, and suggest that users of these products should be cautious when conducting studies that span the 1 January 2011 transition date (see also Section 2.5). NOAA-CIRES 20CR v2 (Compo et al., 2011) was the first extended reanalysis to span more than 100 years. Like ERA-20C, 20CR is a surface input reanalysis. Unlike ERA-20C, which uses a 4D-Var approach to assimilate both surface pressure and surface winds, 20CR uses an EnKF approach (see Section 2.3) and assimilates only surface pressure. The forecast model used in 20CR is similar in many ways to that used in CFSR, but with much coarser vertical and horizontal grids. Because of its relatively coarse vertical resolution (see Appendix A) and the lack of direct observational inputs in the upper atmosphere, output from 20CR should be used with care in the upper troposphere and above.

The influence of observational data on reanalysis products differs not only by the type of reanalysis (e.g., "full input" versus "surface input"), but also by variable (see, e.g., the variable classification proposed by Kistler et al., 2001). Atmospheric temperatures, horizontal winds, and geopotential heights are strongly influenced by the assimilation of observational data even in earlier reanalysis systems, although these variables may be determined mainly by the forecast model in regions or periods where observations are sparse or uncertain. Observational constraints on tropospheric water vapour are weaker but still influential, and some recent reanalysis systems assimilate data that establish constraints on ozone, total water, precipitation, and/or aerosol optical depth. Variables that are largely determined by the forecast model or surface boundary conditions (such as surface fluxes and tendency terms for heat, moisture, and momentum) are considered less reliable and should be used with caution and/or validated against independent estimates.

The SPARC community has particular interest in upper tropospheric and stratospheric ozone and water vapour. This chapter touches briefly on the treatment of these variables, with detailed intercomparisons deferred to Chapter 4. Many reanalysis systems simulate ozone using photochemistry schemes of varying complexity and assimilate satellite ozone retrievals during the period after 1979. Some reanalysis systems provide an ozone analysis but use a climatological ozone distribution for radiation calculations in the forecast model. Additional details regarding the treatment of ozone are provided in Table 2.11. Reanalysis estimates of stratospheric water vapour are rudimentary and often unreliable. Adjustments due to data assimilation are typically suppressed above a specified upper boundary that varies by reanalysis system, and are in several cases replaced by relaxation to a constant value or zonal mean climatology. Stratospheric air is dehydrated mainly at the tropical tropopause and transported and diffused from there, with few if any impacts from methane oxidation in the stratosphere (although some systems do attempt to represent the effects of methane oxidation; see Table 2.24 for further details).

2.2 Forecast Models

2.2.1 Summary of basic information

Table 2.2 provides a summary of key information regarding the forecast models used in each reanalysis, including the analysis system, the horizontal grid, and the number of vertical levels. The forecast models and data assimilation systems used in reanalyses are typically frozen versions of operational systems for numerical weather prediction. The atmospheric model used in a reanalysis thus often has much in common with the model used for operational numerical weather forecasting at the same forecasting centre around the time that reanalysis was started. Model names and generations are listed in the second column of Table 2.2.

Table 2.2: Basic details of the forecast models used in the reanalyses. Horizontal grid spacing is expressed in degrees for regular grids and in kilometres for reduced grids.

Reanalysis system	Model	Horizontal grid	Vertical grid
ERA-40	IFS Cycle 23r4 (2001)	N80: ~125 km (T_L159)	60 (hybrid σ-p)
ERA-Interim	IFS Cycle 31r2 (2007)	N128: ~79 km (T_L255)	60 (hybrid σ-p)
ERA-20C	IFS Cycle 38r1 (2012)	N128: ~125 km (T_L159)	91 (hybrid σ-p)
ERA5	IFS Cycle 41r2 (2016)	N320: ~31 km (T_L639)	137 (hybrid σ-p)
JRA-25 / JCDAS	JMA GSM (2004)	F80: 1.125° (T106)	40 (hybrid σ-p)
JRA-55	JMA GSM (2009)	N160: ~55 km (T_L319)	60 (hybrid σ-p)
MERRA	GEOS 5.0.2 (2008)	$(^1/_2)°$ latitude, $(^2/_3)°$ longitude	72 (hybrid σ-p)
MERRA-2	GEOS 5.12.4 (2015)	C180: ~50 km (cubed sphere)	72 (hybrid σ-p)
NCEP-NCAR R1	NCEP MRF (1995)	F47: 1.875° (T62)	28 (σ)
NCEP-DOE R2	Modified MRF (1998)	F47: 1.875° (T62)	28 (σ)
CFSR	NCEP CFS (2007)	F288: 0.3125° (T382)	64 (hybrid σ-p)
CFSv2	NCEP CFS (2011)	F440: 0.2045° (T574)	64 (hybrid σ-p)
NOAA-CIRES 20CR v2	NCEP GFS (2008)	F47: 1.875° (T62)	28 (hybrid σ-p)

The information on horizontal grids provides a rough idea of the finest horizontal scales represented by the models. We describe the horizontal grid structures of models that use spectral dynamical cores (e.g., Machenhauer, 1979) using two separate notations. All of the models considered here use spectral dynamical cores except for MERRA and MERRA-2. Regular Gaussian grids are denoted by Fn and Tk. Fn refers to a regular Gaussian grid with 2n latitude bands and (in most cases) 4n longitude bands, while Tk indicates horizontal truncation at wave number k in

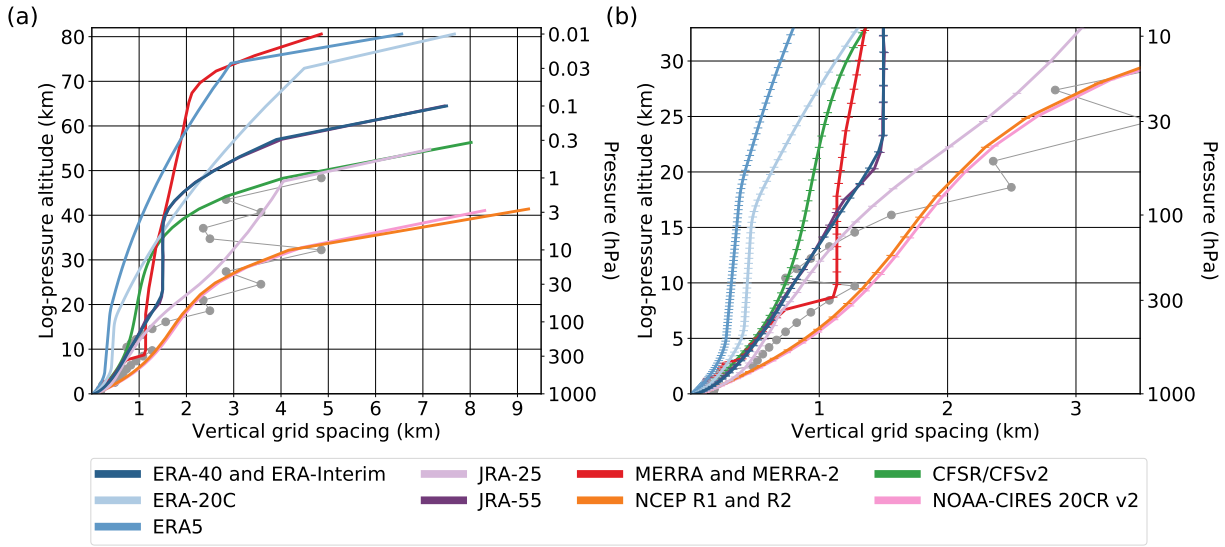

Figure 2.1: Approximate vertical resolutions of the reanalysis forecast models for (a) the full vertical range of the reanalyses and (b) the surface to 33 km (~10 hPa). Altitude and vertical grid spacing are estimated using log-pressure altitudes ($z^* = H \ln[p_0/p]$), where the surface pressure p_0 is set to 1000 hPa and the scale height H is set to 7 km. The grid spacing indicating the separation of two levels is plotted at the altitude of the upper of the two levels, so that the highest altitude shown in (a) indicates the height of the top level. Some reanalyses use identical vertical resolutions; these systems are listed together in the legend. Other reanalyses have very similar vertical resolutions when compared with other systems, including JRA-55 (similar but not identical to ERA-40 and ERA-Interim) and 20CR (similar but not identical to R1 and R2). Approximate vertical spacing associated with the isobaric levels on which ERA-40 and ERA-Interim reanalysis products are provided (grey discs) is shown in both panels for context.

the spectral dynamical core. The longitude grid spacing in a standard Fn regular Gaussian grid is $90°/n$, so that the geographical distance between neighbouring grid cells in the east–west direction shrinks toward the poles. R1, R2, and 20CR use modified regular Gaussian grids with $4(n + 1)$ longitude bands and longitude spacings of $90°/(n + 1)$. Linear reduced Gaussian grids (Hortal and Simmons, 1991; Courtier et al., 1994) are denoted by Nn and $\mathrm{T_L}k$, where the latter again indicates truncation at horizontal wave number k. The number of latitude bands in the Nn reduced Gaussian grid is also $2n$, but the number of longitudes per latitude circle decreases from the equator (where it is $4n$) toward the poles. Longitude grid spacing in reduced Gaussian grids is therefore quasi-regular in distance rather than degrees (Table 2.2). More details on Gaussian grids are available at https://software.ecmwf.int/wiki/display/FCST/Gaussian+grids (accessed August 2018). Unlike the other reanalysis systems discussed in this chapter, the MERRA and MERRA-2 atmospheric models use finite volume dynamical cores. MERRA applied this dynamical core on a regular latitude–longitude grid (Lin, 2004), while MERRA-2 uses a cubed-sphere grid (Putman and Lin, 2007). The latter type of grid is denoted by Cn, following a similar convention as Fn and Nn (i.e., approximately $4n$ longitude bands along the equator).

Table 2.3 lists the vertical locations of the model tops and describes special treatments applied in the uppermost layers of each model. Common special treatments include the use of a diffusive 'sponge layer' near the model top. Sponge layers mitigate the effects of the finite 'lid height' that

must be assumed in numerical models of the atmosphere. The application of enhanced diffusion in a sponge layer damps upward propagating waves as they near the model top, thereby preventing unphysical reflection of wave energy at the model top that would in turn introduce unrealistic resonance in the model atmosphere (Lindzen et al., 1968). It is worth noting, however, that diabatic heating and momentum transfer associated with the absorption of wave energy by sponge layers and other simplified representations of momentum damping (such as Rayleigh friction; see, e.g., Holton and Wehrbein, 1980) may still introduce spurious behaviour in model representations of middle atmospheric dynamics (Shepherd et al., 1996; Shepherd and Shaw, 2004). Most of the forecast models used by reanalysis systems include a sponge layer, but the formulation of this layer varies.

Table 2.3: Model top levels and special dynamical treatments applied in the uppermost model levels.

Reanalysis system	Top level	Special treatment of uppermost levels
ERA-40	0.1 hPa	A sponge layer is applied at pressures less than 10 hPa by adding an additional function to the horizontal diffusion terms. This function, which varies with wavenumber and model level, acts as an effective absorber of vertically-propagating gravity waves. Rayleigh friction is also implemented at pressures less than 10 hPa.
ERA-Interim	0.1 hPa	A sponge layer is applied at pressures less than 10 hPa by adding an additional function to the horizontal diffusion terms. This function, which varies with wavenumber and model level, acts as an effective absorber of vertically-propagating gravity waves. Rayleigh friction is also implemented at pressures less than 10 hPa.
ERA-20C	0.01 hPa	A sponge layer is applied at pressures less than 10 hPa by adding an additional function to the horizontal diffusion terms. This function, which varies with wavenumber and model level, acts as an effective absorber of vertically-propagating gravity waves. An additional first order "mesospheric" sponge layer is implemented at pressures less than 1 hPa. As in ERA-40 and ERA-Interim, Rayleigh friction is still applied at pressures less than 10 hPa, but the coefficient is reduced to account for the inclusion of parameterized non-orographic gravity wave drag (Table 2.7).

ERA5	0.01 hPa	A sponge layer is applied at pressures less than 10 hPa by adding an additional function to the horizontal diffusion terms. This function, which varies with wavenumber and model level, acts as an effective absorber of vertically-propagating gravity waves. An additional first order "mesospheric" sponge layer is implemented at pressures less than 1 hPa. Unlike previous ECMWF reanalyses, Rayleigh friction is not applied at pressures less than 10 hPa.
JRA-25 / JCDAS	0.4 hPa	A sponge layer is applied by gradually enhancing horizontal diffusion coefficients with increasing height at pressures less than 100 hPa. Rayleigh damping is applied to temperature deviations from the global average on each of the highest three layers.
JRA-55	0.1 hPa	A sponge layer is applied by gradually enhancing horizontal diffusion coefficients with increasing height at pressures less than 100 hPa. Rayleigh friction is implemented at pressures less than 50 hPa.
MERRA	0.01 hPa	A sponge layer consisting of the nine uppermost model levels (pressures less than ~0.24 hPa) is implemented by increasing the horizontal divergence damping coefficient (see also Table 2.8). Advection at the top model level is reduced to first order.
MERRA-2	0.01 hPa	A sponge layer consisting of the nine uppermost model levels (pressures less than ~0.24 hPa) is implemented by increasing the horizontal divergence damping coefficient (see also Table 2.8). Advection at the top model level is reduced to first order.
NCEP-NCAR R1	3 hPa	No sponge layer or other special treatment.
NCEP-DOE R2	3 hPa	No sponge layer or other special treatment.
CFSR / CFSv2	~0.266 hPa	Linear Rayleigh damping with a time scale of 5 days is applied at pressures less than ~2 hPa. The horizontal diffusion coefficient also increases with scale height throughout the atmosphere.
NOAA-CIRES 20CR v2	~2.511 hPa	No sponge layer or other special treatment.

All of the reanalysis systems discussed in this chapter use hybrid σ-p vertical coordinates (Simmons and Burridge, 1981), with the exception of NCEP-NCAR R1 and NCEP-DOE R2, which use σ vertical coordinates. The number of vertical levels ranges from 28 (R1, R2, and 20CR) to 137 (ERA5), and top levels range from 3 hPa (R1 and R2) to 0.01 hPa (MERRA, MERRA-2, ERA-

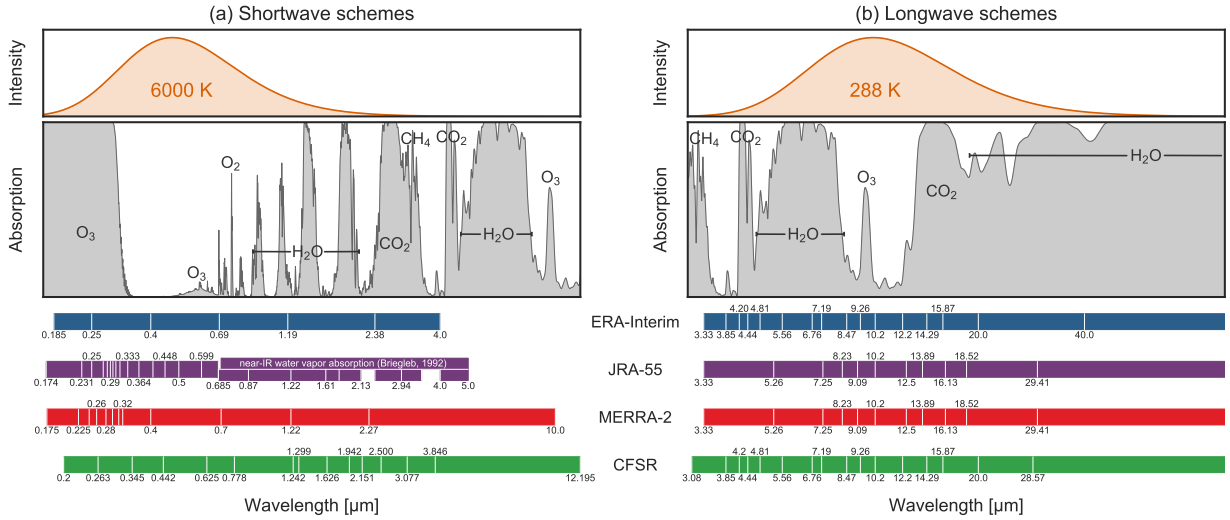

Figure 2.2: Spectral bands for the (a) shortwave (axis range: 0.17–12.2 μm) and (b) longwave (3–100 μm) broadband radiation schemes used in the forecast model components of four recent reanalyses. Note that the wavelength ranges for the shortwave and longwave schemes overlap in the near-IR and IR (3~12 μm). Normalized emission intensities as a function of wavelength for black body emission at temperatures of 6000 K and 255 K are shown in the top row for context, along with column absorptivity by CH_4, CO_2, H_2O, N_2O, O_2, and O_3 in Earth's atmosphere (middle row) approximated using the HITRAN molecular absorption database. Spectral coverage of the uppermost bands in the longwave models extends beyond 100 μm to 400 μm (JRA-55 and MERRA-2) or 1000μm (CFSR and ERA-Interim).

20C, and ERA5). Figure 2.1 shows approximate vertical resolutions for the reanalysis systems in log-pressure altitude, assuming a scale height of 7 km and a surface pressure of 1000 hPa. A number of key differences are evident, including large discrepancies in the height of the top level (Figure 2.1a) and variations in vertical resolution through the upper troposphere and lower stratosphere (Figure 2.1b). These model grids differ from the isobaric levels on which many reanalysis products are provided. Vertical spacing associated with an example set of these isobaric levels (corresponding to ERA-40 and ERA-Interim) is included in Figure 2.1 for context. See Appendix A for lists of model levels and further details of the vertical grids.

2.2.2 Major physical parameterizations

In this section we briefly describe some influential physical parameterizations used in the reanalysis forecast models, including those for longwave and shortwave radiation (Table 2.4), clouds and convection (Tables 2.5 and 2.6), gravity wave drag (Table 2.7), and aspects related to horizontal and vertical diffusion (Tables 2.8 and 2.9). Some of the effects of differences in these parameterizations are explored in the later chapters of this report. Other pertinent details include the treatment of incoming solar radiation, surface boundary conditions, and radiatively active gases and aerosols, which are summarized in section 2.2.3 (see also references in Table 2.1), as well as representations of land surface properties, which are described in section 2.2.4.

The radiative parameterizations used in the forecast model components of reanalysis systems are broadband schemes, in which the radiative spectrum is discretized into a discrete set of spectral bands. The form of this discretization is dictated primarily by the presence of radiatively active

constituents in the atmosphere and the wavelengths at which these constituents are active (Figure 2.2). Each band may feature parameterizations of radiative transfer due to multiple species, as well as scattering, absorption, and emission by clouds or aerosols. Radiative fluxes and heating rates (defined as the convergence of radiative fluxes) are computed by integrating across all spectral bands. Note that the radiative transfer schemes used in the forecast models (Table 2.4) differ from the radiative transfer schemes used to process satellite radiances for data assimilation (Table 2.19).

Most of the reanalysis systems assume maximum–random overlap for clouds during radiation calculations. Under this assumption, cloud layers that are contiguous in the vertical are assumed to have maximal overlap, while cloud layers that are not contiguous in the vertical coordinate are assumed to overlap randomly. Some earlier reanalysis systems (NCEP-NCAR R1 and NCEP-DOE R2) assume random overlap for all cloud layers regardless of the vertical distribution, while JRA-25 and JRA-55 assume maximum–random overlap for longwave radiation but random overlap for shortwave radiation. Several recent reanalysis systems, such as ERA-20C, ERA5, and CFSv2 (but notably not CFSR), use the McICA approach (e.g., Pincus et al., 2003; Morcrette et al., 2008; Saha et al., 2014) to represent interactions between radiation and clouds. Note that there are different ways to apply McICA. The implementation in CFSv2 uses a relatively simple maximum–random overlap assumption, while that in the recent ECMWF reanalyses uses a generalized overlap (e.g., Collins, 2001) with prescribed decorrelation lengths for cloud cover and cloud water content. Other potential sources of differences in radiative transfer beyond those documented here include representations of surface or cloud emissivity, assumptions regarding the optical properties of clouds and aerosols, and parameterizations of radiative transfer within each specified band. Although these aspects of the radiative paramaterizations are not described in detail here, additional information on representations of radiatively active constituents is provided in Table 2.5 (clouds), Table 2.11 (ozone), Table 2.12 (aerosols), Table 2.13 (trace gases), and Table 2.24 (water vapor).

Table 2.4: Radiative transfer schemes used in the forecast models of the reanalysis systems.

ERA-40	Shortwave: Fouquart and Bonnel (1980) with four spectral bands covering 0.2–4.0 μm Longwave: RRTM-G (Mlawer et al., 1997); 16 spectral bands covering 3.33–1000 μm Implementation: Radiation calculations are performed every 3 h on a T63 horizontal grid.
ERA-Interim	Shortwave: updated version of Fouquart and Bonnel (1980) with six spectral bands covering 0.2–4.0 μm Longwave: RRTM-G (Mlawer et al., 1997); 16 spectral bands covering 3.33–1000 μm Implementation: The scheme is a revised version of that used in ERA-40 with hourly radiation calculations on a T95 horizontal grid (Dee et al., 2011).

ERA-20C	Shortwave: updated RRTM-G (Mlawer et al., 1997; Iacono et al., 2008); 14 spectral bands covering 0.2–12.195 μm Longwave: updated RRTM-G (Mlawer et al., 1997; Iacono et al., 2008); 16 spectral bands covering 3.08–1000 μm Implementation: Radiation calculations are performed every 3 h on a T63 horizontal grid. A McICA approach with generalized overlap is used to represent the radiative effects of clouds (Morcrette et al., 2008).
ERA5	Shortwave: updated RRTM-G (Mlawer et al., 1997; Iacono et al., 2008); 14 spectral intervals covering 0.2–12.195 μm Longwave: updated RRTM-G (Mlawer et al., 1997; Iacono et al., 2008); 16 spectral intervals covering 3.08–1000 μm Implementation: Radiation calculations are performed hourly on a T319 horizontal grid. A McICA approach with generalized overlap is used to represent the radiative effects of clouds (Morcrette et al., 2008).
JRA-25 / JCDAS	Shortwave: Briegleb (1992), with nine spectral bands covering 0.2–5.0 μm Longwave: line absorption based on the random band model of Goody (1952), with four spectral bands covering 4.55–400 μm Implementation: Radiation calculations are performed on the full model grid, with calculations hourly for shortwave radiation and every 3 h for longwave radiation.
JRA-55	Shortwave: Briegleb (1992), updated to use the formulation of Freidenreich and Ramaswamy (1999) for shortwave absorption by O_2, O_3, and CO_2; 16 spectral bands covering 0.174–5.0 μm Longwave: Murai et al. (2005); 11 spectral bands covering 3.33–400 μm Implementation: Radiation calculations are performed on the full model grid, with calculations hourly for shortwave radiation and every 3 h for longwave radiation.
MERRA	Shortwave: CLIRAD (Chou and Suarez, 1999), with 10 spectral bands covering 0.175–10.0 μm Longwave: CLIRAD (Chou et al., 2001); 11 spectral bands covering 3.33–400 μm Implementation: Radiation calculations are performed hourly on the full model grid.
MERRA-2	Shortwave: CLIRAD (Chou and Suarez, 1999), with 10 spectral bands covering 0.175–10.0 μm Longwave: CLIRAD (Chou et al., 2001); 11 spectral bands covering 3.33–400 μm Implementation: Radiation calculations are performed hourly on the full model grid.

NCEP-NCAR R1	Shortwave: GFDL (Lacis and Hansen, 1974), with parameterized absorption of solar radiation by ozone, water vapor, CO_2, and clouds in a single band; known to underestimate solar radiative heating rates in the stratosphere (Freidenreich and Ramaswamy, 1993) Longwave: GFDL (Fels and Schwarzkopf, 1975; Schwarzkopf and Fels, 1991); eight spectral bands covering 4.55–1000 μm Implementation: Radiation calculations are performed every 3 h on a 128×64 linear grid.
NCEP-DOE R2	Shortwave: Chou and Lee (1996), with 10 spectral bands covering 0.175–10.0 μm Longwave: GFDL (Fels and Schwarzkopf, 1975; Schwarzkopf and Fels, 1991); eight spectral bands covering 4.55–1000 μm Implementation: Radiation calculations are performed hourly on the full model grid.
CFSR / CFSv2	Shortwave: RRTM-G (Clough et al., 2005), with 14 spectral bands covering 0.2–12.195 μm Longwave: RRTM-G (Clough et al., 2005); 16 spectral bands covering 3.08–1000 μm Implementation: Radiation calculations are performed hourly on the full model grid. A McICA approach with maximum–random overlap has been implemented in CFSv2 to represent the radiative effects of clouds, but was not used in CFSR.
NOAA-CIRES 20CR v2	Shortwave: modified RRTM-G (Clough et al., 2005), with 14 spectral bands covering 0.2–12.195 μm Longwave: modified RRTM-G (Clough et al., 2005); 16 spectral bands covering 3.08–1000 μm Implementation: Radiation calculations are performed hourly on the full model grid. The 20CR AGCM is very similar to the CFSR AGCM in most respects, including parameterizations, configuration, and treatment of radiation.

Parameterizations of stratiform or "large-scale" clouds in the reanalysis systems are briefly described in Table 2.5. These representations influence surface fluxes and the atmospheric state via couplings with radiative transfer, precipitation, and convection. The simplest parameterizations diagnose stratiform cloud cover at each time step as a function of the difference between the grid-scale relative humidity and a critical relative humidity. The existence of clouds in the model atmosphere thus depends on the relative humidity exceeding this critical threshold. NCEP-NCAR R1 and NCEP-DOE R2 use this type of "diagnostic" parameterization. Although computationally inexpensive, diagnostic cloud parameterizations have a number of intrinsic flaws (see, e.g., Xu and Krueger, 1991), and have been replaced in more recent reanalyses by variations on the "prognostic" approach pioneered by Sundqvist (1978). Prognostic parameterizations simulate the evolution of key cloud variables, such as cloud fraction, cloud water content, and precipitation, and allow for the persistence and advection of convectively-detrained anvil clouds across multiple time steps, as well as the implementation of more sophisticated approaches to simulating the autoconversion

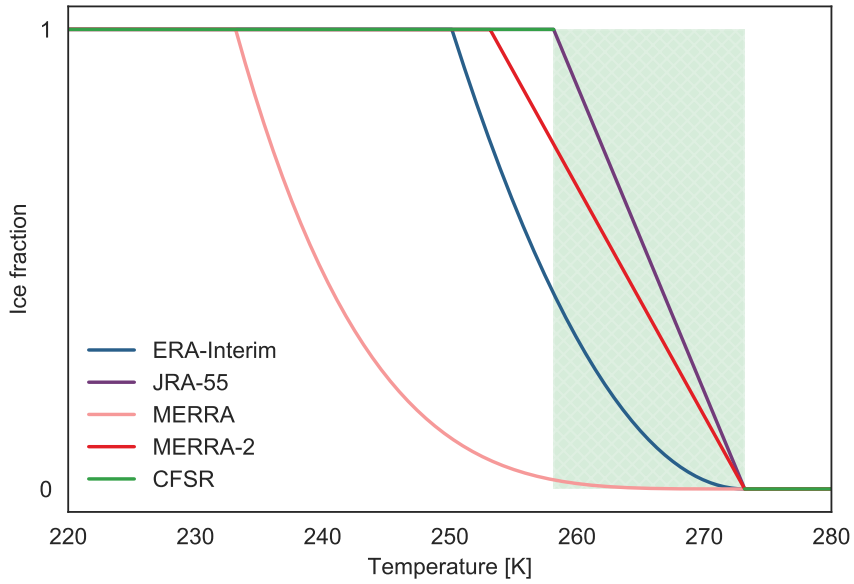

Figure 2.3: Partitioning of prognostic cloud condensate between the ice and liquid phases as a function of temperature in five recent reanalysis systems. See text for details.

of cloud condensate to rain and snow. The prognostic cloud parameterizations used in reanalyses consider two primary sources of stratiform clouds. The first of these, detrainment of cloud condensate from moist convection, depends on the formulation of the convection schemes documented in Table 2.6. The second source, in situ condensation resulting from large-scale cooling, is represented in a variety of ways. One common approach is to define a PDF that governs the subgrid-scale joint variability of total water (water vapor plus condensed water) and liquid water temperature within each grid cell. Cloud fraction and cloud water content are then calculated by integrating over the portion of this PDF that exceeds the critical relative humidity (Sommeria and Deardorff, 1977). Key uncertainties in this approach, which is used by JRA-25, JRA-55, MERRA, and MERRA-2, include the form of the PDF (Xu and Randall, 1996b) and the definition of the critical relative humidity (Molod, 2012). An alternative approach proposed by Tiedtke (1993) is based on a pair of prognostic equations that track cloud fraction and cloud water content in terms of physical sources and sinks. Versions of this parameterization are used by ERA-40, ERA-Interim, ERA-20C, and ERA5 (although there are important differences in implementation, as described in Table 2.5). CFSR and 20CR use a prognostic formulation that tracks the sources and sinks of cloud water (Zhao and Carr, 1997), and then diagnose cloud fraction as a function of cloud water content and relative humidity (Xu and Randall, 1996a).

Another potentially influential difference among the prognostic cloud schemes used in reanalysis systems is the approach to partitioning cloud condensate into ice and liquid phases (Figure 2.3), which affects both the optical properties (and hence radiative transfer) and microphysical properties (and hence autoconversion and precipitation) of the simulated clouds. As with the cloud schemes themselves, this partitioning may be either diagnostic or prognostic. JRA-25 and JRA-55 diagnose the fraction of condensate in the ice phase at every time step according to a simple linear partitioning between 0°C and −15°C. ERA-40 and ERA-Interim also use a diagnostic approach, but with a

quadratic function of temperature that ranges from entirely liquid at temperatures warmer than 0°C to entirely ice at temperatures colder than −23°C. CFSR and 20CR assume that large-scale clouds are entirely liquid at temperatures above 0°C and entirely ice at temperatures below −15°C. At temperatures between these two thresholds, CFSR and 20CR assume that all condensate is ice if ice particles existed at or above the grid cell during this or the previous time step, and assume that all condensate is liquid otherwise (Zhao and Carr, 1997). This implementation might be termed "semi-prognostic", in that it takes conditions during the previous time step into account; however, it does not allow for liquid and ice condensate to coexist in mixed-phase clouds. The implementations in MERRA and MERRA-2 are closer to fully prognostic, partitioning condensate into ice and liquid according to a quartic function of temperature between 0°C and −40°C (MERRA) or a linear function between 0°C and −20°C (MERRA-2) and then gradually converting supercooled liquid droplets to ice over time provided temperatures remain below 0°C. A more sophisticated prognostic approach is taken by ERA-20C and ERA5 (Forbes et al., 2011), in which new condensate is initialized as ice for temperatures below −38°C and liquid for temperatures above −38°C. Exchange between the ice and liquid phases then proceeds according to parameterized representations of freezing, melting, and the Wegener–Bergeron–Findeisen process for temperatures between −38°C and 0°C. A sub-timestep sequential implementation is used to prevent clouds from consisting entirely of supercooled liquid water at extremely low temperatures.

Table 2.5: Non-convective cloud parameterizations used in the reanalysis systems.

ERA-40	A prognostic cloud scheme (Tiedtke, 1993), in which cloud fraction and water content evolve according to physical sources and sinks. Ice fractions are diagnosed at each time step based on temperature (Figure 2.3). Sources due to both convective detrainment and in situ condensation are considered.
ERA-Interim	A prognostic cloud scheme (Tiedtke, 1993), in which cloud fraction and water content evolve according to physical sources and sinks. Updated from ERA-40 to include a treatment for ice supersaturation at temperatures less than 250 K (Tompkins et al., 2007). Ice fractions are diagnosed at each time step based on temperature (Figure 2.3). Sources due to both convective detrainment and in situ condensation are considered.
ERA-20C	A prognostic cloud scheme (Tiedtke, 1993), in which cloud fraction and water content evolve according to physical sources and sinks. Updated from ERA-Interim to permit separate estimates of liquid and ice water in non-convective clouds and to treat rain and snow as prognostic variables (Forbes et al., 2011). A more sophisticated prognostic representation of mixed-phase clouds is included, as opposed to the diagnostic partitioning of liquid and ice used in ERA-40 and ERA-Interim. Sources due to both convective detrainment and in situ condensation are considered.

ERA5	A prognostic cloud scheme (Tiedtke, 1993), in which cloud fraction and water content evolve according to physical sources and sinks. As in ERA-20C, the scheme permits separate estimates of liquid and ice water in non-convective clouds and treats rain and snow as prognostic variables (Forbes et al., 2011), allowing a more sophisticated prognostic representation of mixed-phase clouds relative to the diagnostic partitioning of liquid and ice used in ERA-40 and ERA-Interim. Sources due to both convective detrainment and in situ condensation are considered.
JRA-25 / JCDAS	Cloud fraction and total water content are parameterized following a modified version of the joint PDF-based approach of Smith (1990). Sources of large-scale condensate due to both convective detrainment and in situ condensation are considered. Cloud fractions for marine stratocumulus follow the separate diagnostic approach proposed by Kawai and Inoue (2006).
JRA-55	Cloud fraction and total water content are parameterized following a modified version of the joint PDF-based approach of Smith (1990). Sources of large-scale condensate due to both convective detrainment and in situ condensation are considered. Cloud fractions for marine stratocumulus follow the separate diagnostic approach proposed by Kawai and Inoue (2006).
MERRA	A prognostic scheme that tracks convectively-detrained "anvil" condensate separately from condensate formed in situ due to grid-scale saturation (Bacmeister et al., 2006). The latter source is represented via a two-parameter joint PDF. Sources of large-scale condensate due to both convective detrainment and in situ condensation are considered, with slower autoconversion rates for detrained condensate. Anvil condensate is gradually converted to have the same properties as condensate formed in situ.
MERRA-2	A prognostic scheme that tracks convectively-detrained "anvil" condensate separately from condensate formed in situ due to grid-scale saturation (Bacmeister et al., 2006). The latter source is represented via a two-parameter joint PDF, with new constraints on distributions of total water following Molod (2012). Sources of large-scale condensate due to both convective detrainment and in situ condensation are considered, with slower autoconversion rates for detrained condensate. Anvil condensate is gradually converted to have the same properties as condensate formed in situ. The function used to determine the initial partitioning of liquid and ice has been altered from that used in MERRA (see also Fig. 2.3).

NCEP-NCAR R1	Diagnosed from an empirical relationship with grid-scale RH that depends on latitude, surface type (land or water), and location in the Eastern or Western Hemisphere; the latter condition results in discontinuities in cloudiness around 0°E and 180°E (Kanamitsu et al., 2002). Convectively detrained anvil clouds are not explicitly considered.
NCEP-DOE R2	Diagnosed as a function of grid-scale RH, modified from that used by R1 to eliminate the dependence on location in the Eastern or Western Hemisphere (Kanamitsu et al., 2002). Convectively detrained anvil clouds are not explicitly considered.
CFSR / CFSv2	A simple cloud physics parameterization in which cloud fraction (Xu and Randall, 1996a) is diagnosed primarily according to prognostic cloud condensate (Zhao and Carr, 1997), with relative humidity as a secondary determining factor. Sources of stratiform cloud due to both convective detrainment and in situ condensation are considered.
NOAA-CIRES 20CR v2	A simple cloud physics parameterization in which cloud fraction (Xu and Randall, 1996a) is diagnosed primarily according to prognostic cloud condensate (Zhao and Carr, 1997), with relative humidity as a secondary determining factor. Sources of stratiform cloud due to both convective detrainment and in situ condensation are considered.

Moist convection is another critical subgrid-scale process that must be parameterized in atmospheric models (Arakawa, 2004). All of the reanalyses represent moist convection using versions of bulk mass-flux parameterizations (e.g., Arakawa and Schubert, 1974; Tiedtke, 1989), which have their conceptual basis in the "hot tower" hypothesis of Riehl and Malkus (1958). These parameterizations represent the statistical effects of convection in a given grid cell via one or more updraft and downdraft plumes, which are in turn coupled to the background environment via entrainment and detrainment, diabatic heating, and the vertical transport of tracers and momentum. Key differences in the convective parameterizations used by the reanalysis systems include the trigger function, the principal closure, whether and to what extent momentum and tracer transport are included, restrictions on the properties of the individual plumes (e.g., entrainment, detrainment, cloud base, and cloud top), and assumptions governing the production and partitioning of rainfall and cloud condensate. We briefly describe the first two aspects (trigger functions and closure assumptions) in the following two paragraphs, and then summarize the convection schemes used in each reanalysis in Table 2.6.

The trigger function determines under what conditions the convection scheme is activated. In ERA-40, convection was triggered when a surface parcel undergoing undilute ascent reached its LCL with buoyancy greater than a critical threshold. This procedure was modified starting with ERA-Interim to consider entrainment during ascent between the starting position and the LCL (Bechtold et al., 2006). Tests for shallow convection consider only the lowest model level and take into account surface sensible and latent enthalpy fluxes, while tests for deep convection allow for starting positions within 350 hPa of the surface. Trigger functions are similar for ERA-20C and ERA5, but with different assumptions regarding mixing between the test parcel and its

environment as it ascends to the LCL. Convection in JRA-25 was triggered when the cloud work function exceeded a critical threshold (Arakawa and Schubert, 1974; Aonashi et al., 1997). This differs from JRA-55, which triggers the convection scheme when the time rate of change in CAPE due to large-scale forcing exceeds a specified critical value (Xie and Zhang, 2000). The cloud base is fixed at ~900 hPa in both JRA-25 and JRA-55. MERRA and MERRA-2 use ensembles of plumes with variable entrainment rates to represent subgrid-scale convection (Moorthi and Suarez, 1992), triggered when sub-cloud RH exceeds 60%. Plumes are defined as extending from cloud base (defined as an average of the lowest two model levels in MERRA and as the ABL height in MERRA-2) to any model level between 100 hPa and the level above cloud base, permitting a unified representation of deep and shallow convection. Plumes are activated sequentially from deep to shallow, with each plume altering the background environment felt by subsequent plumes. MERRA-2 implements an additional stochastic Tokioka-type entrainment condition based on the results of Bacmeister and Stephens (2011), which limits the occurrence of plumes with very small entrainment rates (corresponding to the highest cloud top heights; Molod et al., 2015). In NCEP-NCAR R1 and NCEP-DOE R2, the test parcel for each grid column is defined as the level of maximum MSE within 400 hPa of the surface. Cloud base is defined as the LFC for this test parcel, with convection suppressed when the vertical displacement between the test parcel and its LFC is too large. CFSR and 20CR use the approach suggested by Hong and Pan (1998), which adapts the approach used in R1 and R2 to explicitly couple moist convection to boundary layer turbulence and subgrid-scale surface heterogeneity. Cloud base in CFSR and 20CR is defined as the LCL, rather than the LFC as in R1 and R2.

Closure assumptions govern how and to what extent subgrid-scale convection adjusts its grid-scale environment. Principal closures used by reanalyses include the 'quasi-equilibrium' hypothesis (e.g., Arakawa and Schubert, 1974), relaxed adjustment (e.g., Moorthi and Suarez, 1992), and CAPE-based closures (e.g., Gregory and Rowntree, 2000; Bechtold et al., 2014). Under quasi-equilibrium, the stabilizing effects of subgrid-scale convection (i.e., consumption of buoyancy) are assumed to be in quasi-equilibrium with the destabilizing effects of the large-scale circulation (i.e., production of buoyancy). Versions of this assumption are used by JRA-25, JRA-55, NCEP-NCAR R1, NCEP-DOE R2 CFSR, and 20CR. Under relaxed adjustment, which is used by MERRA and MERRA-2, the convection scheme is assumed to relax the environment toward a fraction of the large-scale forcing over a specified time scale (ranging from 30 minutes for shallow convection to 12 h for deep convection). The CAPE-based closures used by ECMWF reanalyses assumed that convection acts to reduce CAPE toward zero over a specified adjustment time scale, which is set to 1 h in ERA-40 and ERA-Interim and is proportional to the convective turnover time scale in ERA-20C and ERA5. ERA5 introduces several additional elements to this closure to better represent coupling between convection and conditions in the boundary layer, as described by Bechtold et al. (2014). See also Arakawa (2004) for discussion on the distinction between 'principal' and 'supplementary' closures. The latter are not described in detail here.

Table 2.6: Convective parameterizations used in the reanalysis systems.

ERA-40	Deep, shallow, and mid-level cumulus convection are parameterized using a bulk mass flux scheme based on that proposed by Tiedtke (1989). Each simulated convective cloud consists of a single pair of entraining/detraining plumes that represent updraught and downdraught processes.

ERA-Interim	Deep, shallow, and mid-level cumulus convection are parameterized using a bulk mass flux scheme based on that proposed by Tiedtke (1989), modified in several respects from those used in ERA-40 to improve the diurnal cycle of convection, increase convective precipitation efficiency, and make more explicit distinctions among shallow, mid-level and deep convective clouds (Dee et al., 2011).
ERA-20C	Deep, shallow, and mid-level cumulus convection are parameterized using a bulk mass flux scheme based on that proposed by Tiedtke (1989), similar to that used in ERA-Interim but with modified representations of entrainment and detrainment rates and a revised convective adjustment time scale.
ERA5	Deep, shallow, and mid-level cumulus convection are parameterized using a bulk mass flux scheme based on that proposed by Tiedtke (1989), with the closure modified from that in ERA-20C to better represent coupling between the boundary layer and free troposphere (Bechtold et al., 2014).
JRA-25 / JCDAS	An 'economical prognostic' mass-flux type Arakawa–Schubert cumulus scheme (Arakawa and Schubert, 1974; JMA, 2007).
JRA-55	An 'economical prognostic' mass-flux type Arakawa–Schubert cumulus scheme (Arakawa and Schubert, 1974; JMA, 2013), similar to that used by JRA-25 but with a new dynamic CAPE triggering mechanism (Xie and Zhang, 2000).
MERRA	A version of the relaxed Arakawa–Schubert cumulus scheme (Moorthi and Suarez, 1992). A spectrum of plumes with variable entrainment rates allows the scheme to represent both shallow and deep convection.
MERRA-2	A version of the relaxed Arakawa–Schubert cumulus scheme (Moorthi and Suarez, 1992). A spectrum of plumes with variable entrainment rates allows the scheme to represent both shallow and deep convection. A stochastic Tokioka-type trigger is implemented to limit the occurrence of plumes with very small entrainment rates (Molod et al., 2015).
NCEP-NCAR R1	Deep convective clouds are simulated using a simplified Arakawa–Schubert convection scheme (Arakawa and Schubert, 1974; Pan and Wu, 1995), without momentum transport. Shallow convective clouds are simulated following Tiedtke (1989).
NCEP-DOE R2	Deep convective clouds are simulated using a simplified Arakawa–Schubert convection scheme (Arakawa and Schubert, 1974; Pan and Wu, 1995), without momentum transport. Shallow convective clouds are simulated following Tiedtke (1989). Both deep and shallow convective parameterizations have undergone minor tuning relative to those used by R1.

CFSR / CFSv2	Deep convective clouds are simulated using a simplified Arakawa–Schubert convection scheme (Arakawa and Schubert, 1974; Moorthi et al., 2001). Shallow convective clouds are simulated following Tiedtke (1989). Momentum transport is included in the deep convective scheme, along with other updates relative to the parameterizations used by R1 and R2 (Moorthi et al., 2010; Saha et al., 2010).
NOAA-CIRES 20CR v2	Deep convective clouds are simulated using a simplified Arakawa–Schubert convection scheme (Arakawa and Schubert, 1974; Moorthi et al., 2001). Shallow convective clouds are simulated following Tiedtke (1989). Momentum transport is included in the deep convective scheme, along with other updates relative to the parameterizations used by R1 and R2 (Moorthi et al., 2010; Saha et al., 2010).

Gravity wave drag (GWD) parameterizations are used in reanalysis forecast models to represent the systematic effects of momentum deposition on the resolved flow by small-scale (i.e., unresolved) gravity waves. As a relative fraction of the momentum budget the importance of GWD forcing generally increases with altitude, becoming a dominant contribution in the mesosphere (Polavarapu et al., 2005), but effects can also be significant at lower altitudes, such as on the upper poleward flank of the tropospheric subtropical jet (Palmer et al., 1986; McFarlane, 1987). GWD parameterizations are typically implemented in atmospheric models via separate schemes for orographic and non-orographic gravity waves. All reanalysis systems considered here include some form of orographic GWD parameterization, but only ERA-20C, ERA5, MERRA, MERRA-2, and CFSv2 include non-orographic GWD parameterizations (Table 2.7).

Orographic waves generated by flow over topography have zero horizontal phase speed with respect to the ground. Momentum deposition occurs when vertically propagating waves break due to encountering critical levels (zero wind lines) or become unstable due to wave amplitude growth induced by decreasing atmospheric density. The resulting momentum tendency from the parameterization acts to drag the resolved flow toward the phase speed of the waves (i.e., toward zero). Non-orographic waves, which include those generated by moist convection or frontal instabilities, occur for a wide range of horizontal phase speeds. Correspondingly, their critical levels occur for a wide range of horizontal wind speeds, and forcing due to these waves can either accelerate or decelerate the resolved flow. Forcing by non-orographic gravity waves provides an appreciable component of the wave driving of the QBO, which requires both eastward and westward wave forcing (Lindzen and Holton, 1968). Non-orographic GWD schemes typically contain a number of adjustable parameters that are not well constrained by observations (Alexander et al., 2010), which allows some freedom to tune these schemes to improve aspects of the large-scale flow such as the QBO or mesopheric jets. An example is the total momentum flux in the imposed launch spectrum of the waves, which affects the QBO period. Following adjustments to the non-orographic GWD parameterization in GEOS-5, the MERRA-2 forecast model exhibits a spontaneous QBO signal (Coy et al., 2016). Similar results have been reported for recent versions of the ECMWF IFS (Orr et al., 2010; Hersbach et al., 2015).

Table 2.7: Gravity wave drag parameterizations used in the reanalysis systems.

ERA-40	Subgrid-scale orographic drag is parameterized using the scheme developed by Lott and Miller (1997). The representation of the orographic gravity wave source follows Miller et al. (1989) and Baines and Palmer (1990), and accounts for three-dimensional variability in the amplitude and orientation of wave stress. Non-orographic gravity wave drag is represented as Rayleigh friction above the stratopause.
ERA-Interim	Subgrid-scale orographic drag is parameterized using the scheme developed by Lott and Miller (1997). The representation of the orographic gravity wave source follows Miller et al. (1989) and Baines and Palmer (1990), and accounts for three-dimensional variability in the amplitude and orientation of wave stress. Non-orographic gravity wave drag is represented as Rayleigh friction above the stratopause.
ERA-20C	Subgrid-scale orographic drag is parameterized using the scheme developed by Lott and Miller (1997). The representation of the orographic gravity wave source follows Miller et al. (1989) and Baines and Palmer (1990). Non-orographic gravity wave drag is included using the parameterization proposed by Scinocca (2003); see also Orr et al. (2010).
ERA5	Subgrid-scale orographic drag is parameterized using the scheme developed by Lott and Miller (1997). The representation of the orographic gravity wave source follows Miller et al. (1989) and Baines and Palmer (1990). Non-orographic gravity wave drag is included using the parameterization proposed by Scinocca (2003); see also Orr et al. (2010).
JRA-25 / JCDAS	The orographic gravity wave drag parameterization consists of a long wave (wavelengths over 100 km) component and a short wave (wavelengths of ∼10 km) component (Iwasaki et al., 1989a,b). Long waves are assumed to propagate upward and break mainly in the stratosphere, where they exert drag (Palmer et al., 1986). Short waves are regarded as trapped and dissipating within the troposphere. Non-orographic gravity wave drag is not included.
JRA-55	The orographic gravity wave drag parameterization consists of a long wave (wavelengths over 100 km) component and a short wave (wavelengths of ∼10 km) component (Iwasaki et al., 1989a,b). Long waves are assumed to propagate upward and break mainly in the stratosphere, where they exert drag (Palmer et al., 1986). Short waves are regarded as trapped and dissipating within the troposphere. Non-orographic gravity wave drag is not included.
MERRA	MERRA includes parameterizations that compute drag due to the breaking of orographic (McFarlane, 1987) and non-orographic (after Garcia and Boville, 1994).

MERRA-2	MERRA-2 includes parameterizations that compute drag due to the breaking of orographic (McFarlane, 1987) and non-orographic (after Garcia and Boville, 1994). The scheme has been modified from that used in MERRA, with an increased latitudinal profile of the gravity wave drag background source at certain latitudes and increased intermittency (Molod et al., 2015).
NCEP-NCAR R1	An orographic gravity wave drag scheme based on Palmer et al. (1986), Pierrehumbert (1986), and Helfand et al. (1987) is included in the forecast model. Non-orographic gravity wave drag is not included.
NCEP-DOE R2	An orographic gravity wave drag scheme based on Palmer et al. (1986), Pierrehumbert (1986), and Helfand et al. (1987) is included in the forecast model. Non-orographic gravity wave drag is not included.
CFSR / CFSv2	The orographic gravity wave drag parameterization is based on the scheme proposed by Kim and Arakawa (1995). Sub-grid scale mountain blocking is represented using the scheme developed by Lott and Miller (1997). Although non-orographic gravity wave drag is not considered in CFSR, a simple representation of non-orographic gravity wave drag is included in CFSv2 via the parameterization proposed by Chun and Baik (1998).
NOAA-CIRES 20CR v2	The orographic gravity wave drag parameterization is based on the scheme proposed by Kim and Arakawa (1995). Sub-grid scale mountain blocking is represented using the scheme developed by Lott and Miller (1997). Non-orographic gravity wave drag is not considered.

Table 2.8 briefly describes the implementations of horizontal and vertical diffusion in the atmospheric forecast models used by the reanalysis systems. All of the systems that use spectral dynamical cores on Gaussian or reduced Gaussian grids (see above) use implicit linear diffusion in spectral space, although the implementations vary from second-order (R1, R2, and 20CR) to eighth-order (CFSR). MERRA and MERRA-2, which are built on finite volume dynamical cores, use slightly different implementations of explicit second-order diffusion. Representations of vertical diffusion in the free troposphere and above are based on first order K-type closures. MERRA, MERRA-2, NCEP-NCAR R1, NCEP-DOE R2, CFSR, and 20CR use versions of the parameterization suggested by Louis et al. (1982) with different background coefficients, while ERA-40 and ERA-Interim use the 'revised Louis' parameterization described by Beljaars (1994). ERA-20C and ERA5 use Monin–Obukhov similarity (Nieuwstadt, 1984), with the exception of some regions of the upper ABL and lower troposphere, where the revised Louis scheme is used to enhance turbulent mixing at positive Richardson numbers relative to that predicted by Monin–Obukhov similarity (Flannaghan and Fueglistaler, 2014). JRA-25 and JRA-55 use the 'level 2' closure outlined by Mellor and Yamada (1974). Example similarity functions based on these four approaches are shown for gradient Richardson numbers (Ri) between 0 and 0.5 in Figure 2.4. Perhaps the most notable difference is at large values of Ri, where the Louis et al. (1982) and revised Louis parameterizations have long tails. These long tails contrast with the behavior of the Monin–Obukhov and

Mellor and Yamada (1974) formulations, which have critical thresholds at Ri = 0.21 and Ri = 0.22, respectively, beyond which turbulent exchange no longer occurs. The inclusion of a critical threshold near Ri $\approx$ 0.25 is consistent with the observed behavior of Kelvin–Helmholtz instability, but may cause the model to underestimate subgrid-scale mixing when gravity waves (which tend to reduce Ri) are not adequately resolved. Note that Figure 2.4 does not include any information on the nominal mixing lengths or background diffusion coefficients, which also affect the relationship between f(Ri) and K (see, e.g., Appendix A of Flannaghan and Fueglistaler, 2014). Differences in specified mixing lengths (or 'background diffusion coefficients') often vary by height and are therefore more difficult to summarize in this way, but may exacerbate or ameliorate the effects of differences in the similarity functions. Consideration of turbulence in the surface layer and ABL introduces an even wider array of parameterizations for turbulent mixing, which are listed in Table 2.8 but not introduced in detail in this document. Differences in these parameterizations may influence surface exchanges of enthalpy and momentum. Table 2.9 introduces different treatments of surface roughness lengths over land and ocean, which also affect energy and momentum fluxes into the atmosphere.

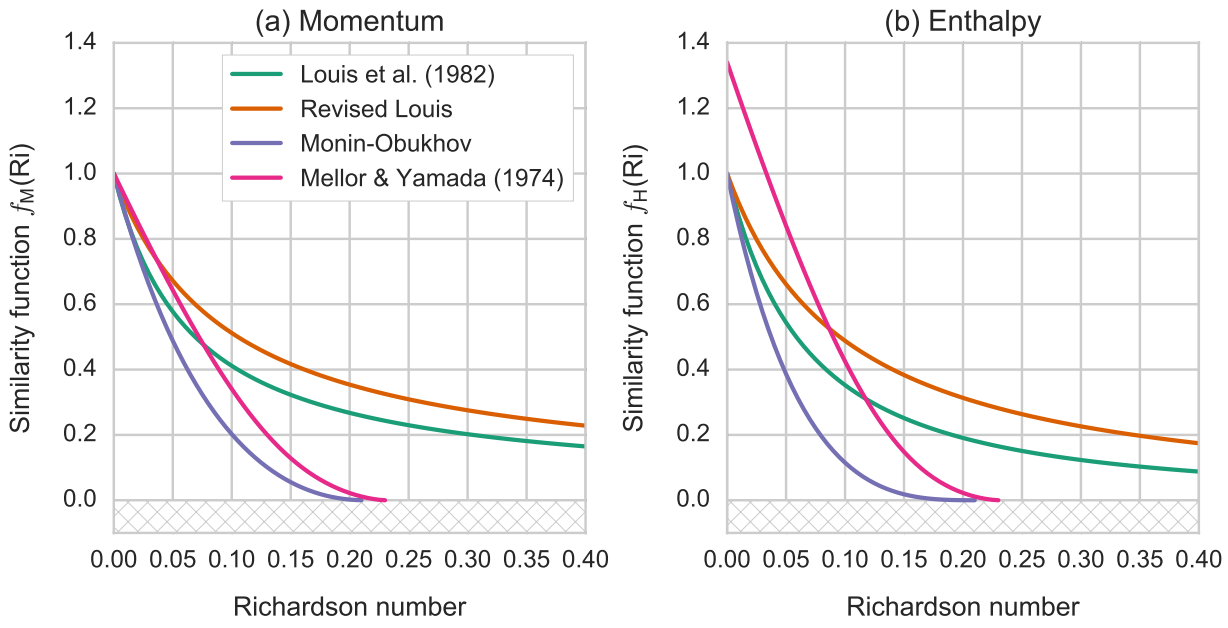

Figure 2.4: Similarity functions for parameterized turbulent transfer of (a) momentum and (b) enthalpy (heat and moisture) as a function of the gradient Richardson number (Ri) based on four turbulence schemes used in the free troposphere by reanalysis systems. See text for details.

Table 2.8: Representations of vertical and horizontal diffusion in the forecast models.

ERA-40	Horizontal diffusion: Implicit linear fourth-order diffusion in spectral space. Vertical diffusion: Vertical diffusion in the free atmosphere and in the ABL under stable conditions is based on the revised Louis scheme (Louis, 1979; Beljaars, 1994) for positive Richardson numbers and on Monin–Obukhov similarity for negative Richardson numbers. Vertical diffusion in the ABL under unstable conditions is based on the non-local scheme proposed by Troen and Mahrt (1986). Turbulent fluxes in the surface layer are calculated using bulk formulae based on Monin–Obukhov similarity.
ERA-Interim	Horizontal diffusion: Implicit linear fourth-order diffusion in spectral space. Vertical diffusion: Vertical diffusion in the free atmosphere and in the ABL under stable conditions is based on the revised Louis scheme (Louis, 1979; Beljaars, 1994) for positive Richardson numbers and on Monin–Obukhov similarity for negative Richardson numbers. Vertical diffusion in the ABL under unstable conditions is based on an eddy-diffusivity mass-flux (EDMF) scheme (Köhler et al., 2011). Turbulent fluxes in the surface layer are calculated using bulk formulae based on Monin–Obukhov similarity.

ERA-20C	Horizontal diffusion: Implicit linear fourth-order diffusion in spectral space. Vertical diffusion: Vertical diffusion in the free troposphere is based on Monin–Obukhov similarity, except in the lowermost troposphere where the revised Louis scheme (Louis, 1979; Beljaars, 1994) is used for positive Richardson numbers. Vertical diffusion in the ABL above the surface layer is also based on the revised Louis scheme for positive Richardson numbers and on Monin–Obukhov similarity for negative Richardson numbers. A simple empirical parameterization of unresolved vertical wind shear is included as a function of height, with a peak value near 900 hPa. Vertical diffusion in the mixed layer under unstable conditions is based on an eddy-diffusivity mass-flux (EDMF) scheme (Köhler et al., 2011). Turbulent fluxes in the surface layer are calculated using bulk formulae based on Monin–Obukhov similarity.
ERA5	Horizontal diffusion: Implicit linear fourth-order diffusion in spectral space. Vertical diffusion: Vertical diffusion in the free troposphere is based on Monin–Obukhov similarity, except in the lowermost troposphere where the revised Louis scheme (Louis, 1979; Beljaars, 1994) is used for positive Richardson numbers. Vertical diffusion in the ABL above the surface layer is also based on the revised Louis scheme for positive Richardson numbers and on Monin–Obukhov similarity for negative Richardson numbers. The empirical parameterization for unresolved shear used in ERA-20C has been removed. Vertical diffusion in the mixed layer under unstable conditions is based on an eddy-diffusivity mass-flux (EDMF) scheme (Köhler et al., 2011). Turbulent fluxes in the surface layer are calculated using bulk formulae based on Monin–Obukhov similarity.
JRA-25 / JCDAS	Horizontal diffusion: Implicit linear fourth-order diffusion in spectral space. Vertical diffusion: Vertical diffusion of momentum, heat, and moisture are represented using the “level 2” turbulence closure scheme developed by Mellor and Yamada (1974). Surface turbulent fluxes are calculated using bulk formulae based on Monin–Obukhov similarity.
JRA-55	Horizontal diffusion: Implicit linear fourth-order diffusion in spectral space. Vertical diffusion: Vertical diffusion of momentum, heat, and moisture are represented using the “level 2” turbulence closure scheme developed by Mellor and Yamada (1974). Surface turbulent fluxes are calculated using bulk formulae based on Monin–Obukhov similarity.

MERRA	Horizontal diffusion: Explicit second-order horizontal divergence damping is included in the dynamical core. Vertical diffusion: Vertical diffusion in the free atmosphere and in the boundary layer under stable conditions is based on a local gradient Richardson number closure (Louis et al., 1982), but a tuning parameter severely suppresses turbulent mixing at pressures less than ~900 hPa. Vertical diffusion in the boundary layer under unstable conditions is based on the non-local scheme proposed by Lock et al. (2000).
MERRA-2	Horizontal diffusion: An explicit second-order horizontal divergence damping is included with the same parameters as in MERRA. A second-order Smagorinsky divergence damping is also applied in MERRA-2 (but not in MERRA). Vertical diffusion: Vertical diffusion in the free atmosphere and in the boundary layer under stable conditions is based on a local gradient Richardson number closure (Louis et al., 1982). The tuning parameter that suppressed turbulent mixing at pressures less than ~900 hPa in MERRA has been removed, but diffusion coefficients are still usually very small in the free atmosphere. Vertical diffusion in the boundary layer under unstable conditions is based on the non-local scheme proposed by Lock et al. (2000). A Monin–Obukhov-type parameterization is introduced to represent turbulent fluxes across the surface layer (Helfand and Schubert, 1995).
NCEP-NCAR R1	Horizontal diffusion: Implicit linear second-order diffusion in spectral space. Horizontal diffusion along model σ layers causes spurious "spectral precipitation", particularly in mountainous areas at high latitudes. A special precipitation product has been produced to correct this issue. Vertical diffusion: Local K diffusion (Louis et al., 1982) is applied in both the ABL and the free atmosphere with a uniform background diffusion coefficient.
NCEP-DOE R2	Horizontal diffusion: Implicit linear second-order diffusion in spectral space. Issues with spectral precipitation caused by horizontal diffusion are greatly reduced relative to R1. Vertical diffusion: Local K diffusion (Louis et al., 1982) is applied in the free atmosphere with a uniform background diffusion coefficient. Non-local diffusion is applied in the ABL (Hong and Pan, 1996).
CFSR / CFSv2	Horizontal diffusion: Implicit linear eighth-order diffusion in spectral space. Vertical diffusion: Local K diffusion (Louis et al., 1982) is applied in the free atmosphere with a background diffusion coefficient that decreases exponentially with pressure. Non-local vertical diffusion is applied in the ABL (Hong and Pan, 1996).

NOAA-CIRES 20CR v2	Horizontal diffusion: Implicit linear second-order diffusion in spectral space. Vertical diffusion: Local K diffusion (Louis et al., 1982) is applied in the free atmosphere with a background diffusion coefficient that decreases exponentially with pressure. Non-local vertical diffusion is applied in the ABL (Hong and Pan, 1996).

Table 2.9: Sources and representations of surface roughness in the reanalysis systems.

ERA-40	Roughness lengths over land are prescribed from a climatology, adapted to account for urban effects and sub-grid orography. Ocean roughness depends on the Charnock parameter (Charnock, 1955), which is in turn modified by ocean wave heights calculated via an OI analysis (Section 2.3). The wave height analysis background state consists of output from a wave model (Komen et al., 1994; Janssen et al., 2001), described in detail in the IFS documentation for Cy23r4. Satellite altimeter observations of wave height are assimilated when available.
ERA-Interim	Roughness lengths over land depend on vegetation and land cover type (Mahfouf et al., 1995). Ocean roughness depends on the Charnock parameter (Charnock, 1955), which is in turn modified by ocean wave heights calculated via an OI analysis (Section 2.3). The wave height analysis background state consists of output from a wave model (Komen et al., 1994; Janssen et al., 2001), described in detail in the IFS documentation for Cy31r1. Satellite altimeter observations of wave height are assimilated when available.
ERA-20C	Roughness lengths over land depend on vegetation and land cover type (Mahfouf et al., 1995). Ocean roughness depends on the Charnock parameter (Charnock, 1955), which is in turn modified by ocean wave heights simulated using a coupled wave model (Komen et al., 1994; Janssen et al., 2001). The wave model is described in detail in the IFS documentation for Cy38r1.
ERA5	Roughness lengths over land depend on vegetation and land cover type (Mahfouf et al., 1995). Ocean roughness depends on the Charnock parameter (Charnock, 1955), which is in turn modified by ocean wave heights calculated via an OI analysis (Section 2.3). The wave height analysis background state consists of output from a wave model (Komen et al., 1994; Janssen et al., 2001), described in detail in the IFS documentation for Cy41r2. Satellite altimeter observations of wave height are assimilated when available.

JRA-25 / JCDAS	Land surface roughness lengths are based on vegetation types (Dorman and Sellers, 1989), and are modified by snow cover (Table 2.16). Ocean surface wind stress accounts for oceanic waves excited by surface winds, with roughness lengths and wind-induced stress calculated iteratively in the model. Roughness lengths over ice-free ocean are determined from Charnock's relation (Charnock, 1955; Beljaars, 1994). Roughness lengths over sea ice are fixed at 0.001 m.
JRA-55	Land surface roughness lengths are based on vegetation types (Dorman and Sellers, 1989), and are modified by snow cover (Table 2.16). Ocean surface wind stress accounts for oceanic waves excited by surface winds, with roughness lengths and wind-induced stress calculated iteratively in the model. Roughness lengths over ice-free ocean are determined from Charnock's relation (Charnock, 1955; Beljaars, 1994). Roughness lengths over sea ice are fixed at 0.001 m.
MERRA	Roughness lengths over land are prescribed based on GLCC vegetation and land cover (USGS, 2000). Ocean roughness is represented by a polynomial function of surface wind speed that blends the approaches proposed by Kondo (1975) and Large and Pond (1981).
MERRA-2	Roughness lengths over land are prescribed based on GLCC vegetation and land cover (USGS, 2000). Ocean roughness is represented by a polynomial function of surface wind speed that blends the approaches proposed by Kondo (1975) and Large and Pond (1981). The formulation is modified from that used in MERRA for wind speeds greater than $\sim 5\,\mathrm{m\,s^{-1}}$ (Molod et al., 2015).
NCEP-NCAR R1	Roughness lengths over land are prescribed based on vegetation and land surface type following Dorman and Sellers (1989). Ocean roughness is a function of surface wind stress via the Charnock relation (Charnock, 1955).
NCEP-DOE R2	Roughness lengths over land are prescribed based on vegetation and land surface type following Dorman and Sellers (1989). Ocean roughness is a function of surface wind stress via the Charnock relation (Charnock, 1955).
CFSR / CFSv2	Roughness lengths over land are prescribed based on vegetation and land surface type following Dorman and Sellers (1989). Ocean roughness is a function of surface wind stress via the Charnock relation (Charnock, 1955).
NOAA-CIRES 20CR v2	Roughness lengths over land are prescribed based on vegetation and land surface type following Dorman and Sellers (1989). Ocean roughness is a function of surface wind stress via the Charnock relation (Charnock, 1955).

2.2.3 Boundary and other specified conditions

This section describes the boundary and other specified conditions that can be regarded as "externally supplied forcings" for each reanalysis system. These conditions comprise the elements of the reanalysis that are not taken from the forecast model or data assimilation but are used to produce the outputs. Figure 2.5 shows three examples of how externally-specified boundary conditions may vary amongst reanalysis systems.

The factors that may be considered "external" vary somewhat among reanalyses because the forecast and assimilation components have provided a progressively larger fraction of the inputs (initial conditions) for the forecast model as reanalysis systems have developed. Ozone is a prime example. As discussed below, all of the reanalysis systems except for ERA-20C, NCEP-NCAR R1, NCEP-DOE R2, and NOAA-CIRES 20CR v2 (and JRA-55, ERA-40, and ERA5 for the period prior to 1978) assimilate satellite ozone measurements. Some reanalysis systems (notably the ECMWF reanalyses) use ozone climatologies rather than internally generated ozone fields for radiation calculations in the forecast model. MERRA-2 assimilates aerosol optical depths and uses internally generated aerosol fields for the radiation calculations, while other systems use climatologies or neglect the role of aerosols altogether. CFSR is a coupled atmosphere–ocean–sea ice system, in which the SST and sea ice lower boundary conditions for the atmospheric model are generated by an ocean model (although temperatures at the boundary are relaxed every six hours to SST analyses similar to those used as lower boundary conditions by other reanalysis systems). This section summarizes the treatment of SST, sea ice, ozone, aerosols, trace greenhouse gases (other than water vapour), and the solar cycle, with special notes where necessary. Dynamical variables, water vapour, and internally generated ozone (i.e., variables that are often directly constrained by the set of assimilated observations) are discussed and evaluated in Chapters 3 and 4 of this report.

2.2.3.1 Sea surface temperature and sea ice

Table 2.10 summarizes the treatment of SST and sea ice distributions in the reanalysis systems, including the names of SST and sea-ice datasets, special calibration or preprocessing details (e.g., bias corrections, interpolations), and details of how the datasets were produced.

Table 2.10: Treatment of sea surface temperature and sea ice.

ERA-40	Monthly data from the Met Office HadISST1 product was used before November 1981, replaced by weekly data from the NOAA–NCEP 2D-Var product from December 1981 through June 2001 and NOAA OISSTv2 from July 2001 through August 2002 (Reynolds et al., 2002). A special sea ice analysis and a method of specifying SST in grid boxes with partial ice-cover were used. Interpolation was used to produce daily values.
ERA-Interim	Monthly data from the Met Office HadISST1 product were used before November 1981, replaced by weekly data from the NOAA–NCEP 2D-Var product from December 1981 through June 2001 and NOAA OISSTv2 from July 2001 through December 2001. NCEP RTG SSTs were used from January 2002 through January 2009. The OSTIA analysis (Donlon et al., 2012) has been used from February 2009 through the present.

ERA-20C	Daily gridded SST and sea ice are from HadISST version 2.1.0.0 (Titchner and Rayner, 2014) at 0.25° horizontal resolution. Daily fields have been obtained via cubic interpolation from monthly analyses, with the temporal average of daily fields constrained to match the analysed monthly mean.
ERA5	Daily gridded SSTs are from HadISST version 2.1.0.0 (Titchner and Rayner, 2014) between January 1949 and August 2007, and from OSTIA for September 2007 onwards. Sea ice cover is from HadISST version 2.0.0.0 from January 1949 through December 1978, from reprocessed EUMETSAT OSI SAF fields between January 1979 and August 2007, and from operational OSI SAF estimates for September 2007 onwards. Data through August 2007 are at 0.25° horizontal resolution, while data from September 2007 to present are at 0.05° horizontal resolution. Daily fields are obtained via cubic interpolation from monthly analyses when necessary, with the temporal average of daily fields constrained to match the analysed monthly mean. Although SST fields are provided at hourly temporal resolution they only change once per day (at 2200 UTC).
JRA-25 / JCDAS	Daily COBE SSTs (Ishii et al., 2005) were used. COBE SSTs are based on the ICOADS and Kobe data collections, and do not include satellite data. Daily sea ice distributions prepared for COBE are based on reports by Walsh and Chapman (2001) for the Northern Hemisphere and Matsumoto et al. (2006) for the Southern Hemisphere.
JRA-55	Daily COBE SSTs (Ishii et al., 2005) were used. COBE SSTs are based on the ICOADS and Kobe data collections, and do not include satellite data. The COBE SST data include minor updates from those used for JRA-25/JCDAS. Daily sea ice distributions prepared for COBE are based on reports by Walsh and Chapman (2001) for the Northern Hemisphere and Matsumoto et al. (2006) for the Southern Hemisphere after October 1978. Southern Hemisphere sea ice coverage before October 1978 is based on a climatology.
MERRA	Starting with January 1982, weekly NOAA OISST data at 1° resolution (Reynolds and Smith, 1994) are linearly interpolated in time to the model time steps. Data for 1979–1981 are taken from an unpublished analysis conducted by the Met Office Hadley Centre.
MERRA-2	Monthly 1° gridded data (Taylor et al., 2000) prior to January 1982, daily 0.25° gridded data (Reynolds et al., 2007) through March 2006, and daily 0.05° gridded data from OSTIA (Donlon et al., 2012) starting from April 2006.

NCEP-NCAR R1	SSTs are taken from the Met Office GISST data set for 1981 and earlier, and from the NOAA OISST data set from 1982 to the present. Sea ice cover is from Navy/NOAA Joint Ice Center analyses before 1978, from SMMR observations for 1978 through 1987, and from SSM/I observations for 1988 through the present. Snow cover is from the NESDIS weekly snow cover analysis (Northern Hemisphere only) for September 1998 and earlier, and from the USAF global snow cover analysis from October 1998 through the present.
NCEP-DOE R2	SSTs and sea ice cover for January 1979 through 15 August 1999 are taken from data prepared for AMIP-II and provided by the PCMDI at Lawrence Livermore National Laboratory. SSTs and sea ice cover for 16 August 1999 through December 1999 are from monthly NOAA OISST and monthly NCEP operational sea ice analyses, interpolated to daily resolution. SSTs and sea ice cover for January 2000 to present are from daily NOAA OISST and NCEP operational sea ice analyses.
CFSR / CFSv2	The atmospheric model is coupled to the GFDL MOM version 4 ocean model and a two-layer sea ice model. AVHRR and AMSR satellite infrared observations of SST are assimilated in the SST analysis, along with in situ data from ships and buoys. The sea (and lake) ice concentration analysis products assimilate different observational data depending on the period, including microwave satellite observations when available. Temperatures at the atmosphere–ocean boundary are relaxed every six hours to separate SST analyses, including the 1° gridded HadISST1.1 from January 1979 through October 1981 and versions 1 and 2 of the 0.25° gridded OI analyses described by Reynolds et al. (2007) from November 1981. Further details of the coupling procedure and SST/sea ice analysis have been provided by Saha et al. (2010). Although some problems have been identified in sub-surface temperatures in CFSR (e.g., off the coast of Brazil; Y. Xue, personal communication), the assimilation of SST effectively constrains the surface temperatures in the analysis.
NOAA-CIRES 20CR v2	HadISST1.1 monthly mean SST and sea ice data are interpolated to daily resolution. Sea ice concentrations were accidentally misspecified in coastal regions. This error results in warmer lower tropospheric temperatures in both polar regions relative to ERA-40 and NCEP-NCAR R1 (Compo et al., 2011). The error has been corrected in 20CR v2c.

2.2.3.2 Ozone

Table 2.11 briefly summarizes the treatment of ozone in the reanalysis systems (detailed intercomparisons are deferred to Chapter 4 of the S-RIP Report). Some reanalysis systems assimilate satellite ozone measurements (from 1978/1979 onward) to produce an ozone analysis product, while

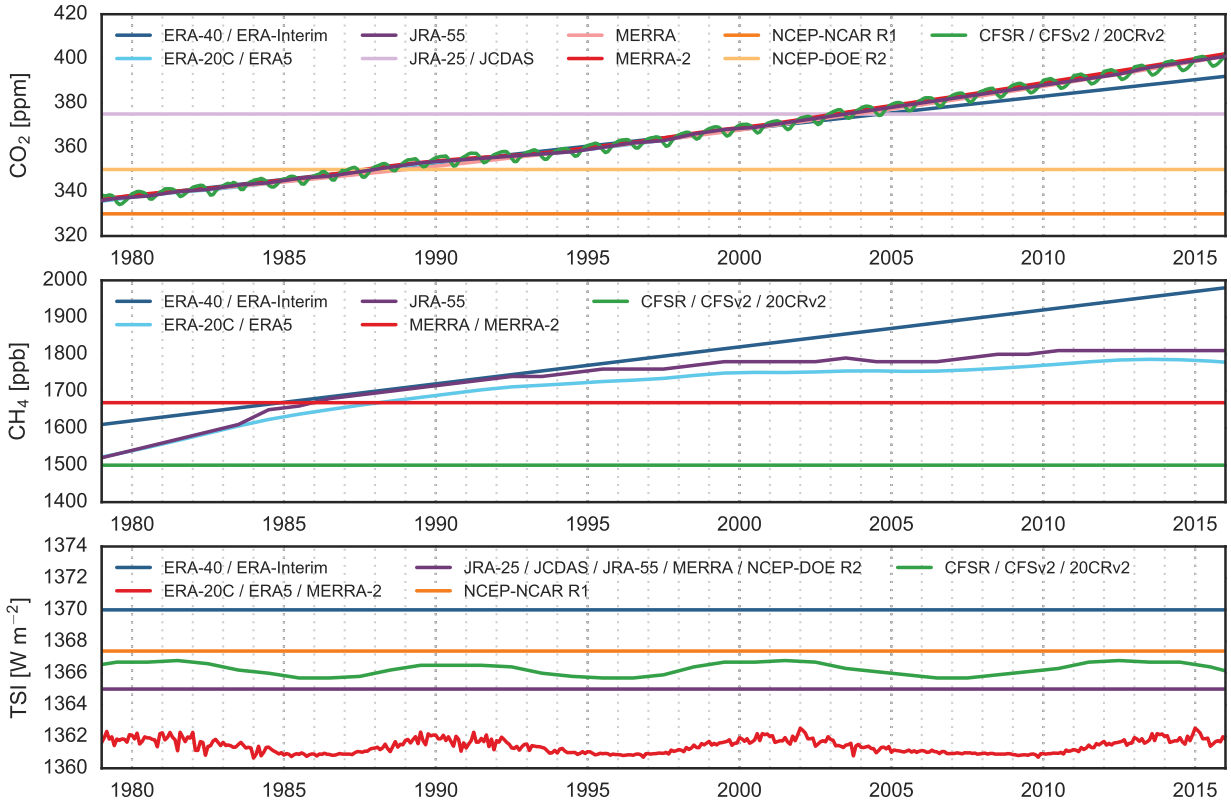

Figure 2.5: Time series of boundary and specified conditions for CO_2 (top), CH_4 (center), and TSI (bottom) used by the reanalysis systems. The CH_4 climatology used in MERRA and MERRA-2 varies in both latitude and height; here a "tropospheric mean" value is calculated as a mass- and area-weighted integral between 1000 and 288 hPa to facilitate comparison with the "well-mixed" values used by most other systems. ERA-20C and ERA5 also apply rescalings of annual mean values of CO_2 and CH_4 that vary in latitude and height; here the base values are shown. Time series of TSI neglect seasonal variations due to the ellipticity of the Earths orbit, as these variations are applied similarly (though not identically) across reanalysis systems. Additional information on CO_2 and CH_4 is provided in Table 2.13, and additional information on TSI is provided in Table 2.14.

some systems do not. Moreover, some systems that produce an ozone analysis use a climatological ozone distribution (rather than the ozone analysis) for radiation calculations in the forecast model. These distinctions are made explicit in Table 2.11. None of the reanalysis systems documented in this chapter assimilate data from ozonesondes.

Table 2.11: Treatment of ozone. See also Chapter 4 of the full S-RIP Report.

ERA-40	TOMS and SBUV ozone retrievals were assimilated from 1978 onward. Ozone in the model is described using a linearization of the ozone continuity equation, including photochemical sources and sinks (Cariolle and Déqué, 1986; Dethof and Hólm, 2004). The model does not account for heterogeneous chemistry, but does include an empirical ozone destruction term to account for chemical loss in polar stratospheric clouds. Model-generated ozone is not used in the radiation calculations, which instead assume the climatological ozone distribution described by Fortuin and Langematz (1995).
ERA-Interim	Ozone retrievals are assimilated from TOMS (1979–present), SBUV (1979–present), GOME (1996–2002), MIPAS (2003–2004), SCIAMACHY (2003–2008), Aura MLS (2008–present), and OMI (2008–present). The ozone scheme is an updated version of that used in ERA-40 (Cariolle and Teyssèdre, 2007; Dragani, 2011). Model-generated ozone is not used in the radiation calculations, which instead assume the climatological ozone distribution described by Fortuin and Langematz (1995).
ERA-20C	No ozone data are assimilated. The forecast model ozone parameterization is identical to that used in ERA-Interim. Model-generated ozone is not used in the radiation calculations, which instead use monthly three-dimensional ozone fields that evolve in time (Cionni et al., 2011).
ERA5	The ozone scheme is the same as that used in ERA-Interim (Cariolle and Teyssèdre, 2007; Dragani, 2011), but there are substantial differences in the assimilated data. Reprocessed ozone retrievals are assimilated from TOMS version 8 (1979–2003), SBUV version 8.6 (1979–present), CCI MIPAS (2005–2012), CCI SCIAMACHY (2003–2012), Aura MLS version 4.2 (2004–present), and OMI-DOAS from KNMI (2004–present). ERA5 also uses IR ozone-sensitive radiances not used in ERA-Interim, and the ozone analysis uses variational bias correction (Section 2.4.3.2). Analyzed ozone is not used in the radiation calculations, which instead use an in-house ozone climatology from CAMSiRA (Flemming et al., 2017).
JRA-25 / JCDAS	Daily ozone distributions were prepared in advance using the MRI-CCM1 offline CTM with output "nudged" to satellite retrievals of total ozone. These distributions were provided to the forecast model for use in radiation calculations.

JRA-55	For 1979 and later, daily ozone distributions have been prepared in advance using the MRI-CCM1 offline CTM with output "nudged" to satellite retrievals of total ozone. These distributions are provided to the forecast model for use in radiation calculations. This approach is similar to that used by JRA-25/JCDAS, but uses an updated chemical transfer model with 68 vertical levels rather than 45. For 1958–1978, a monthly mean climatology generated from the 1980–1984 ozone analyses was used.
MERRA	Version 8 SBUV ozone retrievals have been assimilated from October 1978 onward. The ozone parameterization is based on an empirical relationship between ozone and prognostic odd-oxygen that varies with height and the diurnal cycle (Rienecker et al., 2008). The parameterization uses zonally-symmetric monthly production and loss rates derived from a 2-D model as described by Stajner et al. (2008), but without representation of heterogeneous chemistry in polar regions. The forecast model uses analyzed ozone data in radiation calculations.
MERRA-2	Version 8.6 SBUV retrievals have been assimilated in reanalyses between 1980 and 2004. Starting from October 2004, these data have been replaced by retrieved Aura MLS profiles (version 2.2 through 31 May 2015; version 4.2 from 1 June 2015) and OMI observations of total ozone (McCarty et al., 2016). Assimilation of MLS retrievals at 261 hPa was discontinued starting on 1 May 2016 (Wargan et al., 2017). The ozone parameterization is based on an empirical relationship between ozone and prognostic odd-oxygen that varies with height and the diurnal cycle (Rienecker et al., 2008). The parameterization uses zonally-symmetric monthly production and loss rates derived from a 2-D model as described by Stajner et al. (2008), but without representation of heterogeneous chemistry in polar regions. The forecast model uses analyzed ozone data in radiation calculations.
NCEP-NCAR R1	Seasonal ozone climatologies reported by London (1962) and Hering and Borden (1965) are used in radiation calculations. No ozone analysis is produced.
NCEP-DOE R2	The zonal mean ozone climatology published by Rosenfield et al. (1987) is used in radiation calculations, but the latitudinal orientation was reversed north-to-south. Although this error may cause some problems in the stratosphere, the overall impact is minor (Kanamitsu et al., 2002). No ozone analysis is produced.

CFSR / CFSv2	Version 8 SBUV profiles and total ozone retrievals were assimilated without bias adjustment. Prognostic ozone is parameterized using concentration-dependent climatological production and destruction terms generated by a 2-dimensional chemistry model (McCormack et al., 2006). The forecast model uses analyzed ozone data for radiation calculations. Late 20th century levels of CFCs are included implicitly in the gas phase chemistry and ozone climatology used in the prognostic ozone parameterization.
NOAA-CIRES 20CR v2	No ozone data are assimilated. Prognostic ozone is parameterized using concentration-dependent climatological production and destruction terms generated by a 2-dimensional chemistry model (McCormack et al., 2006), and is used by the forecast model for radiation calculations. Late 20th century levels of CFCs are included implicitly in the gas phase chemistry and ozone climatology used in the prognostic ozone parameterization.

2.2.3.3 Aerosols

Table 2.12 summarizes the treatment of stratospheric and tropospheric aerosols in the reanalysis systems. Some reanalysis systems consider tropospheric aerosols over continents and over oceans separately in the radiation scheme. Some reanalysis systems (but not all) account for changes in stratospheric aerosols due to volcanic eruptions. One reanalysis (MERRA-2) assimilates aerosol optical depths and uses analyzed aerosols in radiation calculations.

Table 2.12: Treatment of aerosols.

ERA-40	Aerosols have been included in the radiation calculations using prescribed climatological aerosol distributions (Tanré et al., 1984). These distributions include annual mean geographical distributions for maritime, continental, urban and desert aerosol types, in addition to uniformly distributed tropospheric and stratospheric 'background' aerosol loading. No trends or temporal variations (such as variations due to volcanic eruptions) were included.
ERA-Interim	Aerosols are included in the radiation calculations using prescribed climatological aerosol distributions (Tegen et al., 1997). These distributions include annual mean geographical distributions for maritime, continental, urban and desert aerosol types, in addition to uniformly distributed tropospheric and stratospheric 'background' aerosol loading. The climatological annual cycles of tropospheric aerosols have been revised relative to those used by ERA-40, as have the optical thickness values for tropospheric and stratospheric background aerosols. There is no evolution of volcanic aerosols.
ERA-20C	The evolution of tropospheric aerosols is based on data prepared for CMIP5 (Lamarque et al., 2010; van Vuuren et al., 2011). Volcanic sulphates (Sato et al., 1993) and ash (Tanré et al., 1984) are also included in the stratosphere. A detailed description of the aerosol fields used in ERA-20C and ERA-20CM has been provided by Hersbach et al. (2015).

ERA5	The evolution of tropospheric aerosols is based on data prepared for CMIP5 (Lamarque et al., 2010; van Vuuren et al., 2011). Volcanic sulphates (Sato et al., 1993) and ash (Tanré et al., 1984) are also included in the stratosphere.
JRA-25 / JCDAS	Aerosols are represented using two aerosol profiles, one over land and one over sea (WMO, 1986). Neither interannual nor seasonal variations are considered.
JRA-55	Aerosols are represented using two aerosol profiles, one over land and one over sea (WMO, 1986), with optical depths adjusted to a 2-dimensional monthly climatology (JMA, 2013). Interannual variations, such as those due to volcanic eruptions, are not considered.
MERRA	Aerosols are represented using a climatological aerosol distribution generated using the GOCART model (Colarco et al., 2010).
MERRA-2	Aerosol optical depths from AVHRR, MODIS, MISR, and AERONET are assimilated into the GEOS-5 Goddard Aerosol Assimilation System (Buchard et al., 2015, 2017; Randles et al., 2017). The forecast model uses analyzed aerosols in radiation calculations for the entire production period. A detailed introduction to the aerosol analysis in MERRA-2 has been provided by Randles et al. (2017).
NCEP-NCAR R1	No aerosols.
NCEP-DOE R2	No aerosols.
CFSR / CFSv2	Aerosols are represented using a seasonally varying climatological global distribution of aerosol vertical profiles on a 5° grid (Koepke et al., 1997). Monthly zonal mean volcanic aerosols in four latitude bands (90–45°S, 45°S–equator, equator–45°N, 45–90°N) are specified based on data reported by Sato et al. (1993).
NOAA-CIRES 20CR v2	Aerosols are represented using a seasonally varying climatological global distribution of aerosol vertical profiles on a 5° grid (Koepke et al., 1997). Monthly zonal mean volcanic aerosols in four latitude bands (90–45°S, 45°S–equator, equator–45°N, 45–90°N) are specified based on data reported by Sato et al. (1993).

2.2.3.4 Carbon dioxide and other radiatively active gases

Table 2.13 summarizes the treatment of carbon dioxide and other radiatively active gases (except for water vapour) in the reanalysis systems (see also Figure 2.5). Notes on the treatment of water vapour are provided in Section 2.4.4.

Table 2.13: Treatment of carbon dioxide and other radiatively active gases.

ERA-40	CO_2, CH_4, N_2O, CFC-11, and CFC-12 are assumed to have globally uniform concentrations throughout the atmosphere. The concentrations of these gases were set to the observed 1990 values plus a linear trend as specified by IPCC (1996).

ERA-Interim	CO_2, CH_4, N_2O, CFC-11, and CFC-12 are assumed to have globally uniform concentrations throughout the atmosphere. The concentrations of these gases were set to the observed 1990 values plus a linear trend as specified by IPCC (1996).
ERA-20C	CO_2, CH_4, N_2O, CFC-11, and CFC-12 are specified according to CMIP5-recommended values (Meinshausen et al., 2011). The IPCC RCP3PD scenario is followed for 2006–2010. Greenhouse gases are not assumed to be globally uniform; rather, they are rescaled to match specified seasonal cycles and zonal mean vertical distributions (Hersbach et al., 2015).
ERA5	CO_2, CH_4, N_2O, CFC-11, and CFC-12 are specified according to CMIP5-recommended values (Meinshausen et al., 2011). The IPCC RCP3PD scenario is followed for 2006–present. Greenhouse gases are not assumed to be globally uniform; rather, they are rescaled to match specified seasonal cycles and zonal mean vertical distributions (Hersbach et al., 2015)
JRA-25 / JCDAS	A constant, globally uniform CO_2 concentration of 375 ppmv was assumed. CH_4, N_2O, CFCs, and HCFCs were not considered.
JRA-55	Daily values of CO_2, CH_4, N_2O, CFC-11, CFC-12, and HCFC-22 are specified by interpolating from annual mean values. For CO_2, CH_4, and N_2O these annual mean values are valid on 1 July; for CFC-11, CFC-12, and HCFC-22 they are valid on 31 December. All species are assumed to be globally uniform. Data sources vary in time (Kobayashi et al., 2015, their Table 7).
MERRA	CO_2 concentrations are assumed to be globally uniform and are specified according to historical observed values. CH_4, N_2O, CFCs, and HCFCs are specified according to steady state monthly climatologies from the Goddard two-dimensional chemistry transport model (Rienecker et al., 2008). These monthly climatologies vary in both latitude and pressure, but do not contain interannual variability.
MERRA-2	Annual global mean CO_2 concentrations follow the CMIP5 historical and RCP4.5 scenarios and are assumed to be uniform throughout the atmosphere. CH_4, N_2O, CFCs, and HCFCs are specified according to steady state monthly climatologies from the Goddard two-dimensional chemistry transport model (Rienecker et al., 2008). These monthly climatologies vary in both latitude and pressure, but do not contain interannual variability
NCEP-NCAR R1	A constant, globally uniform CO_2 concentration of 330 ppmv is assumed. CH_4, N_2O, CFCs, and HCFCs were not considered.
NCEP-DOE R2	A constant, globally uniform CO_2 concentration of 350 ppmv is assumed. CH_4, N_2O, CFCs, and HCFCs were not considered.

CFSR / CFSv2	Monthly mean 15°×15° distributions of CO_2 concentrations derived from historical WMO Global Atmosphere Watch observations are used. Constant values of CH_4, N_2O, O_2, and four types of halocarbons are also included in the radiation calculations.
NOAA-CIRES 20CR v2	Monthly mean 15°×15° distributions of CO_2 concentrations derived from historical WMO Global Atmosphere Watch observations are used for 1956 and later. Estimates of semi-annual average global mean CO_2 concentrations based on ice core data are used for the period before 1956. Constant values of CH_4, N_2O, O_2, and four types of halocarbons are also included in the radiation calculations.

2.2.3.5 Solar cycle

The solar cycle (i.e., changes in TSI with a period of ~11 years) is an important driver of atmospheric variability. This variability is incorporated in reanalysis systems in a variety of ways, including specified solar radiation at the TOA (boundary condition) and/or observations of temperature or ozone (data assimilation). Table 2.14 briefly summarizes the extent to which interannual variations in TSI are represented in each reanalysis system (see also Figure 2.5).

Table 2.14: Influence of variations in TSI on the reanalysis systems.

ERA-40	The ~11-year solar cycle is not included in the TSI boundary condition, with the base irradiance assumed to be constant at 1370 W m^{-2}; however, variations in this value due to changes in the distance between the Earth and the Sun have been incorporated as prescribed by (Paltridge and Platt, 1976). A programming error artificially increased the effective TSI by about 2 W m^{-2} relative to the specified value. Dee et al. (2011) reported that the impact of this error is mainly expressed as a warming of approximately 1 K in the upper stratosphere; systematic errors in other regions are negligible. The effects of the solar cycle are included in the assimilated upper-air temperatures, but are not included in the ozone passed to the forecast model (see Table 2.11).
ERA-Interim	The ~11-year solar cycle is not included in the TSI boundary condition, with the base irradiance assumed to be constant at 1370 W m^{-2}; however, variations in this value due to changes in the distance between the Earth and the Sun have been incorporated as prescribed by (Paltridge and Platt, 1976). A programming error artificially increased the effective TSI by about 2 W m^{-2} relative to the specified value. Dee et al. (2011) reported that the impact of this error is mainly expressed as a warming of approximately 1 K in the upper stratosphere; systematic errors in other regions are negligible. The effects of the solar cycle are included in the assimilated upper-air temperatures, but are not included in the ozone passed to the forecast model (see Table 2.11).

ERA-20C	Uses TSI variations provided for CMIP5 historical simulations by the SPARC SOLARIS-HEPPA working group with the TIM scaling applied, which take values ranging from 1360.2 to 1362.7 $W\,m^{-2}$ between 1950 and 2008. These variations account for solar cycle changes through 2008 and repeat the final cycle (April 1996–June 2008) thereafter. Seasonal variations due to the ellipticity of the Earth's orbit are also included.
ERA5	Uses TSI variations provided for CMIP5 historical simulations by the SPARC SOLARIS-HEPPA working group with the TIM scaling applied, which take values ranging from 1360.3 to 1362.7 $W\,m^{-2}$ between 1950 and 2008. These variations account for solar cycle changes through 2008 and repeat the final cycle (April 1996–June 2008) thereafter. Seasonal variations due to the ellipticity of the Earth's orbit are also included.
JRA-25 / JCDAS	A constant base TSI of 1365 $W\,m^{-2}$ was assumed, including seasonal effects due to the ellipticity of the Earth's orbit (Spencer, 1971). Interannual variations in incoming solar radiation were not included in the TSI boundary condition, but were included in assimilated temperature and ozone observations.
JRA-55	A constant base TSI of 1365 $W\,m^{-2}$ was assumed, including seasonal effects due to the ellipticity of the Earth's orbit (Spencer, 1971). Interannual variations in incoming solar radiation are not included in the TSI boundary condition, but are included in assimilated temperature observations (for the whole period) and ozone observations (for 1979 and later).
MERRA	MERRA uses a constant base TSI of 1365 $W\,m^{-2}$. Seasonal variations due to the ellipticity of the Earth's orbit are also included.
MERRA-2	MERRA-2 uses TIM-corrected TSI variations provided for CMIP5 historical simulations by the SPARC SOLARIS-HEPPA working group, which take values ranging from 1360.6 to 1362.5 $W\,m^{-2}$ between 1980 and 2008. These variations account for solar cycle changes through 2008 and repeat the final cycle (April 1996–June 2008) thereafter. Seasonal variations due to the ellipticity of the Earth's orbit are also included.
NCEP-NCAR R1	R1 uses a constant TSI of 1367.4 $W\,m^{-2}$. The ~11-year solar cycle is not included in the TSI boundary condition, but variations due to changes in orbital geometry are accounted for. The effects of the solar cycle are included in the assimilated upper-air temperatures, but are not included in the ozone passed to the forecast model (see Table 2.11).

NCEP-DOE R2	R2 uses a constant TSI of 1365 W m^{-2}. The 11-year solar cycle is not included in the TSI boundary condition, but variations due to changes in orbital geometry are accounted for. The effects of the solar cycle are included in the assimilated upper-air temperatures, but are not included in the ozone passed to the forecast model (see Table 2.11).
CFSR / CFSv2	Annual average variations in TSI were specified according to data prepared by H. van den Dool (personal communication, 2006), which take values ranging from 1365.7 to 1367.0 W m^{-2}. The solar cycle after 2006 is repeated forwards (e.g., insolation for 2007 is the same as that for 1996, that for 2008 is the same as that for 1997, and so on). The effects of the solar cycle are included in assimilated temperature and ozone observations; however, the prognostic ozone parameterization does not otherwise account for variations in incoming solar radiation.
NOAA-CIRES 20CR v2	Annual average variations in TSI were specified according to data prepared by H. van den Dool (personal communication, 2006), which take values ranging from 1365.7 to 1367.0 W m^{-2}. The solar cycle before 1944 is repeated backwards (e.g., insolation for 1943 is the same as that for 1954, that for 1942 is the same as that for 1953, and so on) and the solar cycle after 2006 is repeated forwards (as for CFSR). No upper-air observations were assimilated or included, and the prognostic ozone parameterization does not account for variations in incoming solar radiation.

2.2.4 Surface air and land surface treatments

Treatments of surface air and land surface properties present a number of challenges for reanalyses. For example, sharp gradients and other types of spatial heterogeneity in land cover are difficult to represent in global models, but have important influences on the magnitudes and variability of water and energy fluxes between the land surface and the atmosphere. More specific to reanalyses, the spatial domain over which near-surface observations may be considered representative is reduced in coastal regions and regions of complex topography. Land surface properties, such as soil moisture and soil temperature, also evolve relatively slowly. As a result, these variables are among the main targets of model spin-up. Discontinuities in the land surface state at stream transitions (Section 2.5) can propagate into the atmosphere.

Reanalyses use two main approaches for producing surface air analysis variables over land. The first approach, which is taken by ERA-40, ERA-Interim, ERA5, JRA-25, and JRA-55, is to assimilate screen-level station observations (i.e., temperatures and dewpoint temperatures at 2-m height) in separate two-dimensional OI analyses (Section 2.3) of surface air variables (e.g., Simmons et al., 2004). The main benefits include stronger constraints on surface meteorological conditions and their influences on the LSM (see below); however, this approach can also generate inconsistencies between the upper air and surface fields in the analysis. None of the reanalysis systems use the results of OI surface air analyses to initialize subsequent forecasts, although these analyses can still indirectly affect subsequent forecasts via influences on the land surface state. The second approach, which is taken by all other reanalyses described in this document, omits screen-level

station observations from the analysis. Surface air analysis variables over land are still affected by surface pressure and (in the case of full-input reanalyses) upper air measurements assimilated during the standard analysis cycle. This approach establishes weaker observational constraints on the evolution of surface air and land surface conditions in regions where the observational network is dense, but has the benefit of producing a more internally-consistent atmospheric state. Reanalyses using this second approach are mutually independent with respect to external analyses of surface air temperatures over land (e.g., CRUTEM; Osborn and Jones, 2014); reanalyses using the first approach are not.

Land surface state variables that are simulated by atmospheric reanalyses include soil moisture and soil temperature. Analyses of these variables are not directly affected by data assimilation, but are instead produced by a LSM forced entirely or primarily by the reanalysis atmospheric state. In addition to the different treatments of surface air variables discussed above, a key difference among reanalyses in this respect is the source of the precipitation forcing, which may be taken from the atmospheric model, from observations, or from a combination of the two. The complexity and implementation of the land surface models used by reanalyses also varies widely. Several of the reanalyses implement some form of sub-grid 'tiling' to allow for different land cover types to coexist within a single grid cell. Spatial distributions of vegetation and soil characteristics are prescribed. These characteristics are typically assumed to be constant in time, although some of the prescribed climatologies include limited representations of seasonality.

Table 2.15: Information about land surface models and surface air analyses (if applicable).

ERA-40	Surface air and land surface analyses are performed outside of the main atmospheric reanalysis. Six-hourly OI analyses of surface air temperature and dewpoint temperature at 2-m height are produced using station observations over land and the background state from the most recent atmospheric analysis. Empirical relationships between surface air fields and soil properties are then used to update soil temperature and soil moisture in a four-level LSM (van den Hurk et al., 2000). Each grid cell is divided into subgrid tiles, where the set of tiles in a single grid cell must be either all land or all water. Surface fluxes are calculated separately for each tile assuming a single atmospheric column above and a single soil profile below. Land surface fluxes depend on vegetation coverage and characteristics, prescribed based on GLCC and invariant in time.

ERA-Interim	Surface air and land surface analyses are performed outside of the main atmospheric reanalysis. Six-hourly OI analyses of surface air temperature and dewpoint temperature at 2-m height are produced using station observations over land and the background state from the most recent atmospheric analysis. Empirical relationships between surface air fields and soil properties are then used to update soil temperature and soil moisture in a four-level LSM (van den Hurk et al., 2000). Each grid cell is divided into subgrid tiles, where the set of tiles in a single grid cell must be either all land or all water. Surface fluxes are calculated separately for each tile assuming a single atmospheric column above and a single soil profile below. Land surface fluxes depend on vegetation coverage and characteristics, prescribed based on GLCC and invariant in time. The additional global land surface reanalysis ERA-Interim/Land was conducted for 1979–2010 using a newer version of the land surface model (Balsamo et al., 2015) with atmospheric forcing from ERA-Interim and precipitation from GPCP.
ERA-20C	Surface pressure and surface winds (over ocean) are the only variables directly constrained by the data assimilation; no land surface analysis is performed. The land surface scheme is based on a new version of the LSM (Balsamo et al., 2015) relative to that used in ERA-Interim. Each model grid cell is divided into sub-grid tiles representing different surface types, with the set of tiles in a single grid cell restricted to be either all land or all water. Surface fluxes are calculated separately for each subgrid tile, assuming a single atmospheric column above and a single soil profile below. Surface fluxes over land tiles depend on vegetation type and characteristics. Prescribed values of leaf area index based on MODIS observations (Boussetta et al., 2013) introduce some seasonality. Other vegetation characteristics are based on GLCC and assumed constant in time.

ERA5	Surface air and land surface analyses are performed outside of the main atmospheric reanalysis. Hourly two-dimensional OI analyses of surface air temperature and dewpoint temperature at 2-m height are produced using station observations over land and the background state from the most recent atmospheric analysis. Soil temperature, soil moisture, and several snow variables (Table 2.16) are also analyzed as described by de Rosnay et al. (2014). The surface air and land surface analyses are weakly coupled through the use of a common coupled land–atmosphere forecast background state. Both conventional and satellite observations are assimilated over land, including scatterometer retrievals of soil moisture. The LSM is similar to that used in ERA-20C (Balsamo et al., 2015), but with a new mixed-layer formulation for representing subgrid-scale water tiles. Notably, the set of tiles in a single grid cell is no longer restricted to only land or only water, enabling a more realistic representation of lakes and coastlines. Surface fluxes are calculated separately for each subgrid tile, assuming a single atmospheric column, a single soil profile for land tiles, and a dedicated mixed-layer model for water tiles. Surface fluxes over land tiles depend on vegetation type and characteristics. Prescribed values of leaf area index based on MODIS observations (Boussetta et al., 2013) introduce some seasonality. Other vegetation characteristics are based on GLCC and assumed constant in time. A separate land surface analysis ERA5L is planned and now in production, with atmospheric forcing from ERA5.
JRA-25 / JCDAS	Surface air temperature, winds, and relative humidity are based on univariate OI analyses that assimilate meteorological station observations. Observation departures are computed relative to the background state at the analysis time rather than at the observation time. Soil temperature and soil moisture on three levels are updated four times per day using a modified version of the SiB model (Sellers et al., 1986; Sato et al., 1989) forced by atmospheric reanalysis fields applied every six hours. Vegetation properties are specified following Dorman and Sellers (1989) and are assumed to be constant in time, although some properties (e.g., LAI and percentage of vegetation cover) include seasonal variations.

JRA-55	Surface air temperature, winds, and relative humidity are based on univariate OI analyses that assimilate meteorological station observations. These analyses differ from those in JRA-25 in two ways. First, comparisons between observations and the first-guess background state are evaluated at observation times rather than analysis times. Second, screen-level observations over islands are not used as they may not be appropriately representative of conditions at the scale of the model grid cell. Soil temperature and soil moisture on three levels are updated four times per day using a modified version of the SiB model (Sellers et al., 1986; Sato et al., 1989) forced by atmospheric reanalysis fields applied every three hours. Vegetation properties are specified following Dorman and Sellers (1989) and are assumed to be constant in time, although some properties (e.g., LAI and percentage of vegetation cover) include seasonal variations.
MERRA	MERRA did not conduct separate surface air or land surface analyses. Screen-level temperature and humidity measurements over land are not assimilated, although surface air variables in both ANA and ASM products are affected by surface pressure and upper air measurements assimilated during the analysis cycle. Estimates of land surface properties represent the time-integrated effects of coupling between the Catchment LSM (Koster et al., 2000) and the surface conditions and fluxes generated by the atmospheric model during the IAU "corrector" segment (see Section 2.3). The LSM divides each grid cell into irregularly-shaped hydrological "catchments" to better account for the effects of sub-grid topographic variability on runoff and soil moisture transport. Vegetation types are prescribed based on GLCC and assumed to be constant in time, although some vegetation properties (e.g., LAI and vegetation greenness) are prescribed using seasonally-varying climatologies. A separate land surface analysis (MERRA-Land) has been conducted by replacing the model-generated precipitation with pentad-resolution GPCP data and an updated version of the Catchment LSM (Reichle et al., 2011).

MERRA-2	Although MERRA-2 does not conduct a separate land surface analysis, land precipitation inputs to the LSM are based mainly on observations rather than model-generated values between 60°S and 60°N (Reichle et al., 2017b). The reanalysis does not assimilate screen-level temperature or humidity measurements over land. Surface meteorological variables over land thus primarily reflect the net effects of assimilated surface pressures, model-generated surface fluxes (which are directly affected by precipitation corrections), and the upper-air assimilated state (which is not). MERRA-2 uses the Catchment LSM (Koster et al., 2000; Reichle et al., 2011), with several adjustments relative to MERRA and MERRA-Land (Reichle et al., 2017a). The LSM divides each grid cell into irregularly-shaped hydrological "catchments" to better account for the effects of sub-grid topographic variability on runoff and soil moisture transport. Vegetation types are prescribed and invariant in time, although some vegetation properties (e.g., LAI and vegetation greenness) are prescribed using seasonally-varying climatologies.
NCEP-NCAR R1	The reanalysis does not assimilate screen-level temperature or humidity measurements over land, although surface air variables are affected by surface pressure and upper air measurements assimilated during the standard analysis cycle. The land surface analysis includes soil moisture and soil temperature on two layers. Rather than an assimilation, this analysis is constructed by driving the 2-layer OSU LSM (Mahrt and Pan, 1984; Pan and Mahrt, 1987) using analyses of snow cover (Table 2.16) and atmospheric reanalysis fields as forcings. Soil moisture and temperature are relaxed toward a specified climatology.
NCEP-DOE R2	The reanalysis does not assimilate screen-level temperature or humidity measurements over land, although surface air variables are affected by surface pressure and upper air measurements assimilated during the standard analysis cycle. The land surface analysis includes soil moisture and soil temperature on two layers. Rather than an assimilation, this analysis is constructed by driving the 2-layer OSU LSM (Mahrt and Pan, 1984; Pan and Mahrt, 1987) using analyses of snow cover (Table 2.16) and atmospheric reanalysis fields as forcings. Precipitation inputs to the LSM are corrected for consistency with pentad-mean precipitation data from CMAP. The relaxation of soil variables to climatological values used in R1 was not used in R2.

CFSR / CFSv2	The reanalysis does not assimilate screen-level temperature or humidity measurements over land, although surface air variables are affected by surface pressure and upper air measurements assimilated during the standard analysis cycle. The land surface analysis includes soil moisture and soil temperature, and is based on driving the 4-layer Noah LSM (Ek et al., 2003) using observations and reanalysis fields. The precipitation forcing is a blended estimate combining pentad-mean CMAP data, the CPC daily-mean gauge-based analysis, and precipitation produced by the atmospheric model. The weights for the blending depend on location, and especially on latitude. The gauge-based analysis is given the largest weights in mid-latitudes, particularly in continental regions where the gauge network is dense. CMAP is given the largest weights in the tropics and the model estimate is given the largest weights at high latitudes. Other forcing data are taken from the coupled atmosphereocean reanalysis. The LSM is fully coupled to the atmosphere throughout the diurnal cycle, but the land surface analysis is performed only once per day (at 00UTC) for better consistency with the temporal resolution of the precipitation forcing.
NOAA-CIRES 20CR v2	Surface pressure is the only variable assimilated by the system; no land surface analysis is performed. The model is coupled to the 4-layer Noah LSM (Ek et al., 2003), which provides a representation of land surface processes that evolve in tandem with the atmospheric state.

Snow cover and its evolution have important impacts on climate (e.g., Cohen and Entekhabi, 1999), including the stratospheric circulation and its coupling with the troposphere (Orsolini and Kvamstø, 2009; Allen and Zender, 2011; Cohen et al., 2014). Table 2.16 summarizes the representation of snow in reanalyses. Several of the reanalysis systems produce analyzed snow cover and snow depth variables using station observations of snow depth. Observationally-based gridded analyses of snow cover and/or depth may be assimilated as additional constraints, used to help constrain the background state prior to assimilating station observations, or applied (when available) as the primary determinant for the presence or absence of snow. Four of the reanalyses (ERA-20C, MERRA, MERRA-2, NOAA-CIRES 20CR v2) simulate the evolution of snow using snow models forced by the atmospheric reanalysis and the land surface state, with no adjustment based on observational data.

Table 2.16: Treatment of snow in the reanalysis systems.

ERA-40	A snow analysis, including the albedo, depth, temperature, and density of snow, is performed outside of the main atmospheric reanalysis using Cressman interpolation with successive corrections. Snow is represented as an additional layer on top of the LSM with prognostic temperature and mass per unit area. Snow density is constant with depth but increases exponentially with snow age. Snow albedo reduces exponentially as snow ages over low vegetation or bare soil, but is constant in time for snow under high vegetation. Assimilated observations include station observations of snow depth and gridded estimates of snow cover from satellites. Observations of snow depth are limited to Canada before 1966 and to Canada and the former Soviet Union between 1966 and 1976 (Uppala et al., 2005). The snow depth analysis is relaxed toward a climatology when observations are unavailable.
ERA-Interim	A snow analysis, including the albedo, depth, temperature, and density of snow, is performed outside of the main atmospheric reanalysis using Cressman interpolation with successive corrections. Snow is represented as an additional layer on top of the LSM with prognostic temperature and mass per unit area. Snow density is constant with depth but increases exponentially with snow age. Snow albedo reduces exponentially as snow ages over low vegetation or bare soil, but is constant in time for snow under high vegetation. Observations used in the analysis include station observations of snow depth and, after 2003, the IMS gridded snow cover product, which combines optical and microwave satellite data and station data. The snow depth analysis is relaxed toward a climatology when observations are unavailable.
ERA-20C	Snow depth, albedo, temperature and density are simulated using the model described by Dutra et al. (2010). Snow is represented as an additional layer on top of the LSM with prognostic mass and heat contents. Unlike the models used in ERA-40 and ERA-Interim, the snow layer can contain liquid water, diagnosed as a function of temperature, mass, density, and rainfall interception (Dutra et al., 2010). Snow density is assumed to be constant with depth, and evolves according to parameterized representations of overburden, thermal metamorphism, and meltwater retention. Snow albedo reduces exponentially as snow ages over low vegetation or bare soil, and varies based on vegetation type for snow under high vegetation.

ERA5	A two-dimensional OI snow analysis, including the water equivalent, temperature, and density of snow, is performed outside of the main atmospheric reanalysis (de Rosnay et al., 2015). Snow is represented as an additional layer on top of the LSM with prognostic temperature and mass per unit area. The snow layer can contain liquid water, diagnosed as a function of temperature, mass, density, and rainfall interception (Dutra et al., 2010). Snow density is assumed to be constant with depth, and evolves according to parameterized representations of overburden, thermal metamorphism, and meltwater retention. Snow albedo reduces exponentially as snow ages over low vegetation or bare soil, and varies based on vegetation type for snow under high vegetation. Observations used in the analysis include station observations of snow depth and the IMS gridded snow cover product, which combines optical and microwave satellite data and station data. Unlike ERA-Interim, the IMS data are not used at high altitudes (above 1500 m) and the snow depth analysis is not relaxed toward a climatology when observations are unavailable.
JRA-25 / JCDAS	A separate OI snow depth analysis is performed once per day. The first-guess background state combines the land-surface analysis and gridded satellite observations. Weekly NOAA snow cover analyses are used in place of gridded satellite observations when the latter are unavailable. The analysis ingests in situ observations of snow depth from selected archives (Onogi et al., 2007).
JRA-55	A separate OI snow depth analysis is performed once per day. The first-guess background state combines the land-surface analysis, gridded satellite observations, and climatological values over ice sheets. Climatological values are also used in place of gridded satellite observations when the latter are unavailable. The analysis ingests in situ observations of snow depth from selected archives (Kobayashi et al., 2015).
MERRA	The evolution of snow mass, depth, and heat content is simulated within each LSM "catchment" (Table 2.15) using a three-layer snow model (Stieglitz et al., 2001). Density in each layer evolves via parameterized representations of compaction due to snow overburden and melting/refreezing. Snow is redistributed among layers as necessary to keep the surface layer shallow enough to respond to diurnal variability. The albedo of snow-covered land surface depends on snow density and vegetation type. Land ice sheets are represented simplistically, with a constant albedo, a constant near-surface temperature, and no overlying surface snow. No snow analysis is produced.

MERRA-2	The evolution of snow mass, depth, and heat content is simulated within each "catchment" (Table 2.15) using a three-layer snow model (Stieglitz et al., 2001). Density in each layer evolves via parameterized representations of compaction due to snow overburden and melting/refreezing. Snow is redistributed among layers as necessary to keep the surface layer shallow enough to respond to diurnal variability. The albedo of snow-covered land surface depends on snow density and vegetation type. A detailed representation of the surface properties of land ice sheets is introduced (Gelaro et al., 2017), including the evolution of overlying snow layers. No snow analysis is produced.
NCEP-NCAR R1	Snow is treated as a single layer of frozen water with a uniform density of $200\,\mathrm{kg\,m^{-3}}$. The presence of snow alters the snow-free albedo, which in turn depends on vegetation type. Weekly snow cover analyses from the NSIDC are used for the NH between 1967 and September 1998, after which they are replaced with daily analyses. Snow cover analyses are not available in the SH or in the NH before 1967; climatological constraints are used instead. Weekly analyses are not interpolated in time, so that snow variables change discontinuously every seven days. Model-simulated values of snow depth are ignored and replaced with the output of an empirical formula based on model temperature. Several errors in the representation of snow have been identified (Kistler et al., 2001; Kanamitsu et al., 2002). For example, the snow cover analysis mistakenly reused 1973 data for the entire 1974–1994 period, and conversion of snow to water during melting was overestimated by three orders of magnitude.
NCEP-DOE R2	Snow is simulated as a single layer of frozen water via a budget equation that accounts for accumulation and melting. A uniform snow density of $200\,\mathrm{kg\,m^{-3}}$ is assumed. Weekly analyses of NH snow cover from the NSIDC are interpolated to daily resolution until September 1998, after which they are replaced with daily analyses. Snow cover analyses are not available in the SH, where model-generated values are used instead. The model-predicted evolution of snow depth is used when it is consistent with the ingested snow cover analysis. When this condition is not met, snow is either removed or added, with snow depth in the latter case determined via an empirical formula that depends on model temperature.

CFSR / CFSv2	Snow is simulated using a three-layer snow model (Koren et al., 1999; Ek et al., 2003). The evolution of snow density accounts for compaction due to overburden and thermal effects, with adjustments applied for snowmelt and/or fresh snowfall. The albedo of snow-covered areas varies as a function of snow depth and vegetation type, with an allowance for patchy snow cover when snow depth is below a specified threshold. Simulated snow variables are evaluated and adjusted using external analyses of global snow depth and NH snow cover. These external analyses are not available for dates prior to February 1997, but are used to supplement and correct the snow depth analyses after this date. Model-estimated snow depths are only adjusted if they differ from the analysed depth by more than a factor of two, and are used as is when analysed values are not available. A prognostic snow layer is also included in the sea ice model.
NOAA-CIRES 20CR v2	Snow is simulated using a three-layer snow model (Koren et al., 1999; Ek et al., 2003). The evolution of snow density accounts for compaction due to overburden and thermal effects, with adjustments applied for snowmelt and/or fresh snowfall. The albedo of snow-covered areas varies as a function of snow depth and vegetation type, with an allowance for patchy snow cover when snow depth is below a specified threshold.

2.3 Assimilation Schemes

2.3.1 Basics of data assimilation

This section provides a brief overview of data assimilation concepts and methods as implemented in current reanalysis systems. More detailed summaries have been provided by Krishnamurti and Bounoua (1996), Bouttier and Courtier (2002), and Kalnay (2003), among others. In this context, an analysis is a best estimate of the true state of the atmosphere at a given time t. Reanalysis systems use objective analysis methods that employ mathematical optimization (data assimilation) techniques to combine model-generated forecasts and observed data, given constraints that are intended to preserve consistency. The results should be reproducible, internally consistent, and spatially continuous.

Data ingested into an analysis system may include observations and variables from a first guess background state (such as a previous analysis or forecast). Analysis systems are constructed to be consistent with known or assumed physical properties (such as smoothness, hydrostatic balance, geostrophic or gradient-flow balance, or more complex non-linear balances). Both the observations and the background state include important information, and neither should be considered as 'truth': both the model and observations include errors and uncertainties. An analysis system must therefore adopt a consistent and objective strategy for minimizing the differences between the analysis and the (unknown) true state of the atmosphere. Such strategies should on average reduce the errors and uncertainties associated with both observations and the first-guess background state. To this end, data assimilation algorithms often employ statistics to represent the range of potential uncertainties in the background state, observations, and any techniques used to convert between

model and observational space (i.e., observation operators), and ultimately aim to minimize these potential uncertainties.

An observation operator (also sometimes referred to as a "forward operator") is a function that converts information from the first guess background state space to the observation space, thus permitting direct comparisons between the model state and observed variables. Different types of observations require different types of observation operators. Key functions performed by observation operators include spatial interpolation from the model grid to observation locations and the transformation of model variables to observed quantities (i.e., the estimation of satellite radiances via the application of a radiative transfer model to the first guess profile; see also Table 2.19). Errors in the observation operators constitute a portion of the observation errors considered by the data assimilation scheme.

The analysis methods used by current reanalysis systems include variational methods (3D-Var and 4D-Var) and the ensemble Kalman filter (EnKF). Variational methods (e.g., Talagrand, 2010) minimize an objective cost function that simultaneously penalizes differences between the analysis and observations and differences between the analysis and the model background state, with consideration of uncertainties in both the observations and the model. Implementations of variational data assimilation may be applied to derive optimal states at discrete times (3D-Var), or to identify optimal state trajectories within finite time windows (4D-Var). In EnKF (e.g., Evensen, 2009), an ensemble of forecasts is used to define a set of background states (the prior ensemble), which is then combined with observations and associated uncertainties to derive a set of analysis states that is consistent with the posterior distribution. The optimal analysis states are determined by applying a Kalman filter (Kalman, 1960) to this posterior ensemble (see also Evensen and van Leeuwen, 2000). If a single analysis state is required, this is typically derived by averaging the ensemble members, although this approach yields fields that are spatially smoother than any of the individual ensemble members, particularly in regions of sharp gradients. One of the key advantages of 3D-Var, 4D-Var, and EnKF methods relative to many earlier implementations of data assimilation is the ability to account for indirect and possibly nonlinear relationships between observed quantities and analysis variables. This ability permits the direct assimilation of satellite radiance data without an intermediate retrieval step (Tsuyuki and Miyoshi, 2007), and underpins many of the recent advances in reanalysis development.

Figure 2.6 shows simplified one-dimensional schematic representations of four data assimilation strategies used by current reanalysis systems (3D-Var, 3D-FGAT, 4D-Var, and EnKF). In the following discussion, we frequently refer to the analysis increment, which is defined as the adjustment applied to the first guess (forecast) background state following the assimilation of observational data (i.e., the difference between the analysis state and the first guess background state). We also use the term observation increment, which refers to the difference between the observation and the background state after the observation operator is applied. This concept is also referred to in the literature as the observational 'innovation' (see detailed discussion by Kalnay, 2003). The analysis increment reflects the combined adjustment after evaluating and weighting (see also Section 2.4.2) all observation increments within an assimilation window, where the assimilation window is the time period containing observations that influence the analysis. The assimilation window used in reanalyses is typically between 6 and 12 hours long, and is often (but not always) centred at the analysis time. Core differences among the data assimilation strategies used in current reanalysis systems can be understood in terms of how the analysis increment is calculated and applied.

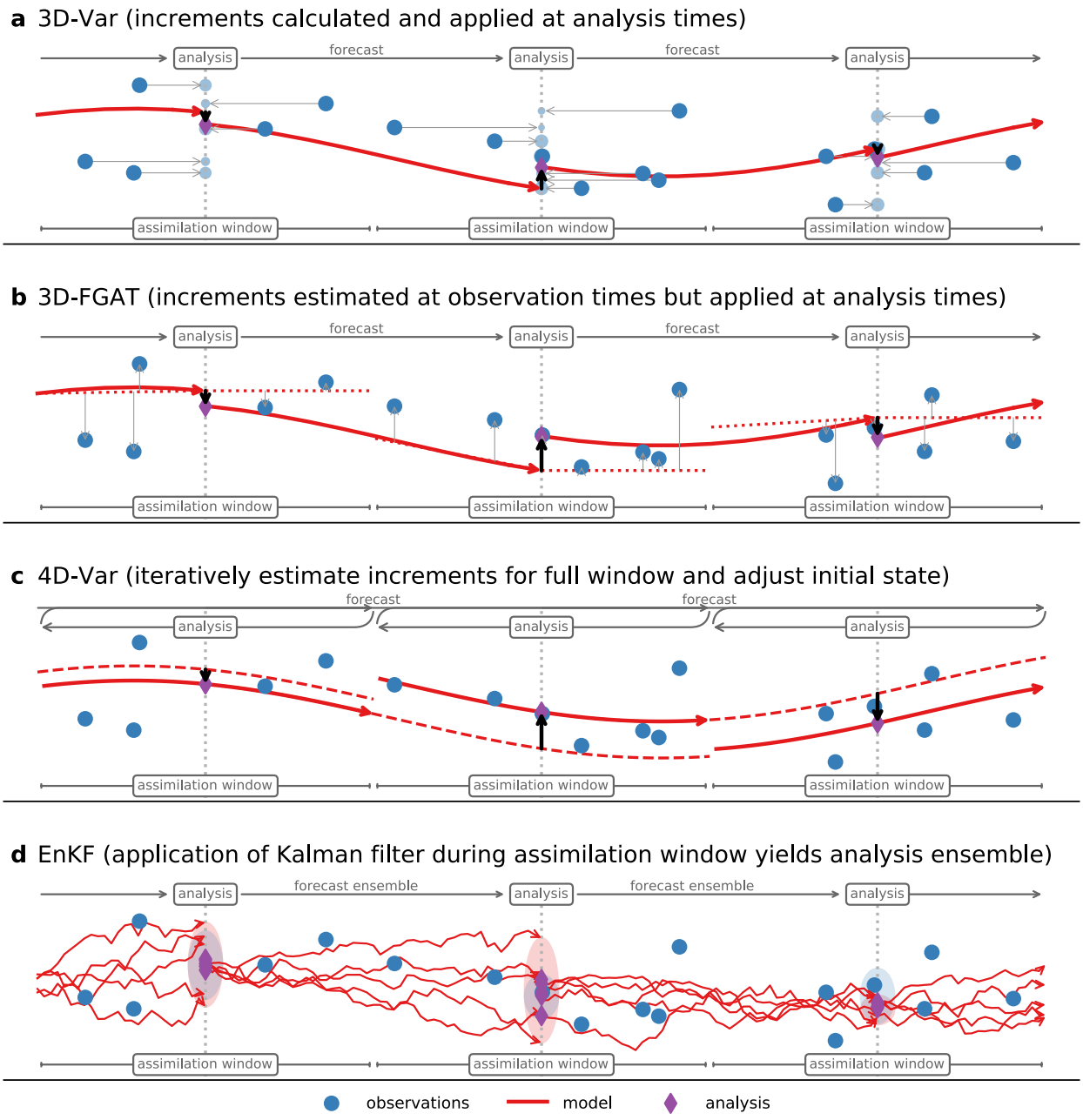

Figure 2.6: Simplified schematic representations of four data assimilation strategies used by current reanalyses: (a) 3D-Var; (b) 3D-FGAT (for clarity, this panel illustrates the 'semi-FGAT' approach used by NCEP-NCAR R1 and NCEP-DOE R2); (c) incremental 4D-Var; and (d) EnKF. Blue circles represent observations, red lines represent the model trajectory, and purple diamonds indicate the analysis. The dotted red lines in (b) represent linearly interpolated/extrapolated first guesses used to estimate increments at observation times. The dashed red lines in (c) represent the initial forecasts, prior to iterative adjustments. These illustrations are conceptual, and should not be taken as exact depictions of the much more complex strategies used by actual reanalysis systems.

The 3D-Var method (Figure 2.6a) calculates and applies analysis increments only at discrete analysis times. Observation increments within the assimilation window may either be treated as though they were all at the analysis time (which approximates the average observation time) or weighted by when they occurred (so that observations collected closer to the analysis time have a stronger impact on the analysis increment). JRA-25 uses a 3D-Var method for data assimilation under the former assumption, in which all observations within the assimilation window are treated as valid at the analysis time. In practice, many 3D-Var systems estimate observation increments at observation times rather than analysis times (Figure 2.6b). This approach is referred to as 3D-FGAT ("first guess at the appropriate time"; Lawless, 2010). The implementation of 3D-FGAT in reanalysis systems varies. For example, R1 and R2 can be thought of as "semi-FGAT" systems in that observation increments are estimated relative to a linear interpolation between the initial and final states of the forecast before the analysis time and relative to a constant state after the analysis time (i.e., these systems effectively use a pure 3D-Var approach for the portion of the assimilation window after the analysis time). The illustration provided in Figure 2.6b corresponds to this semi-FGAT approach. Other 3D-FGAT systems break each forecast into multiple piecewise segments of 30 minutes (ERA-40), one hour (CFSR), or three hours (MERRA and MERRA-2) in length. Observation increments are calculated by interpolating to observation times within each piecewise segment and then used to estimate analysis tendencies for each piecewise segment. These analysis tendencies are then combined to construct the full analysis increment.

MERRA and MERRA-2 include an additional step relative to other 3D-FGAT systems, and generate two separate sets of reanalysis products (designated "ANA" for the analyzed state and "IAU" for the incremental analysis update state) using an iterative predictor–corrector approach (Rienecker et al., 2011). The ANA products are analogous to the analyses produced by other 3D-FGAT systems, and are generated by using the data assimilation scheme to adjust the background state produced by a 12-h "predictor" forecast (from 9 h before the analysis time to 3 h after). The IAU products (also referred to as "ASM") have no analogue among other 3D-FGAT reanalyses. These latter products are generated by conducting a 6-h "corrector" forecast centered on the analysis time and using the IAU procedure (Bloom et al., 1996) to apply the previously calculated analysis increment gradually at each model time step rather than abruptly at the analysis time. The corrector forecast is then extended 6 h to generate the next predictor state. This iterative predictor–corrector procedure is illustrated in Figure 2.7. Note that the ASM state has only seen half of the analysis increment by the original analysis time, so that differences between the ASM and ANA states correspond to approximately half of the analysis increment. Moreover, the inclusion of the analysis increment as an additional tendency term may alter the physical tendency terms produced by the atmospheric model. For example, diabatic temperature tendencies produced by MERRA and MERRA-2 are archived during the corrector step rather than the predictor step. This arrangement applies to all tendency terms (moisture, momentum, ozone, etc.) and introduces a conceptual difference relative to the tendencies produced by other reanalyses (which are archived prior to the analysis during the initial forecast step), though it is important to emphasize that the analysis tendency is needed to close the budget in either case. For MERRA and MERRA-2, the ANA products represent the closest match to assimilated observations, while the ASM products provide a more complete and consistent suite of atmospheric variables and tendency terms with reduced wind and tracer imbalances relative to the 3D-FGAT analyzed state (see also Table 2.18 and associated discussion). ASM products should be used for transport simulations and other applications for which internal consistency is a priority (see also technical note on appropriate use of MERRA-

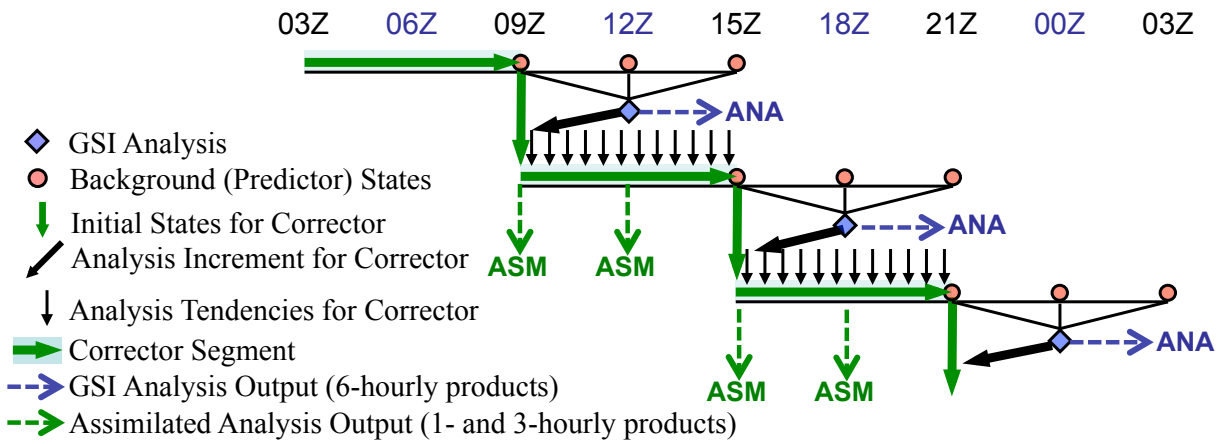

Figure 2.7: A schematic illustration of the DAS procedure used to create ANA products and the IAU procedure used to create ASM products as implemented in MERRA and MERRA-2 (modified from Rienecker et al., 2011). See text for details.

2 products at https://gmao.gsfc.nasa.gov/reanalysis/MERRA-2/docs/ANAvsASM.pdf). MERRA and MERRA-2 analysis increments for temperature, winds, water vapor, and ozone are included in a subset of the data products provided by these systems.

Unlike 3D-Var and 3D-FGAT, which attempt to optimize the fit between assimilated observations and the atmospheric state at discrete analysis times, 4D-Var (Figure 2.6c) attempts to optimize the fit between assimilated observations and the time-varying forecast trajectory within the full assimilation window (e.g., Park and Županski, 2003). 4D-Var makes more complete use of observations collected between analysis times than 3D-Var or 3D-FGAT, and has been shown to substantially improve the resulting analysis (Talagrand, 2010). However, the computational resources required to run a 4D-Var analysis are much greater than the computational resources required to run a 3D-Var or 3D-FGAT analysis, and the full implementation of 4D-Var remains impractical at present. Current reanalysis systems using 4D-Var (such as ERA-Interim, ERA-20C, ERA5, and JRA-55) therefore apply the simplified "incremental 4D-Var" approach described by Courtier et al. (1994). Under this approach, the model state at the beginning of the assimilation window is iteratively adjusted to obtain progressively better fits between the assimilated observations and the forecast trajectory. This iterative adjustment process propagates information both forward and backward in time, which benefits the analysis but requires the derivation and maintenance of an adjoint model. The latter is a difficult and time-consuming process, and is a significant impediment to the implementation of 4D-Var. Incremental 4D-Var is tractable (unlike full 4D-Var), but it is still computationally expensive, and is therefore usually implemented in two nested loops for computational efficiency. Analysis increments are first tested and refined in an inner loop using the tangent linear model and its adjoint with reduced resolution and simplified physics. This approach takes advantage of the fact that the cost function for the tangent linear model is perfectly quadratic, thus permitting the use of efficient optimization algorithms designed especially for quadratic functions. The final analysis increments are then applied in an outer loop with full resolution and full physics after the inner loop converges.

Most implementations of variational methods in reanalysis systems are based on single deterministic forecasts. By contrast, EnKF (Figure 2.6d) uses an ensemble approach to evaluate and

apply analysis increments, thus generating an ensemble of analysis states at each analysis time. Major advantages of the EnKF technique include ease of implementation (unlike 4D-Var, EnKF does not require an adjoint model) and the generation of useful estimates of analysis uncertainties, which are difficult to obtain when using variational techniques with single forecasts (ERA5 uses 4D-Var in a reduced-resolution 'ensemble of data assimilations' framework, in part to address this issue). Although the assimilation of satellite radiances presents some unique challenges in EnKF (Campbell et al., 2010; Polavarapu and Pulido, 2017), Whitaker et al. (2009) found that 4D-Var and EnKF perform comparably well in the case of a reanalysis that assimilates only surface pressure observations, and that both 4D-Var and EnKF give more accurate results than 3D-Var in this case. 20CR uses an EnKF method for data assimilation.

As discussed in section 2.2.4, some reanalyses use simpler methods (such as OI or Cressman interpolation) for certain types of data assimilation, especially analyses of screen-level meteorological variables or snow depth. In Cressman interpolation (Cressman, 1959), the analysis is iteratively 'corrected' toward the set of observed values, with weighted observation increments that reduce with distance according to a specified window function. The radius of influence defined by this window function is typically reduced on successive iterations so that the closest observations have the largest influence on the final analysis. OI (Gandin, 1963) is a linear combination of the available observations and the background state, with the weight of each contribution estimated in a way that aims to minimize the analysis error variance. OI is formulated as a multiple linear regression problem in which both the observations and the background state are assumed to be unbiased, with known random errors. Standard OI is a special case of two of the methods discussed above, and can be functionally equivalent to both 3D-Var (assuming linear observation operators and Gaussian errors) and to the Kalman filter (assuming constant background error covariance). Although the assumptions involved in Cressman interpolation and OI are rarely satisfied, they offer a flexibility in application that can be valuable for estimating analysis increments in variables with highly heterogeneous spatial distributions (such as surface air temperature).

The assimilation of observational data can introduce spurious artefacts into reanalyses of the state and variability of the upper troposphere, stratosphere, and mesosphere. For example, data assimilation can act to smooth sharp vertical gradients in the vicinity of the tropopause. The potential importance of this effect is illustrated by abrupt changes in vertical stratification near the tropopause at the beginning of the satellite era in R1 (Birner et al., 2006). Changes in data sources and availability can also lead to biases and artificial oscillations in temperature in various regions of the stratosphere, particularly in the polar and upper stratosphere where observations are sparse (Randel et al., 2004; Uppala et al., 2005; Simmons et al., 2014; Lawrence et al., 2015). Information and errors introduced by the input data and data assimilation system propagate upwards through the middle atmosphere in both resolved waves and parametrized gravity wave drag (Polavarapu and Pulido, 2017). The effects of this propagation are often but not always undesirable. The abrupt application of analysis increments can generate spurious gravity waves in systems that use intermittent data assimilation techniques (Schoeberl et al., 2003), including most implementations of 3D-Var, 3D-FGAT, and EnKF, and may also generate instabilities that artificially enhance mixing and transport in the subtropical lower stratosphere (Tan et al., 2004). Reanalyses of the stratosphere and mesosphere are therefore quite sensitive to the details of the data assimilation scheme and input data at lower altitudes.

Additional details regarding all of the methods mentioned in this section, including relative advantages and disadvantages, have been discussed and summarized by Park and Županski (2003),

Lorenc and Rawlins (2005), Kalnay et al. (2007a,b), Gustafsson (2007), and Buehner et al. (2010a,b), among others.

2.3.2 Data assimilation in reanalysis systems

Table 2.17 summarizes the schemes used for atmospheric data assimilation in the reanalysis systems, which include variations on the 3D-Var, 3D-FGAT, 4D-Var, and EnKF techniques.

Table 2.17: List of assimilation schemes used for atmospheric analyses.

ERA-40	3D-FGAT with a 9-h forecast step ending 3 h after the analysis time and a 6-h assimilation window centered on the analysis time. Analysis tendencies are calculated in 30-minute windows and then combined to construct the analysis increment.
ERA-Interim	Incremental 4D-Var atmospheric analysis with 12-h assimilation windows extending from 09 UTC to 21 UTC and from 21 UTC to 09 UTC. Analysis increments are calculated on coarser grids that approach the model resolution over successive iterations.
ERA-20C	Incremental 4D-Var analysis with 24-h assimilation windows extending from 09 UTC to 09 UTC. Assumed background error covariances are invariant in time, although a scaling is applied for consistency with time-varying background errors produced by an earlier 10-member ensemble pilot reanalysis that also assimilated only surface observations (Poli et al., 2013, 2016).
ERA5	Incremental 4D-Var atmospheric analysis with 12-h assimilation windows extending from 09 UTC to 21 UTC and from 21 UTC to 09 UTC. A 10-member 'ensemble of data assimilations' is conducted on a coarser grid, providing more robust estimates of analysis uncertainties and background error covariances.
JRA-25 / JCDAS	3D-Var (not 3D-FGAT) with 6-h forecast steps. Observations from 3 h before the analysis to 3 h afterwards are considered.
JRA-55	Incremental 4D-Var with a 9-h forecast step that extends 3 h past the analysis time and a 6-h assimilation window centered on the analysis time. Analysis increments are calculated on a coarser T106/F80 inner grid (rather than the T_L319/N160 outer grid used in the forecast model) to limit computational expense.
MERRA	GSI with IAU (Bloom et al., 1996), with 6-h assimilation windows centered on each analysis time. The IAU procedure (illustrated in Figure 2.7) is summarized in the text. The humidity variable used for the assimilation is pseudo-relative humidity, which is defined as the water vapour mixing ratio divided by the saturation mixing ratio of the background field (i.e., pseudo-RH does not change if no observations of moisture are assimilated, even with a non-zero analysis increment in temperature).

MERRA-2	GSI with IAU as in MERRA, but with updated background error specifications. The humidity variable used for the assimilation is the same pseudo-RH as in MERRA but normalized by the background error standard deviation. This normalization leads to a more Gaussian error distribution. A global constraint is imposed on the analysis increment of total water (Takacs et al., 2015).
NCEP-NCAR R1	SSI in a 3D-Var 'semi-FGAT' configuration (see text) with a 6-hour assimilation window centered on each analysis time. For times before the analysis time, first guesses are based on linear interpolation between the initial and final model states. For times after the analysis time, first guesses are estimated as the first guess at the analysis time.
NCEP-DOE R2	SSI in a 3D-Var 'semi-FGAT' configuration (see text) with a 6-hour assimilation window centered on each analysis time. For times before the analysis time, first guesses are based on linear interpolation between the initial and final model states. For times after the analysis time, first guesses are estimated as the first guess at the analysis time.
CFSR / CFSv2	GSI with 9-h forecasts (from 6 h before to 3 h after each analysis time) and 6-h assimilation windows (centered on each analysis time). The implementation of GSI in CFSR is a form of 3D-FGAT with hourly first guesses.
NOAA-CIRES 20CR v2	EnKF with a 6-h window centered on each analysis time. Observations from 3 h before the analysis time to 3 h afterwards are used. The EnKF implementation in 20CR uses a window that straddles the analysis time, and is therefore technically an Ensemble Kalman Smoother (Compo et al., 2011).

As noted in the previous section, the application of analysis increments can generate spurious instabilities in the atmospheric state, particularly when these increments are applied intermittently (as in 3D-Var). Several methods have been developed to mitigate these effects, including nonlinear normal mode initialization techniques and the application of digital filters. Nonlinear normal mode initialization (Machenhauer, 1977; Daley, 1981) limits the impacts of spurious instabilities by reducing or eliminating the tendencies associated with all "fast-mode" disturbances (i.e., gravity waves) in the vertical and horizontal domains. By contrast, digital filter initialization (Lynch, 1993) aims to reduce or eliminate high-frequency noise in the temporal domain. Both approaches can be applied as strong constraints (in which all potentially undesirable modes are eliminated) or as weak constraints (in which potentially undesirable modes are penalized rather than eliminated entirely).

Certain data assimilation techniques also aim to reduce the impacts of spurious instabilities and/or eliminate the need for initialization techniques. For example, one of the benefits of the SSI analysis technique (Parrish and Derber, 1992) developed at NCEP and used in R1 and R2 was that it imposed a global balance constraint on the analysis that eliminated the need for nonlinear normal mode initialization (Kalnay et al., 1996). It should be noted, however, that balance constraints and filters (particularly those applied as strong constraints) may eliminate real information along with spurious noise. The loss of this information can have particularly detrimental effects in the middle

atmosphere, where gravity waves that propagate upward from lower levels play important roles in the dynamics (Polavarapu and Pulido, 2017). The application of IAU, as in MERRA and MERRA-2, can help to eliminate spurious instabilities without affecting other "fast-mode" disturbances in the model atmosphere. The use of IAU has been shown to improve the representation of the mesosphere in data assimilation systems (e.g., Sankey et al., 2007).

Table 2.18: Initialization procedures used to mitigate assimilation-driven instabilities.

ERA-40	Nonlinear normal mode initialization
ERA-Interim	Weak constraint digital filter
ERA-20C	Weak constraint digital filter
ERA5	Weak constraint digital filter
JRA-25 / JCDAS	Nonlinear normal mode initialization
JRA-55	None
MERRA	IAU
MERRA-2	IAU
NCEP-NCAR R1	None
NCEP-DOE R2	None
CFSR / CFSv2	6-h digital filter (Lynch and Huang, 1992)
NOAA-CIRES 20CR v2	None

The assimilation of observed satellite radiances by a reanalysis system requires the use of a radiative transfer model. This scheme typically differs from that used in the forecast model (Table 2.4). Table 2.19 lists the radiative transfer schemes used by each reanalysis system for assimilating satellite radiances.

Table 2.19: List of radiative transfer schemes used for assimilating satellite radiances.

ERA-40	RTTOV-5 is used for assimilating satellite radiances.
ERA-Interim	RTTOV-7 is used for assimilating satellite radiances.
ERA-20C	Satellite radiances are not assimilated (see also Table 2.21).
ERA5	RTTOV-11 is used for assimilating satellite radiances. Note that where ERA-40 and ERA-Interim only assimilated radiances under clear-sky conditions (see also Table 2.23), ERA5 assimilates all-sky radiances from certain sensors.
JRA-25 / JCDAS	RTTOV-6 is used for assimilating TOVS radiances and RTTOV-7 is used for assimilating ATOVS radiances.
JRA-55	RTTOV-9 is used for assimilating satellite radiances.
MERRA	The GLATOVS radiative transfer model is used for assimilating SSU radiances; the CRTM is used for assimilating all other satellite radiances.
MERRA-2	All radiances are assimilated using version 2.1.3 of the CRTM.
NCEP-NCAR R1	Satellite radiances are not assimilated (see also Table 2.21).
NCEP-DOE R2	Satellite radiances are not assimilated (see also Table 2.21).
CFSR / CFSv2	The CRTM developed at NOAA/NESDIS and the JCSDA is used for assimilating satellite radiances.
NOAA-CIRES 20CR v2	Satellite radiances are not assimilated (see also Table 2.21).

2.4 Observational Data

2.4.1 Summary of the basic information

This section provides information on key observational data assimilated in the reanalysis systems. Reanalysis systems assimilate observational data from a variety of sources. These sources are often grouped into two main categories: conventional data (e.g., surface records, radiosonde profiles, and aircraft measurements) and satellite data (e.g., microwave and infrared radiances, atmospheric motion vectors inferred from satellite imagery, and various retrieved quantities).

The densities and distributions of both types of observational data have changed considerably over time. Figure 2.8 shows examples of the spatial distributions of observations assimilated by JRA-55 in the 1980s (00UTC, 22 September 1983), while Figure 2.9 shows examples of the spatial distributions of observations assimilated by the same reanalysis system approximately 30 years later (00UTC, 23 June 2010). These two sets of examples are representative of the distribution and number of observations assimilated in most recent reanalysis systems (with the notable exception of ERA-20C and 20CR, which do not assimilate upper-air observations). Figures 2.10 through 2.13 summarize the availability of different types of observations assimilated in five of the most recent reanalysis systems as a function of time. Figure 2.14 provides a more detailed look at how the availability of radiances observed by certain instruments changes as satellites are launched and retired. Common codes and terminology for assimilated observations are listed in Table 2.20.

A number of key features are apparent in Figures 2.8 through 2.14. First, conventional in-situ data (such as surface, radiosonde, and aircraft data) are unevenly distributed in space. Second, satellite data (microwave and infrared sounder data, air motion vector data from geostationary and polar satellites, etc.) are often more evenly distributed but still inhomogeneous in space. Third, none of these datasets are continuous and homogeneous in time. For example, microwave and infrared sounders (i.e., the TOVS suite) were introduced in 1979, while advanced sounders (i.e., the ATOVS suite) were introduced in 1998. Such changes in the availability of observational data for assimilation have strong impacts on the quality of the reanalysis datasets that assimilate them, so that discontinuities in reanalysis data should be carefully evaluated and checked for coincidence with changes in the input observations. The quality of a given type of measurement is also not necessarily uniform in time; for example, virtually all radiosonde sites have adopted different instrument packages over time (see section 2.4.3.1), while TOVS and ATOVS data were collected using several different sounders on several different satellites with availability that changed over time (see Figure 2.14 and section 2.4.3.2). Finally, Figures 2.10 through 2.13 show that, although modern reanalysis systems assimilate observations from many common sources, different reanalysis systems assimilate different subsets of the available observations. Such discrepancies are particularly pronounced for certain categories of satellite observations and, like differences in the underlying forecast models, are an important potential source of inter-reanalysis differences.

Table 2.20: List of codes/acronyms for selected observations assimilated by reanalysis systems.

SYNOP (conventional)	Surface meteorological observation reported by manned and automated weather stations.
SHIP (conventional)	Surface meteorological observations reported by ships.
BUOY (conventional)	Surface meteorological observations reported by buoys.

PAOBS (conventional)	Surface pressure bogus data for the southern hemisphere produced by human analysts in the Australian Bureau of Meteorology who estimate sea level pressure based on satellite imagery, conventional data, and temporal continuity.
AMV (satellite)	Atmospheric motion vectors derived by tracing the movement of individual cloud or water vapour features in successive images from geostationary and polar-orbiting satellites.

Timelines of conventional data assimilated by reanalyses are quite consistent among recent full-input reanalyses (Figure 2.10), as well as the conventional input JRA-55C (not shown). All of the reanalysis systems discussed in this chapter assimilate records of surface pressure from manned and automated weather stations, ships, and buoys, while all but 20CR assimilate at least some records of surface winds over oceans. All but ERA-Interim, ERA5, ERA-20C, 20CR, and JRA-55C assimilated synthetic surface pressure data for the Southern Hemisphere (PAOBS) through at least 2009. PAOBS are subjective analyses of surface pressure produced by the Australian BOM based on available observations and temporal continuity, which are used to compensate for the scarcity of direct observations in the Southern Hemisphere. The influence of these data in reanalysis systems has waned in recent years, as the availability of direct observations covering the Southern Hemisphere has expanded. All of the full input reanalyses and JRA-55C assimilate upper-air observations made by radiosondes, dropsondes, and wind profilers. JRA-25, JRA-55, and JRA-55C assimilate wind speed profiles in tropical cyclones, while 20CR assimilates records of tropical cyclone central pressures. CFSR uses the NCEP tropical storm relocation package (Liu et al., 1999) to relocate tropical storm vortices to observed locations. ERA5 assimilates bogus vortex data before 1979 to improve its representation of tropical cyclones during the pre-satellite era. ERA-40, ERA-Interim, MERRA, MERRA-2, NCEP-NCAR R1, and NCEP-DOE R2 have no special treatments for tropical cyclones.

Timelines of satellite data assimilated by recent reanalysis systems are more varied (Figures 2.11 through 2.13; see also Figures 4.1 and 4.2 in Chapter 4 of the S-RIP report), but still include many commonalities. The core satellite data assimilated by most reanalyses are microwave and infrared radiances (or retrievals, in the case of NCEP-NCAR R1 and NCEP-DOE R2) from a variety of instruments. All of the full input reanalyses (including R1 and R2) also assimilate atmospheric motion vector (AMV) data derived from geostationary and polar-orbiting satellite imagery. Many of the more recent systems assimilate GNSS-RO data, while MERRA-2 assimilates temperature retrievals from Aura MLS at pressures 5 hPa and less. Additional information on satellite ozone retrievals assimilated by reanalyses is discussed in Chapter 4 of the S-RIP report. Table 2.21 lists special features of each reanalysis system regarding observational data assimilated.

Table 2.21: Special features regarding observational data assimilated in each reanalysis system (see also Figures 2.10 through 2.13 for five of the most recent full input reanalyses).

ERA-40	SSM/I total column water vapor and surface wind retrievals were assimilated. Neither GNSS-RO data nor AIRS radiances were assimilated (ERA-40 effectively predates these data types). No special treatment for tropical cyclones was included.

ERA-Interim	GNSS-RO bending angles and AIRS radiances are assimilated. Unlike ERA-40, SSM/I radiances are assimilated directly (in place of TCWV and surface wind retrievals). No special treatment for tropical cyclones is included.
ERA-20C	ERA-20C assimilated surface pressure observations from ISPD (Cram et al., 2015) and surface pressure and surface wind observations from ICOADS (Woodruff et al., 2011). Reports that appear in both the ISPD and ICOADS databases were taken from ICOADS, with the ISPD report discarded. Tropical cyclone best track data were assimilated, but with relatively large rejection rates during quality control (Poli et al., 2016).
ERA5	GNSS-RO bending angles are assimilated. AIRS radiances are assimilated, as are hyperspectral radiances observed by IASI and CrIS, microwave soundings from ATMS, and infrared and microwave radiances from several sounding instruments on the Chinese FY-3 series of meteorological satellites. Radiances from several microwave imagers are assimilated directly, including SSM/I and SSMIS, TMI, and GMI, as well as visible and infrared radiances from AHI. Variational bias corrections have been added for ozone, aircraft measurements, and surface pressure. Bogus data are assimilated to improve the representation of tropical cyclones in the pre-satellite era.
JRA-25 / JCDAS	Total column water vapor retrievals from SSM/I and AMSR-E were assimilated, as were wind profile retrievals in tropical cyclones. SSM/I surface winds, GNSS-RO data, and AIRS radiances were not assimilated.
JRA-55	GNSS-RO refractivity data are assimilated, as are wind profile retrievals in tropical cyclones. Clear-sky radiances from selected channels of microwave imagers such as SSM/I, TMI, and AMSR-E are assimilated over ocean (Kobayashi et al., 2015). Neither SSM/I surface winds nor hyperspectral radiances were assimilated.
MERRA	AIRS radiances were assimilated, as were rain rates from SSM/I and TMI. SSM/I radiances were assimilated through late 2009, and surface winds were assimilated throughout. GNSS-RO data were not assimilated and no special treatment for tropical cyclones was included.

MERRA-2	GNSS-RO bending angles are assimilated up to 30 km. AIRS radiances are assimilated, as are hyperspectral radiances observed by IASI and CrIS and microwave soundings from ATMS. MLS temperature retrievals are assimilated above 5 hPa (version 3.3 through 31 May 2015; version 4.2 from 1 June 2015). A new adaptive bias correction scheme is applied to aircraft observations (see also Section 2.4.3.3). Assimilated aerosol optical depths are also bias-corrected. Rain rates from SSM/I and TMI and satellite observations of AOD are assimilated, as are SSM/I surface wind retrievals. SSM/I radiances were assimilated through late 2009. No special treatment for tropical cyclones was included.
NCEP-NCAR R1	Temperature retrievals from microwave and infrared sounders are assimilated, rather than radiances. The horizontal and vertical resolutions of temperature retrievals are downgraded to reduce the weight given to satellite data in recent analyses. Satellite moisture retrievals and SSM/I surface winds are not assimilated.
NCEP-DOE R2	Temperature retrievals from microwave and infrared sounders are assimilated, rather than radiances. The horizontal and vertical resolutions of temperature retrievals are downgraded to reduce the weight given to satellite data in recent analyses. Satellite moisture retrievals and SSM/I surface winds are not assimilated. No special treatment for tropical cyclones was included.
CFSR / CFSv2	GNSS-RO bending angles and radiances from AIRS and IASI are assimilated. SSM/I radiances are not assimilated, but surface wind retrievals are. The NCEP tropical storm relocation package is applied to relocate tropical storm vortices to observed locations. No special treatment for tropical cyclones was included.
NOAA-CIRES 20CR v2	Only observations of surface pressure, sea level pressure, and tropical cyclone central pressure were assimilated. No upper-air or satellite data were assimilated.

2.4.2 Quality control procedures

The observations assimilated by reanalyses are subjected to rigorous quality control procedures that are intended to prevent the introduction of errors into the analysis. Key steps in the quality control algorithm for each reanalysis are listed in Table 2.22. Common quality control procedures are briefly described in the following paragraphs (see also Kalnay, 2003).

The typical first step in quality control is preliminary screening. This step eliminates observations with incomplete or duplicate data records, as well as observations that have previously been 'blacklisted' by either the data provider or the reanalysis center. Many data assimilation systems include automated procedures that try to correct incomplete data records to reduce the number of observations that are eliminated at this stage. The preliminary screening is typically followed by tests to identify and exclude data with physically unreasonable values. The latter may take several different forms. The simplest, the 'gross check', involves comparison against climatological values. Observations are excluded from the analysis if the gross check indicates that they differ from the expected value by more than a specified threshold amount. This type of test may be supple-

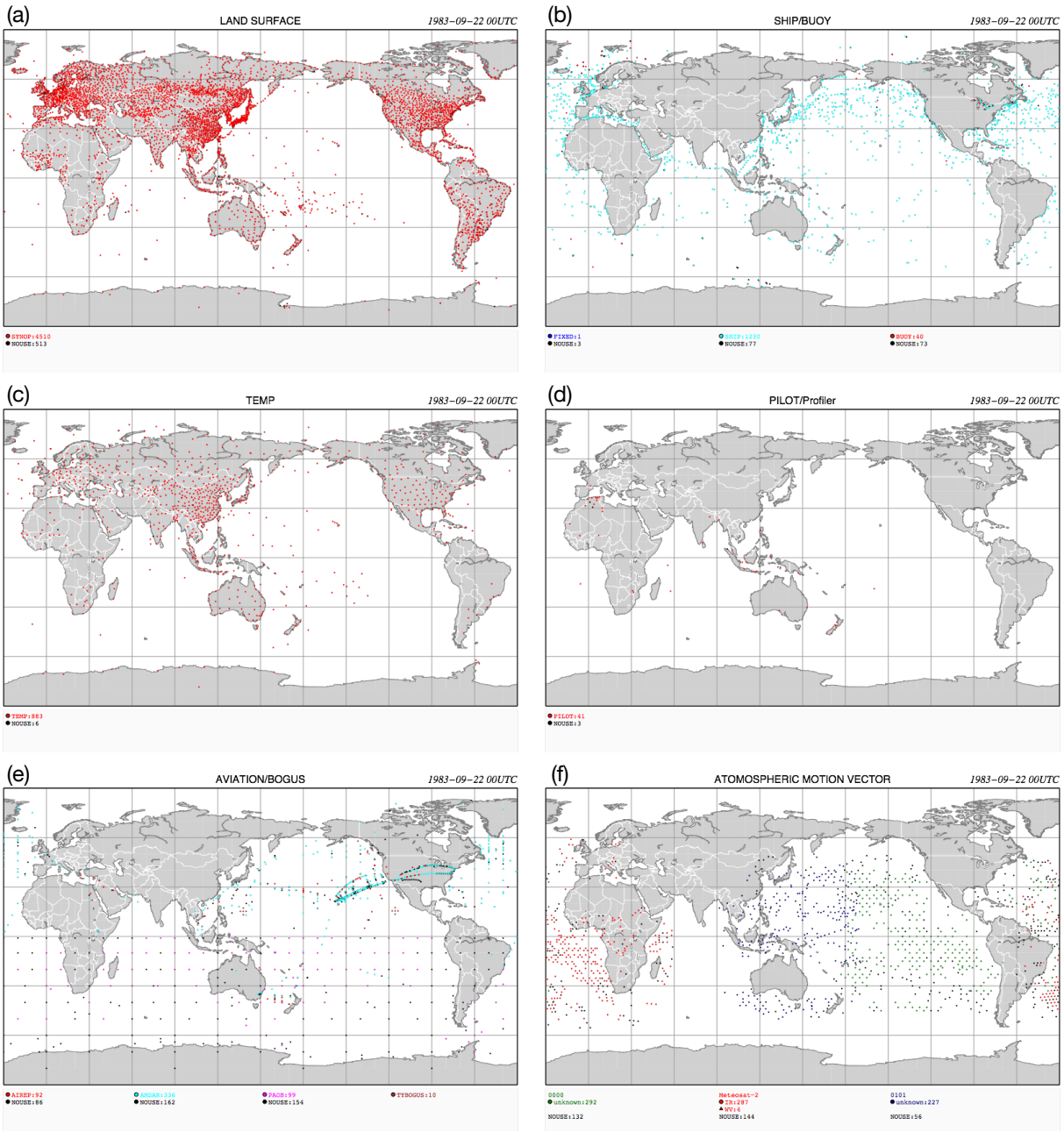

Figure 2.8: Observations assimilated by JRA-55 at 00UTC 22 September 1983 (±3 hours): (a) land surface data, (b) surface meteorological data reported by ships and buoys, (c) radiosonde profiles, (d) pilot balloons, (e) aircraft, PAOBS, and tropical cyclone wind retrievals, and (f) atmospheric motion vectors from METEOSAT, GMS, and GOES satellites.

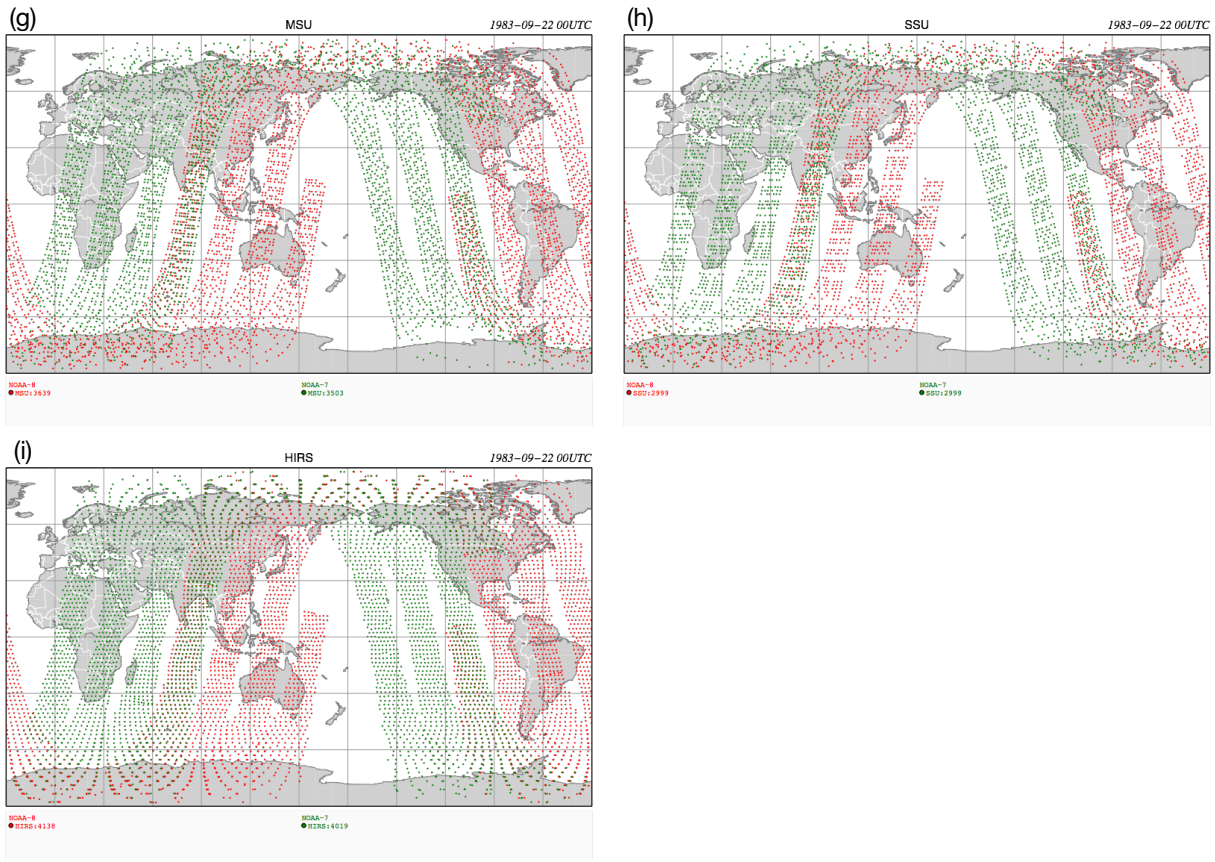

Figure 2.8 (cont.): (g) Microwave temperature sounder radiances from NOAA satellites, (h) stratospheric temperature sounder radiances from NOAA satellites, and (i) infrared sounder radiances (sensitive to temperature and moisture) from NOAA satellites.

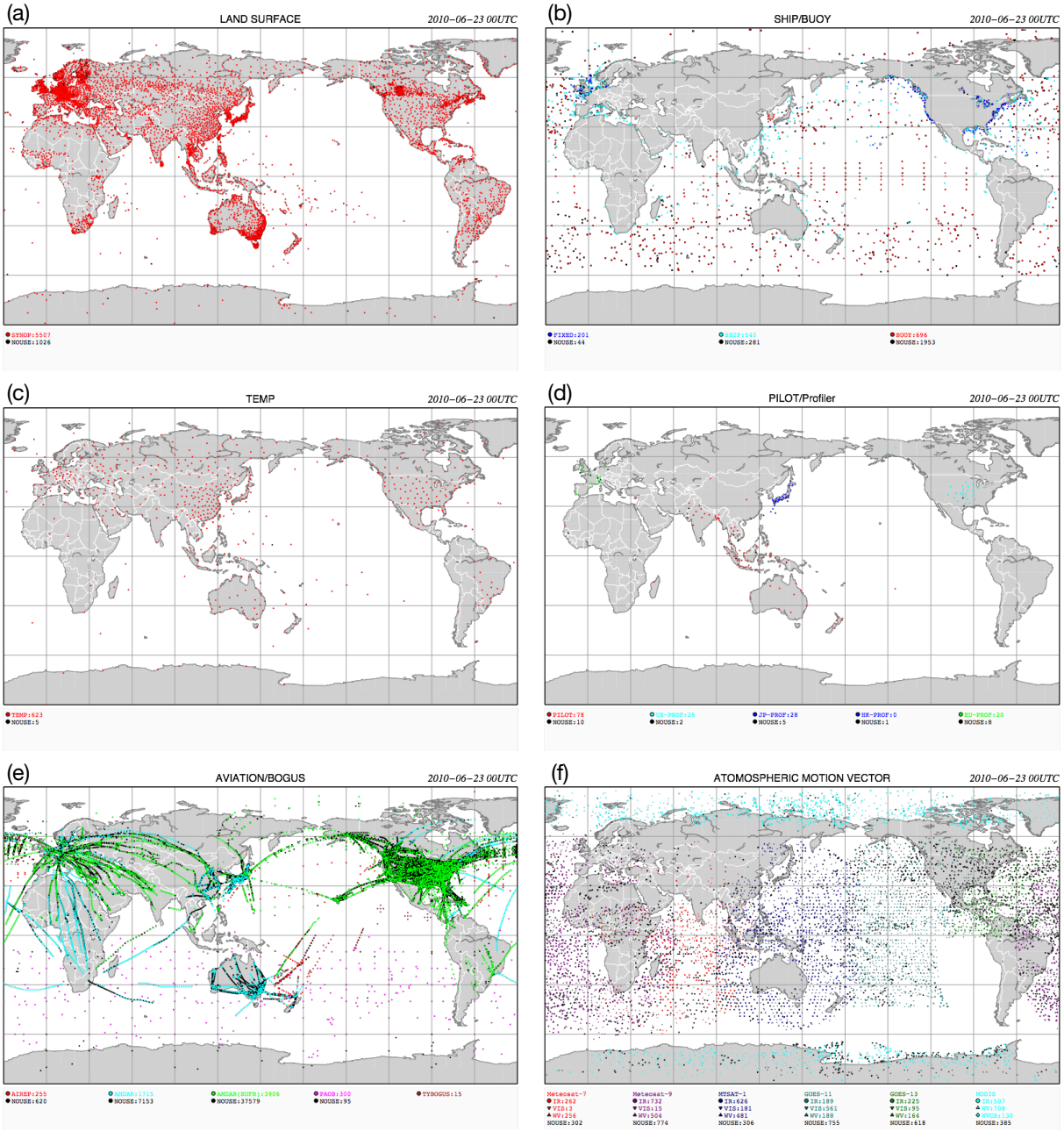

Figure 2.9: Observations assimilated by JRA-55 at 00UTC 23 June 2010 (±3 hours): (a) land surface data, (b) surface meteorological data reported by ships and buoys, (c) radiosonde profiles, (d) pilot balloons and wind profilers, (e) aircraft, PAOBS, and tropical cyclone wind retrievals, and (f) atmospheric motion vectors from the METEOSAT, MTSAT, GOES, Aqua, and Terra satellites.

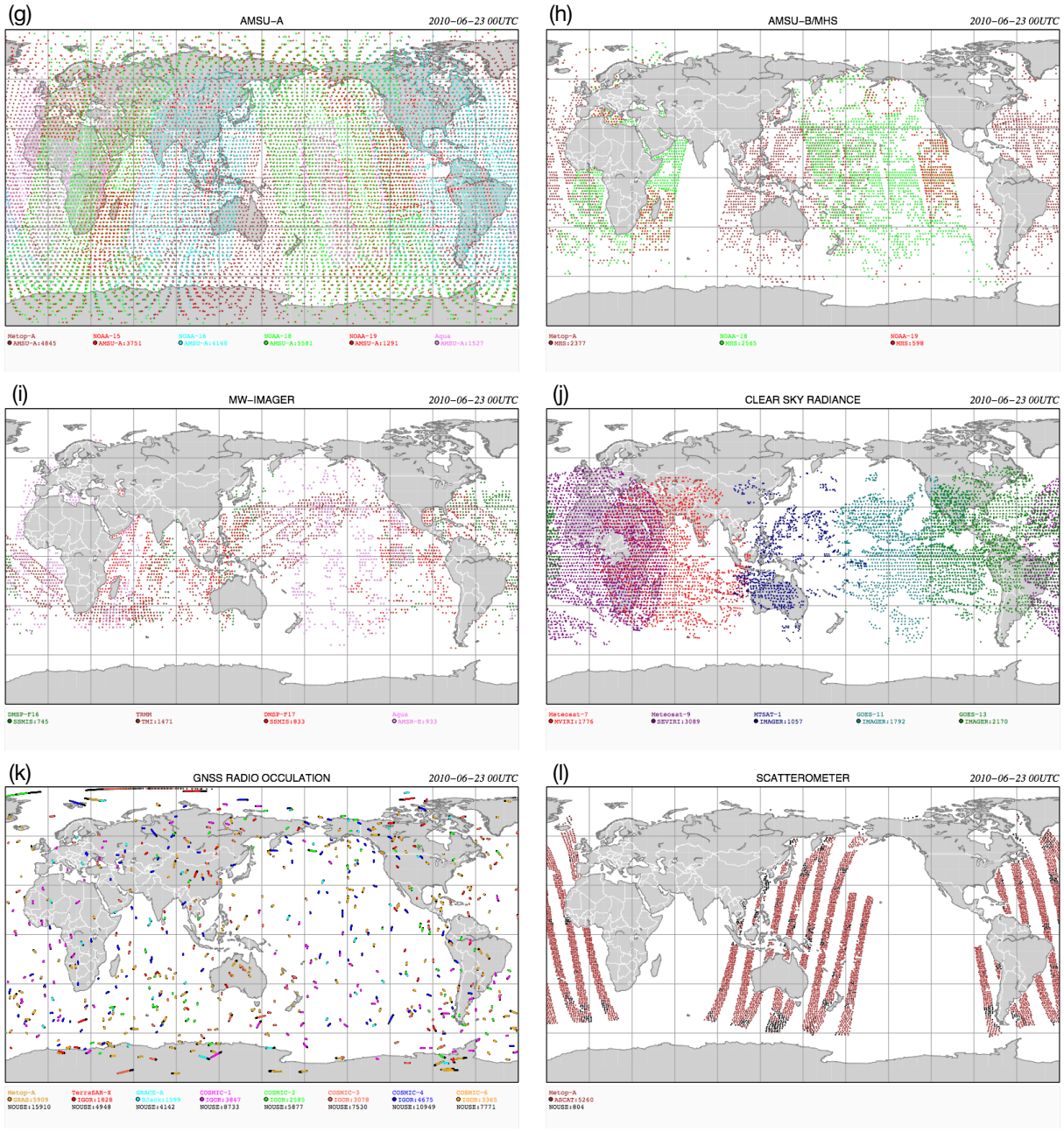

Figure 2.9 (cont.): (g) microwave temperature sounder radiances from the NOAA, MetOp, and Aqua satellites, (h) microwave humidity sounder radiances from NOAA and MetOp satellites, (i) microwave imager radiances (sensitive to moisture) from the DMSP, TRMM, and Aqua satellites, (j) clear-sky radiances from METEOSAT, MTSAT, and GOES satellites, (k) GNSS-RO refractive index data (sensitive to temperature and moisture) from the COSMIC, GRACE, MetOp, and TerraSAR-X satellites, and (l) ocean surface winds from MetOp (ASCAT scatterometer).

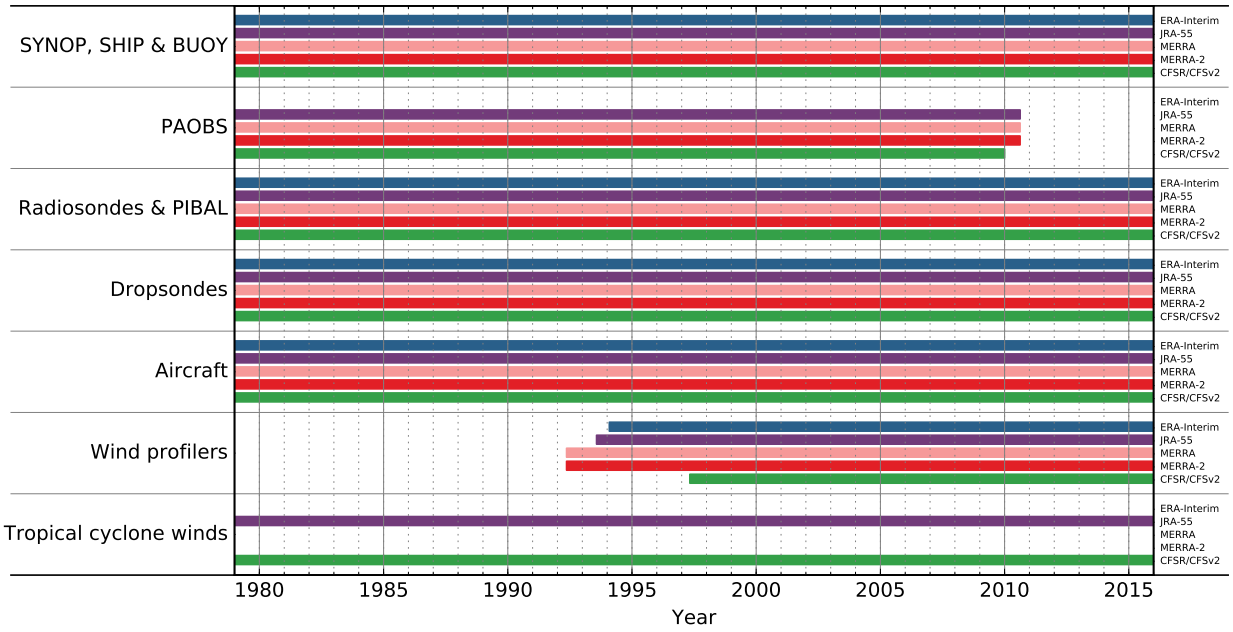

Figure 2.10: Availability of conventional observations assimilated by ERA-Interim (blue), JRA-55 (purple), MERRA (light red), MERRA-2 (dark red), and CFSR (green) reanalysis systems as a function of time. See Table 2.20 and Appendix B for acronym definitions.

mented (or superseded) by comparison to other reasonable expected values, such as the average of other nearby observations (i.e., a 'buddy check') or the forecast background state itself. These comparisons may also be combined, for instance by performing a simple OI analysis using nearby observations (except for the observation being evaluated) and then checking for consistency between the observation and the result of the OI analysis. One benefit of this kind of approach is that it can applied iteratively, rescuing data that might have been excluded by comparison to the initial background state or eliminating data that passed the initial checks but is too far from the OI analysis. In addition to expected values, observations may be checked for consistency with expected balance criteria. For example, height measurements might be compared against heights calculated from virtual temperature measurements via the hypsometric equation. Complex quality control refers to the common practice of applying these checks in combination, and then using an algorithm to decide whether each observation should be included or excluded.

The quality control procedures described above are used to pre-select observational data for use in the analysis. Many 3D-Var and 4D-Var data assimilation systems use variational quality control (Anderson and Järvinen, 1999), in which observations that are far from the expected value are penalized in the analysis rather than eliminated entirely. This means that observations that fail to meet the desired criteria have less impact on the analysis but may still be used, especially in regions where observations are sparse. Data pre-selection and variational quality control are not mutually exclusive. For example, ERA-Interim conducts a preliminary screening for incomplete, duplicate, and blacklisted data records before starting the incremental 4D-Var assimilation. The initial iterations of the assimilation (see Section 2.3) are then conducted without variational quality control, so that all observations that meet the pre-selection criteria are weighted equally. Variational quality control is then turned on for the later iterations of the assimilation to limit the

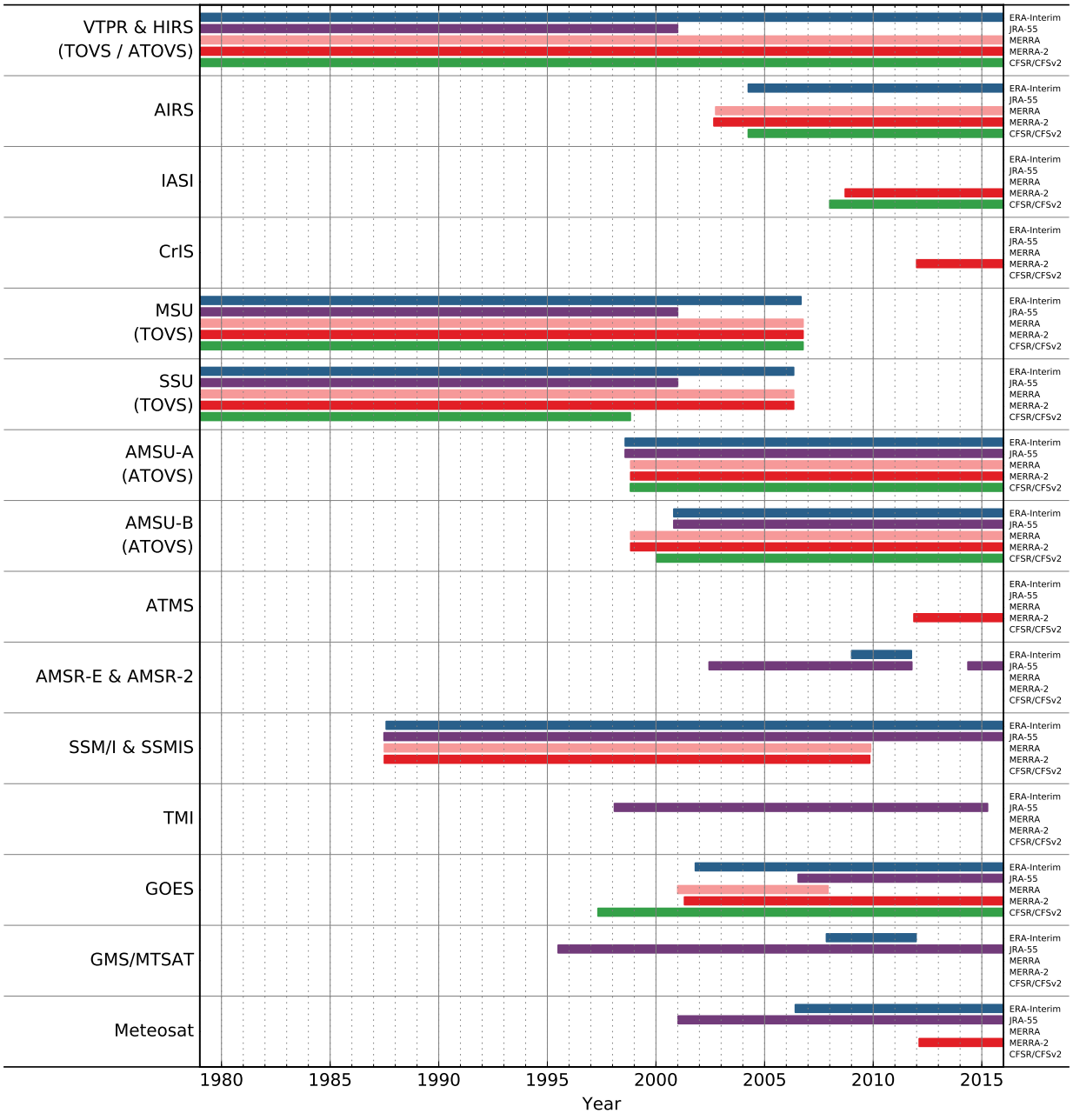

Figure 2.11: As in Figure 2.10, but for satellite radiances assimilated by the reanalysis systems.

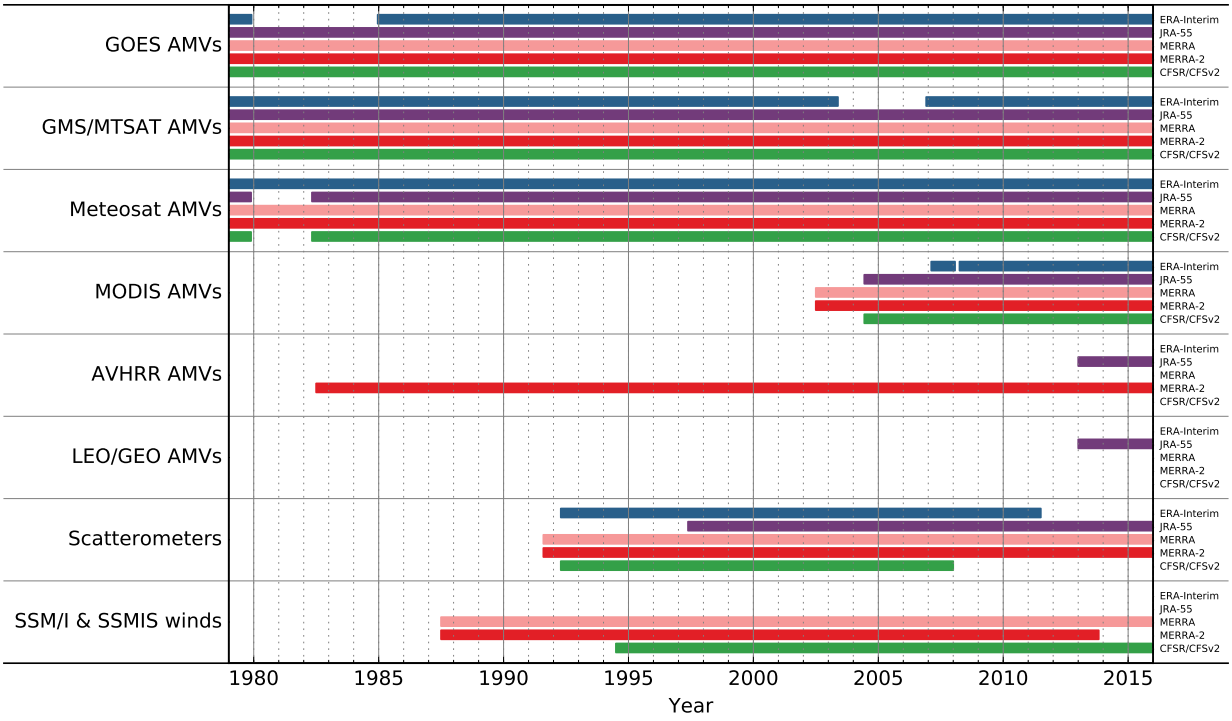

Figure 2.12: As in Figure 2.10, but for AMVs and ocean surface wind products derived from satellites and assimilated by the reanalysis systems.

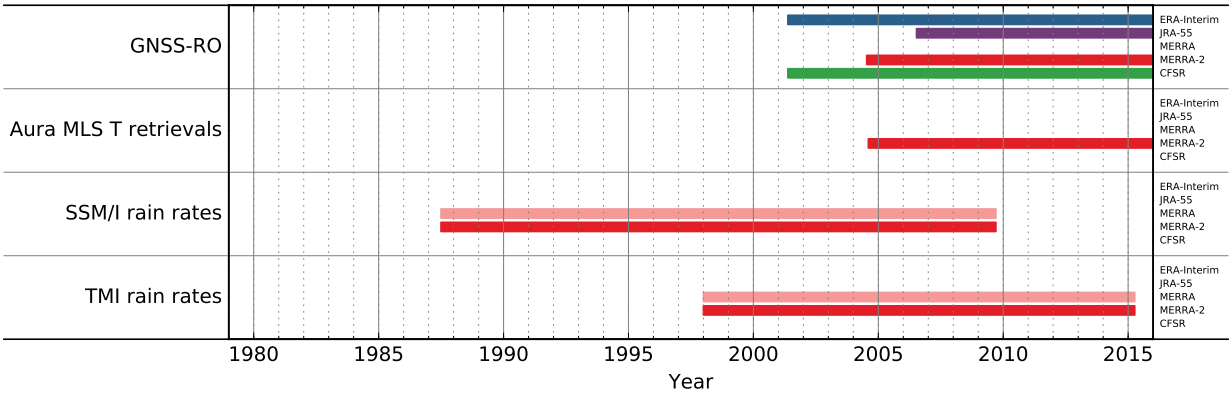

Figure 2.13: As in Figure 2.10, but for other types of satellite observations assimilated by the reanalysis systems. Timelines of satellite retrievals of total column ozone and ozone profiles assimilated by the reanalysis systems are provided in Chapter 4 of the S-RIP report (Figures 4.1 and 4.2).

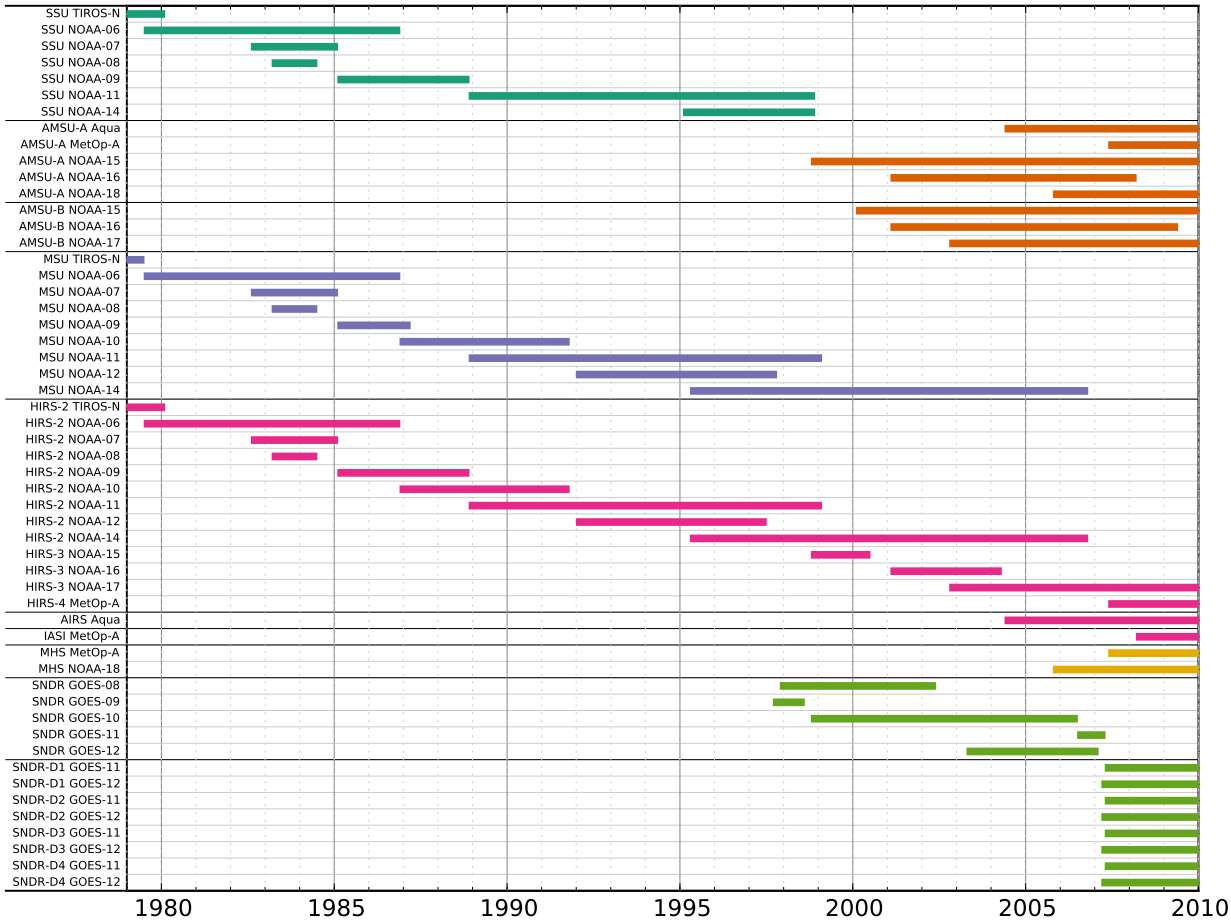

Figure 2.14: Availability of satellite instruments with radiances assimilated by CFSR as a function of time. Adapted from Saha et al. (2010). Original ©American Meteorological Society. Used with permission.

impacts of outlier observations on the final analysis state.

In addition to consistency checks, data may be thinned to reduce redundancy in regions where many observations are available. This procedure can have several benefits, including identifying previously undetected duplicates and reserving an independent set of observations for validating the analysis (Compo et al., 2011). Quality control criteria are also intimately connected to bias correction procedures. Bias corrections may be applied to certain observations either before or during the analysis step to keep otherwise good observations with known biases from being excluded from the analysis. Some typical bias correction procedures for radiosonde, satellite, and aircraft measurements are described in Section 2.4.3.

Table 2.22: Brief summary of standard quality control procedures applied in the reanalysis systems.

ERA-40	• Preliminary screening and exclusion of incomplete, duplicate, and blacklisted data • Thinning of selected observation types • Check that the departure from the first-guess is below a threshold that depends on expected error statistics • Variational quality control applied during the analysis step
ERA-Interim	• Preliminary screening and exclusion of incomplete, duplicate, and blacklisted data • Thinning of selected observation types • Check that the departure from the first-guess is below a threshold that depends on expected error statistics • Variational quality control applied during the analysis step
ERA-20C	• Preliminary screening and exclusion of incomplete, duplicate, and blacklisted data • In the case of duplicates, precedence is given to ICOADS over ISPD • Wind observations over land and near coasts are excluded • Data are excluded if more than three constant values are reported within a five-day window • Background check eliminates data with departures large (more than seven times expected) relative to the combined error variance • Variational quality control applied during the analysis step
ERA5	• Preliminary screening and exclusion of incomplete, duplicate, and blacklisted data • Thinning of selected observation types • Check that the departure from the first-guess is below a threshold that depends on expected error statistics • Variational quality control applied during the analysis step

JRA-25 / JCDAS	• Preliminary screening and exclusion of incomplete, duplicate, and blacklisted data • Gross check against climatology for most observation types, with thresholds determined using the "dynamic" method proposed by Onogi (1998) • Track checks for ships, buoys, and aircraft • Complex quality control for radiosondes • Data thinning is applied to AMVs and some TOVS radiances to make the data distribution more uniform
JRA-55	• Preliminary screening and exclusion of incomplete, duplicate, and blacklisted data • Gross check against climatology for most observation types, with thresholds determined using the "dynamic" method proposed by Onogi (1998) • Thresholds have been reviewed and updated relative to JRA-25 (Sakamoto and Christy, 2009) • Track checks for ships, buoys, and aircraft • Complex quality control for radiosondes • Variational bias correction is used for non-blacklisted satellite radiances
MERRA	• Preliminary screening and exclusion of incomplete, duplicate, and blacklisted data • Check that the departure from the first-guess background state is below a threshold that depends on observation type • Data thinning is applied to all radiance data
MERRA-2	• Preliminary screening and exclusion of incomplete, duplicate, and blacklisted data • Check that the departure from the first-guess background state is below a threshold that depends on observation type (thresholds revised relative to MERRA) • Data thinning is applied to all radiance data
NCEP-NCAR R1	• Complex quality control, including a hydrostatic check and correction • Data exclusion for unrealistic values, duplicate records, ship measurements over land, and blacklisted data • Thinning of selected observation types • Aircraft rejected during certain phases of flight • Background and buddy checks to eliminate observations with large departures • Quality control based on observations within ±24 hours rather than only the assimilation window • Horizontal and vertical thinning of satellite temperature retrievals to reduce the impact of resolution improvements over time

NCEP-DOE R2	• Complex quality control, including a hydrostatic check and correction • Data exclusion for unrealistic values, duplicate records, ship measurements over land, and blacklisted data • Thinning of selected observation types • Aircraft rejected during certain phases of flight • Background and buddy checks to eliminate observations with large departures • Quality control based on observations within ±24 hours rather than only the assimilation window • Horizontal and vertical thinning of satellite temperature retrievals to reduce the impact of resolution improvements over time
CFSR / CFSv2	• Complex quality control, including a hydrostatic check and correction • Data exclusion for unrealistic values, duplicate records, ship measurements over land, and blacklisted data • Thinning of selected observation types • Aircraft rejected during certain phases of flight • Variational quality control penalizes observations based on magnitude of departure from the preliminary analysis
NOAA-CIRES 20CR v2	• Pressure observations reduced to sea level and subjected to a gross check against the plausible range 880 to 1060 hPa • Background check eliminates data with departures large (more than three times expected) relative to the combined error variance • Buddy check against nearby observations; can override the results of the background check • Data thinning eliminates observations with weak impacts on the analysis; has the added effect of capping assimilated observations at near mid-20th century levels • Correction of systematic biases (recalibrated every 60 days)

2.4.3 Summary of key upper air observations and known issues

This section discusses a selection of upper air observational data that are assimilated in one or more of the reanalysis systems and are key for SPARC sciences. Radiosondes provide high vertical resolution profiles of temperature, horizontal wind, and humidity worldwide; however, most radiosonde stations are located in the Northern Hemisphere at middle and high latitudes over land (Figure 2.15). The typical vertical coverage of radiosonde data extends from the surface up to ~30 hPa for temperature and wind and from the surface up to 300~200 hPa for humidity. Operational satellite radiance measurements provide constraints for temperature and moisture with more homogeneous spatial coverage, but at the cost of deep vertical weighting functions (e.g., Figure 2.16). Moreover, the majority of these measurements were not available before 1978. Both observing systems have known biases, as well as jumps and drifts in the time series that may cause the quality

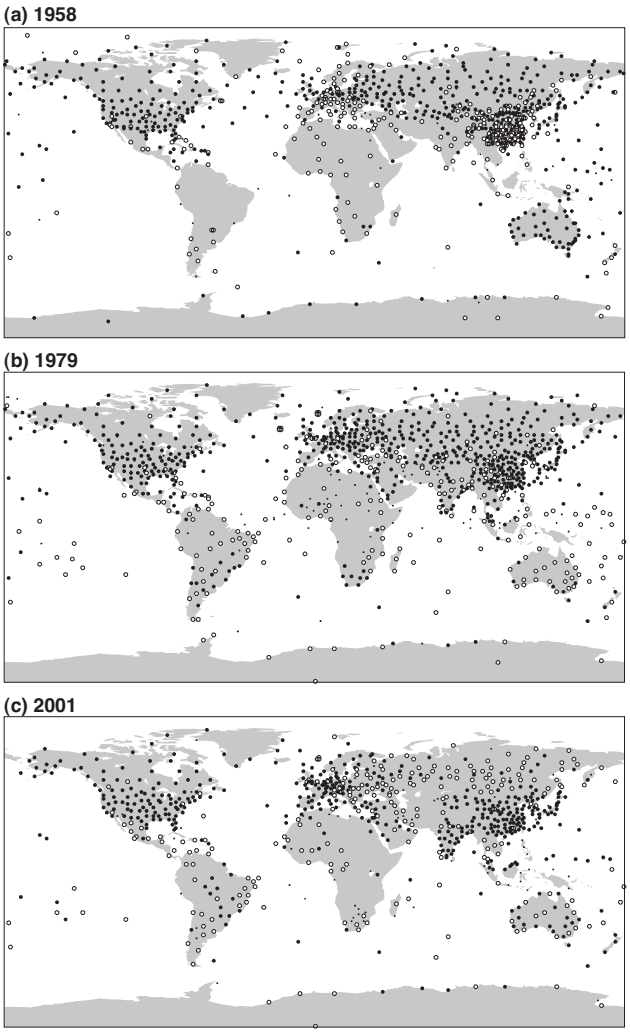

Figure 2.15: Frequency of radiosonde reports assimilated by ERA-40 during (a) 1958, (b) 1979, and (c) 2001. Solid circles denote stations reporting three times every 2 days on average, open circles denote stations reporting at least once every 2 days, and small dots denote stations reporting at least once per week (reproduced from Uppala et al., 2005). ©Royal Meteorological Society. Used with permission.

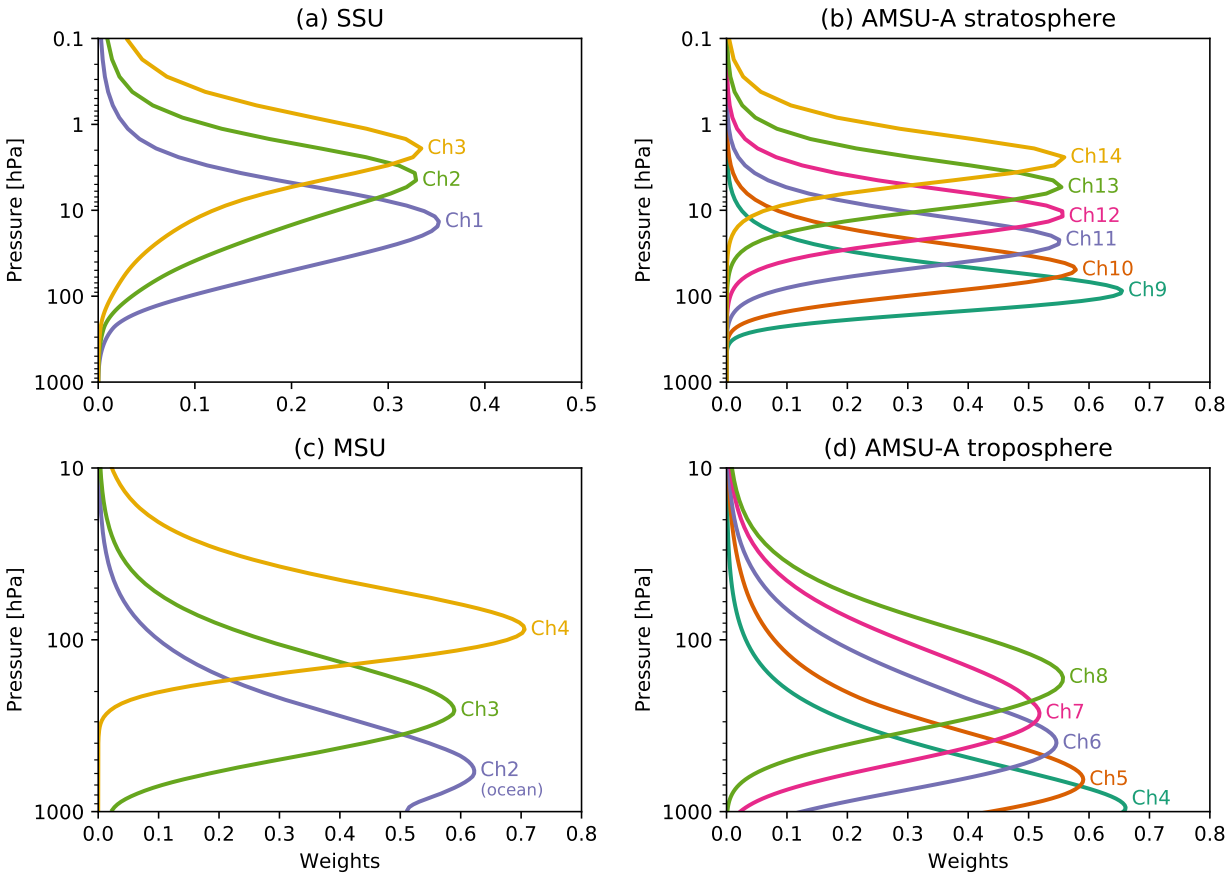

Figure 2.16: Example vertical weighting functions of radiance measurements for temperature based on (a) the SSU instrument (1979–2005) channels 1–3, (b) the AMSU-A instrument (1998–present) channels 9–14, (c) the MSU instrument (1979–2006) channels 2–4, and (d) AMSU-A channels 4–8. Weighting functions are for nadir or near-nadir scan positions and have been normalized as described by Zou and Qian (2016).

of reanalysis products to change over time. Bias corrections prior to and/or within the assimilation step are therefore essential for creating more reliable reanalysis products (see below for examples). In addition to radiosonde and satellite data, atmospheric motion vector (AMV) data created from geostationary and polar-orbiter satellite images and wind and temperature observations collected by aircraft are influential in the upper troposphere and lower stratosphere.

2.4.3.1 Radiosonde data

The main source of systematic errors in radiosonde temperature measurements is the effects of solar radiative heating and (to a lesser extent) infrared cooling on the temperature sensor (Nash et al., 2011). This issue, which is sometimes called the 'radiation error', can cause particularly pronounced warm biases in raw daytime stratospheric measurements. These biases may be corrected onsite in the ground data receiving system before reporting, and further corrections may be applied at each reanalysis centre before assimilation. The major issue with radiosonde humidity measurements is that the sensor response is too slow at cold temperatures (Nash et al., 2011). Recent advances in radiosonde instrumentation are beginning to improve this issue, particularly in the

upper troposphere; however, radiosonde observations of humidity at pressures less than 300 hPa are typically not assimilated by reanalysis systems. Other issues include frequent (and often undocumented) changes in radiosonde instrumentation and observing methods at radiosonde stations, which may cause jumps in the time series of temperature and relative humidity. Several 'homogenization' activities for radiosonde temperature data exist to support climate monitoring and trend analyses (see, e.g., Seidel et al., 2009). Although some of these activities have been effectively independent of reanalysis activities, cooperation between the two groups has increased substantially in recent years. Particularly notable is the production of RAOBCORE (Haimberger et al., 2008, 2012), which was conducted with reanalysis applications in mind. One or more versions of RAOBCORE are used in ERA-Interim (v1.3), MERRA and MERRA-2 (v1.4 through 2005), and JRA-55 (v1.4 through 2005; v1.5 thereafter). ERA5 uses the RICH dataset (v1.5.1) in place of RAOBCORE. Further efforts on data rescue, reprocessing, homogenization, and uncertainty evaluation by the broader research community are likely to be an essential part of the next generation of reanalyses (e.g., ACRE and GRUAN; Allan et al., 2011; Bodeker et al., 2016).

The following example describes a 'homogenization' (or bias correction) of radiosonde temperature measurements for assimilation in a reanalysis system:

(1) Radiosonde temperatures are corrected for estimated biases from 1980 onwards;
(2) Stations are separated into groups representing different countries or regions (because stations within the same country often use the same type of radiosonde from the same manufacturer);
(3) Mean differences between background forecasts and observations are accumulated for each group of stations;
(4) The mean error for all groups is subtracted from the bias computed for each group to provide a correction for radiation effects;

This approach corrects for many daily and seasonal variations of the biases but does not account for variations in annual mean biases. Radiosonde temperature measurements homogenized using this approach were assimilated in both ERA-40 and JRA-25 (Andræet al., 2004; Uppala et al., 2005; Onogi et al., 2007). The homogenizations applied to produce the RAOBCORE temperatures assimilated by many later reanalyses (including ERA-Interim, JRA-55, MERRA, and MERRA-2, as discussed above) have been conducted using updated versions of this procedure (Haimberger et al., 2008, 2012). Although radiosonde humidity measurements are also known to suffer from biases, current reanalysis systems do not include schemes to correct for biases in radiosonde humidities.

Major quality control criteria for radiosonde profiles (and other conventional data) include checks for completeness, physical and climatological consistency, and duplicate reports (Section 2.4.2). Data may also be filtered using locally compiled blacklists or blacklists acquired from other data providers and reanalysis centres. Further information on the quality control criteria applied by different reanalysis is available in the text and supporting material of the publications listed in Table 2.1.

Radiosonde and other upper-air in situ data are also often shared among different reanalysis centres. For example, Rienecker et al. (2011) listed the sources for historical radiosonde, dropsonde, and PIBAL data used by MERRA as:

(1) NCEP–NCAR: Office Note 20, Office Note 29, NMC/NCEP/GTS ingest;
(2) ECMWF: ECMWF/FGGE, ECMWF/MARS/GTS ingest;
(3) JMA: Japan Meteorological Agency GTS ingest;
(4) NCAR: International archives from Argentina, Australia, Brazil, Canada, China, Dominica, France, India, Japan, NCDC, New Zealand, Russia, Singapore, South Africa, United Kingdom

Research sets: PermShips, RemoteSites, Ptarmigan, Scherhaug, LIE, GATE, and BAS;

(5) NCDC: United States military and academic sources, including TD52, TD53, TD54, TD90, USCNTRL, USAF, United States Navy, CCARDS and MIT.

These data sources overlap substantially with those used in ERA-40 (Uppala et al., 2005, their Appendix B) and ERA-Interim (Tavolato and Isaksen, 2011), JRA-25 (Onogi et al., 2007, their section 2.1a) and JRA-55 (Kobayashi et al., 2015, their Table A1), MERRA-2 (McCarty et al., 2016), NCEP-NCAR R1 (Kalnay et al., 1996, their section 3a), and CFSR (Saha et al., 2010, their section "Conventional observing systems in the CFSR"); however, individual reanalyses may supplement standard data sets with data from unique sources. A detailed intercomparison of the conventional data used in each reanalysis is beyond the scope of this chapter; however, we note that at least four of the reanalyses (ERA-40, ERA-Interim, JRA-25, and JRA-55) use the ERA-40 ingest as a starting point, and that the ERA-40 ingest has much in common with the conventional data archives used by NCEP (R1, R2, and CFSR) and the NASA GMAO (MERRA and MERRA-2). More recent updates in data holdings at ECMWF, JMA, GMAO, and NCEP rely heavily on near-real-time data gathered from the WMO GTS, which also contributes to the use of a largely (but not completely) common set of conventional data among reanalysis systems.

2.4.3.2 Satellite data

Reanalysis systems assimilate data from several different types of satellite instruments, most notably the microwave and infrared sounders in the TOVS suite (1979–2006 on several satellites) and the ATOVS suite (1998–present on several satellites). The TOVS suite included the Stratospheric Sounding Unit (SSU), the Microwave Sounding Unit (MSU), and the High-resolution Infrared Sounder-2 (HIRS/2). The ATOVS suite includes the Advanced MSU-A (AMSU-A) and HIRS/3 (updated to HIRS/4 starting with NOAA-18). NCEP-NCAR R1 and NCEP-DOE R2 assimilate temperature retrievals from these instruments (see, e.g., Reale, 2001). All of the other full input reanalyses described in this chapter assimilate microwave and infrared radiances from the TOVS and ATOVS suites. ERA-Interim, ERA5, MERRA, MERRA-2, and CFSR also assimilate radiances from AIRS, the first hyperspectral infrared sounder with data assimilated in reanalyses (2002–present). ERA5, MERRA-2, and CFSR assimilate hyperspectral infrared radiances from IASI (2008–present), while ERA5 and MERRA-2 also assimilate radiances from the hyperspectral infrared sounder CrIS and the most recent generation of microwave sounder ATMS (late 2011–present). ERA-Interim, ERA5, JRA-55, MERRA-2, and CFSR assimilate data from GNSS-RO instruments, often starting with the CHAMP mission in May 2001 (Figure 2.17). GNSS-RO data are assimilated in the form of bending angles or refractivity at the tangent point rather than in the form of temperature or water vapour retrievals.

Satellite sounding instruments often have several channels with different vertical weighting functions (see, e.g., Figure 2.16). Even when using the same satellite instrument, different reanalysis systems may assimilate data from different sets of channels. Bias corrections and quality control criteria for satellite radiances may also vary by channel. Table 2.23 lists details of satellite data usage for four of the full input reanalysis systems considered in this chapter.

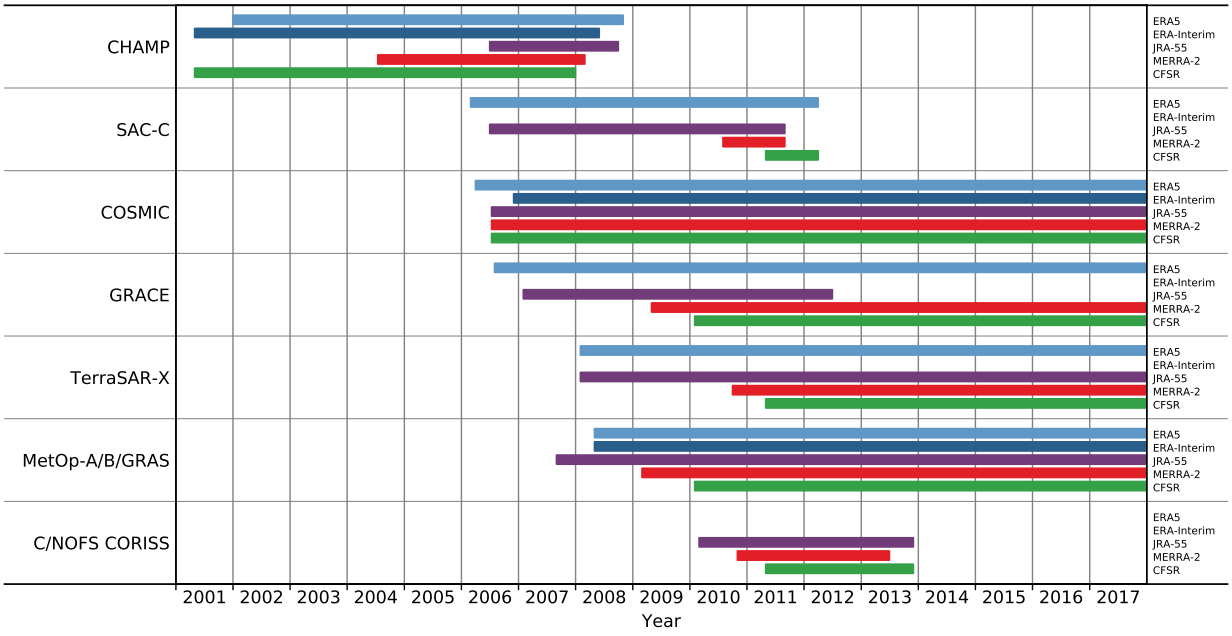

Figure 2.17: Assimilation of GNSS-RO observations by the ERA5 (light blue), ERA-Interim (dark blue), JRA-55 (purple), MERRA-2 (red), and CFSR (green) reanalysis systems as a function of time. See Appendix B for acronym definitions.

Table 2.23: Overview of satellite data usage in four of the most recent full input reanalysis systems. Adapted and updated from reanalyses.org. Refer to this website for source information and the latest version of this table (including information for JRA-25/JCDAS and MERRA). See Appendix B for acronym definitions.

Instrument (observable)	ERA-Interim	JRA-55	MERRA-2	CFSR/CFSv2
MSU (radiances)	Channels 2–4 **Exclusions:** • Ch. 2: land or rain • Ch. 3: land	Channels 2–4 **Exclusions:** • Ch. 2: land or rain • Ch. 3: land	Channels 2–4 **Notes:** NESDIS SNO corrected calibr. coefficients applied **Exclusions:** • Restrictive QC over snow, ice and mixed surfaces • Obs. errors inflated over non-water surfaces	Channels 1–4 **Notes:** NESDIS SNO corrected calibr. coefficients applied (NOAA-10 to -14) **Exclusions:** • More restrictive QC in tropics and over high terrain • Ch. 2: window test
AMSU-A (radiances)	Channels 5–14 **Notes:** No offset bias correction for ch. 14 **Exclusions:** • Ch. 5–6: high terrain • Ch. 5–7: rain	Channels 4–14 **Exclusions:** • Ch. 4–5: sea ice or land • Ch. 6–7: high terrain • Ch. 4–8: rain	Channels 4–14 **Exclusions:** • Restrictive QC • Ch. 4-6: observation errors inflated over non-water surfaces	Channels 1–13, 15 **Exclusions:** • Ch. 1-5, 15: estimated cloud liquid water large • Ch. 1-6, 15: scattering index large • Ch. 1-5, 15: ch. 4 gross check large • Ch. 1-5, 15: ch. 6 gross check large • Ch. 1-5, 15: high terrain • Ch. 1-5, 15: Fit to emissivity or surface temp large
AMSU-B/MHS (radiances)	Channels 3–5 **Exclusions:** • Ch. 3–4: sea ice, rain, high terrain • Ch. 5: land	Channels 3–5 **Exclusions:** • Land, sea ice, rain	Channels 1–5 **Exclusions:** • Restrictive gross check • Observation errors inflated for all channels over non-water surfaces	Channels 1–5 **Exclusions:** • Scattering index too large • Ch. 1 fit too large • Any channel failing gross check • High terrain
SSM/I (radiances)	Channels 1–7 **Exclusions:** • Land, rain	Channels 1,3,4,6 **Exclusions:** • Land, rain	Channels 1–7 **Exclusions:** • All non-water surfaces	

HIRS (radiances)	Channels 2–7,11,12, 14,15 **Exclusions:** • Ch. 4–7,11,14,15: clouds, land • Ch. 12: high terrain	Channels 2–7,11,12, 14,15 **Exclusions:** • Ch. 4–7,11,14,15: land • Ch. 12: high terrain • Ch. 3 and above: cloud	Channels 2–12 **Exclusions:** • Surface-sensitive channels • Observation errors inflated over non-water surfaces	Channels 2–15 **Exclusions:** • Wavenumbers > 2400 over water during day • High terrain • Above model top • Channels without signal over clouds • Surface sensing channels with large difference
SSU (radiances)	Channels 1–3 **Notes:** No offset bias correction for ch. 3	Channels 1–3	Channels 1–3 **Notes:** • Only ch. 1–2 after NOAA-15 AMSU-A available (1 Nov 1998) • No offset bias correction for ch. 3	Channels 1–3 **Notes:** All channels bias-corrected.
GEO (radiances)	GOES, MTSAT, METEOSAT imagers	GOES, GMS, MTSAT, METEOSAT imagers	GOES; METEOSAT after early 2012	GOES sounder **Notes:** • 5°×5° 1993–2007 • 1°×1° 2007–present
SSM/I (retrievals)	Total column water vapor (rainy areas over oceans)	Snow cover	Surface wind speed over ocean; rain rate	Surface wind speed over ocean
Imager (upper-air winds)	GOES, GMS, MTSAT, METEOSAT, MODIS	GOES, GMS, MTSAT, METEOSAT, MODIS	GOES, GMS, MTSAT, METEOSAT, MODIS	GOES, GMS, MTSAT, METEOSAT, MODIS
Scatterometer (winds over ocean surface)	ERS, QuikSCAT	ERS, QuikSCAT, ASCAT	ERS, QuikSCAT, ASCAT	ERS, QuikSCAT, ASCAT
Ozone sensors (retrievals)	TOMS, SBUV, GOME, MIPAS, SCIAMACHY, MLS, OMI	TOMS, OMI (nudging)	SBUV V8 retrievals, OMI, MLS (v2.2 through 31 May 2015, switching to v4.2 from 1 June 2015; 261 hPa switched off from 1 May 2016)	SBUV V8 retrievals

Other notable elements	• GNSS-RO • AIRS • SSM/I-S • AMSR-E • HIRS NOAA-18	• Reprocessed winds from GMS, GOES-9, MTSAT (revised) and METEOSAT • Reprocessed radiances from GMS, GOES-9, MTSAT • TMI (NASA) • AMSR-E (JAXA) • GNSS-RO • SSM/I-S • VTPR • Exclude HIRS from NOAA-15 and later	• TMI rain rate • AIRS • IASI • CrIS • GNSS-RO • NOAA-15 AMSU-B • ATMS • SEVIRI • MLS retrievals of temperature above 5 hPa (v3.3 through 31 May 2015, switching to v4.2 from 1 June 2015) • AOD from MISR, MODIS, AVHRR and AERONET	• AIRS • IASI • GNSS-RO • AMSR-E • Reprocessed ERS • Reprocessed GMS • AMSU-B (NOAA-15 only)

Radiances observed by the SSU instruments, which covered the period 1979–2005, represent an important archive of stratospheric temperatures (e.g., Wang et al., 2012; Zou et al., 2014; Nash and Saunders, 2015) and serve as a useful illustration of the types of issues that may be encountered in assimilating satellite data. The SSU was a pressure-modulated radiometer with an onboard CO_2 cell for spectral filtering at 15 μm. The calibration of SSU radiances is affected by the following known issues:
(1) Space-view anomalies due to electrical interference;
(2) CO_2 gas leakage and cell pressure changes;
(3) Changes in atmospheric CO_2 concentrations;
(4) Satellite orbital drift and diurnal sampling biases;
(5) Short overlap periods between successive instruments.
Raw radiance data from SSU include drifts and jumps in the time series due to these issues (e.g., Figure 2.18), which must be accounted for in the data assimilation system. Drifts and jumps of this type are not unique to SSU, and other long-term satellite radiance archives are also affected by issues specific to individual instruments. For example, Simmons et al. (2014, their Figure 13) have shown that estimated biases for certain MSU, HIRS, and AMSU-A channels can be of similar orders of magnitude to those for SSU, while trends in atmospheric CO2 concentrations also cause long-term drifts in estimated biases for HIRS, AIRS, and IASI radiances. Biases in radiances observed by MSU and AMSU-A can be attributed mainly to inaccurate calibration offsets and non-linearity (Zou et al., 2006).

Post-launch inter-satellite calibration (or "homogenization") efforts by the satellite remote sensing community, such as the WMO GSICS (Goldberg et al., 2011) have substantially reduced inter-satellite differences in some cases, including MSU (Zou et al., 2006), AMSU-A (Zou and Wang, 2011), and SSU (Zou et al., 2014). In practice, this type of inter-satellite calibration is usually performed by reanalysis systems internally via bias correction terms applied during the data assimilation step. It is therefore not strictly necessary for satellite data to be homogenized prior

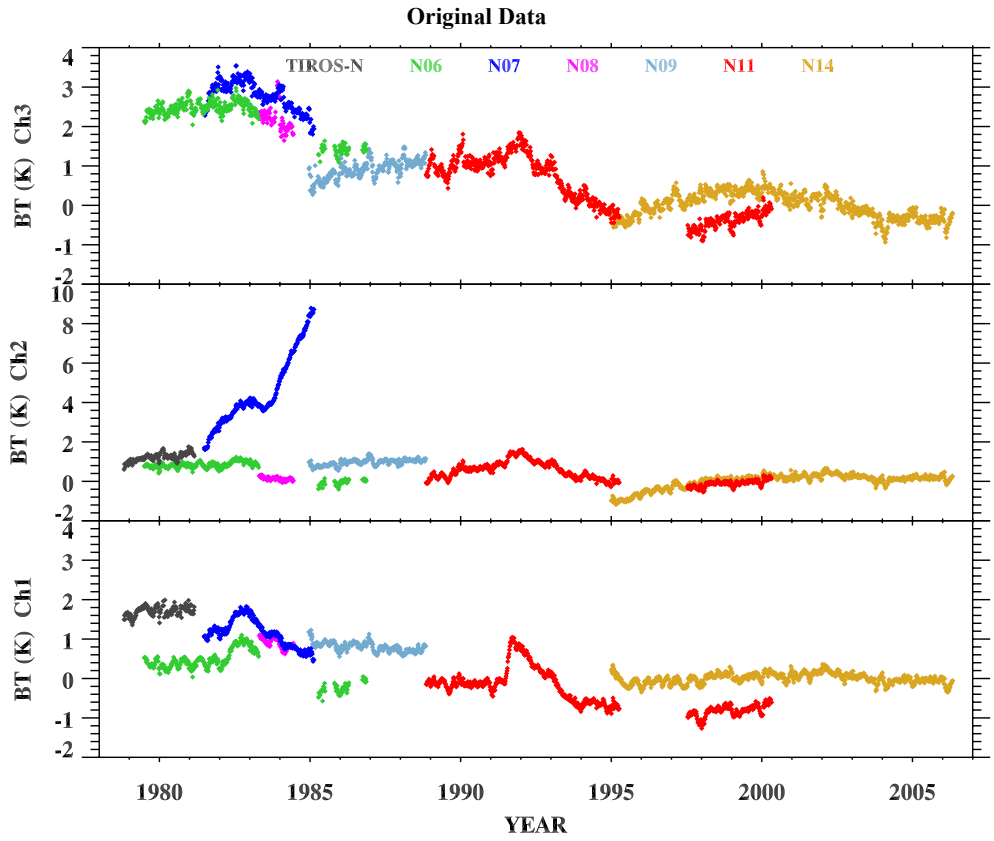

Figure 2.18: Global mean pentad brightness temperature anomalies based on raw SSU radiances from different satellites. Anomalies are calculated relative to the 1995–2005 mean NOAA-14 annual cycle (reproduced from Wang et al., 2012). ©American Meteorological Society. Used with permission.

to its assimilation in a reanalysis system, although it is beneficial to assimilate data with biases as small as possible.

The use of externally homogenized data has been found to improve some aspects of recent reanalyses. For example, homogenized MSU data (Zou et al., 2006) assimilated by CFSR, MERRA and MERRA-2 (Table 2.23) have been found to improve temporal consistency in bias correction patterns (Rienecker et al., 2011), and may have helped MERRA to produce a more realistic stratospheric temperature response following the eruption of Mount Pinatubo (Simmons et al., 2014). In situations where conventional data are unavailable or insufficient to provide a reference for satellite bias correction, such as SSU in the middle and upper stratosphere, homogenized radiance data may be even more effective in eliminating artificial drifts and jumps in the analysis state. Homogenized satellite radiance time series only represent a relatively small fraction of the satellite data ingested by current reanalysis systems (several of which do not assimilate homogenized data at all); however, the availability of homogenized satellite radiance time series is increasing and these data are likely to become more influential in future reanalysis efforts.

Bias corrections for assimilated satellite data often vary by satellite platform and/or reanalysis system. Although bias corrections are intended to limit the impacts of changing satellite biases within the reanalysis, these impacts may still manifest as spurious trends or discontinuities in the time series of temperature and other reanalysis variables. In older reanalyses that assimilated satellite radiances, such as ERA-40 and JRA-25, bias corrections were often (but not always) based on a fixed regression that spanned the lifetime of the instrument (Uppala et al., 2005; Onogi et al., 2007; Sakamoto and Christy, 2009). This approach, which occasionally required the reanalysis to be interrupted for manual retuning of bias correction terms, has been replaced by adaptive (or variational) bias correction schemes in recent reanalysis systems. Adaptive bias corrections for satellite radiances are based on differences between observed radiances and expected radiances calculated from model-generated background states. Some early implementations of adaptive bias corrections, such as that applied to TOVS data in JRA-25, left the reanalysis vulnerable to jumps and drifts inherited from the assimilated radiances (Sakamoto and Christy, 2009). These problems are addressed in most recent reanalysis systems by defining observational 'anchors' that are regarded as unbiased and are therefore allowed to contribute directly to the background state (Dee, 2005). A key example is the use of homogenized radiosonde data to anchor bias corrections for satellite radiances (e.g., Auligné et al., 2007). Versions of this approach have been implemented in ERA-Interim, ERA5, JRA-55, MERRA, and MERRA-2. GNSS-RO observations are also useful for anchoring bias corrections (e.g., Poli et al., 2010), and are used in this capacity in ERA-Interim, ERA5, JRA-55, and MERRA-2. However, GNSS-RO data are only available after May 2001, and only reached wide coverage with the beginning of the COSMIC mission in 2006 (Figure 2.17). The approach to bias correction taken by CFSR and CFSv2 (Derber and Wu, 1998; Saha et al., 2010) differs from that taken by other systems in that anchor observations are not used. Instead, initial bias corrections are determined for each new satellite instrument via a three-month spin-up assimilation and then allowed to evolve slowly. The effects of satellite-specific drifts and jumps are kept small by assigning very low weights to the most recent biases between the observed and expected radiances, and by accounting for known historical variations in satellite performance as catalogued by multiple research centres. One byproduct of this procedure is an oscillating warm bias in CFSR in the upper stratosphere (see Chapter 3 of the S-RIP report). This bias, which is intrinsic to the forecast model, largely disappears when a new execution stream is introduced, only to slowly return as the model bias is imprinted on the observational bias correction terms.

A further example of the type of temporal discontinuities that can result from changes in satellite instrumentation is the cold bias (~2 K) in middle stratospheric temperature in JRA-25 between 1979 and 1998 (Onogi et al., 2007). This feature resulted from a known cold bias in the radiative transfer model used by JRA-25. The SSU had only three channels sensitive to stratospheric temperature (too few to correct the model bias). The AMSU-A instruments, first launched in 1998, have more channels (i.e., higher vertical resolution) in the stratosphere (see also Figure 2.16). Assimilation of the higher-resolution AMSU-A radiances effectively corrected the model bia in temperatures, but at the cost of enhanced spurious diabatic cooling in the stratosphere during the forecast step (Wright and Fueglistaler, 2013). The JRA-55 system uses an improved radiative transfer model, and produces more realistic stratospheric temperatures during 1979–1998 (Ebita et al., 2011; Kobayashi et al., 2015).

A final illustrative example concerns temperatures in the upper stratosphere. MERRA shows artificial annual cycles in the upper stratosphere (Rienecker et al., 2011, their Figure 16), which probably arise because the forward radiative transfer model used to assimilate SSU radiances did not consider variations in atmospheric CO_2. These issues have been corrected in MERRA-2, which uses version 2.1.3 of the CRTM to assimilate SSU radiances (Table 2.19). Several reanalyses also show jumps in upper stratospheric temperature in or around 1998 (the sign varies by vertical level and reanalysis) due to the introduction of AMSU-A, which includes channels that peak higher in the stratosphere. See Chapter 3 of the S-RIP report for further details and additional examples.

2.4.3.3 Aircraft data

Measurements made by aircraft, such as the AMDAR data collection, are influential inputs in many atmospheric analyses and reanalyses (Petersen, 2016). Horizontal wind data from aircraft are assimilated in all of the reanalysis systems but ERA-20C and 20CR, while temperature data from aircraft are assimilated in all of the reanalysis systems except for ERA-20C, JRA-55, JRA-25, and 20CR. In principle, aircraft data were assimilated from the outset by ERA-40 (September 1957; Uppala et al., 2005), JRA-55 (January 1958; Kobayashi et al., 2015), and NCEP-NCAR R1 (January 1948; Kalnay et al., 1996; see also Moninger et al., 2003), although many of the data from these early years do not meet the necessary quality control standards for assimilation (Section 2.4.2). The volume of aircraft data suitable for assimilation increased substantially after January 1973 (Uppala et al., 2005; Kobayashi et al., 2015).

Aircraft temperature data have been reported to have a warm bias with respect to radiosonde observations (Ballish and Kumar, 2008). This type of discrepancy among ingested data sources can have important impacts on the analysis. For example, Rienecker et al. (2011) and Simmons et al. (2014) have shown that an increase in the magnitude of the temperature bias at 300 hPa in MERRA with respect to radiosondes in the middle to late 1990s coincides with a large increase in the number of aircraft observations assimilated by the system. Moreover, they conclude that differences in temperature trends at 200 hPa between MERRA and ERA-Interim reflect the different impacts of aircraft temperatures in these two reanalysis systems. MERRA-2 applies adaptive bias corrections to AMDAR observations that may help to reduce the uncertainties associated with assimilating these data (McCarty et al., 2016): after each analysis step the updated bias is estimated as a weighted running mean of the aircraft observation increments from preceding analysis times. These adaptive bias corrections are calculated and applied for each aircraft tail number in the database separately.

2.4.4 Water vapour

The assimilation of radiosonde and satellite observations of humidity fields is problematic in the upper troposphere and above, where water vapour mixing ratios are very low and measurement uncertainties are relatively large. The impact of saturation means that humidity probability density functions are often highly non-Gaussian (Ingleby et al., 2013). These issues are particularly pronounced near the tropopause, where sharp temperature gradients complicate the calculation and application of bias corrections for humidity variables during the assimilation step. Reanalysis systems therefore often do not assimilate observations of water vapour provided by radiosondes and/or microwave and infrared sounders (mostly in the form of radiances; see Section 2.4.3.2) above a specified upper bound, typically between ~300 hPa and ~100 hPa. In regions of the atmosphere that lie above this upper bound (i.e., the uppermost troposphere and stratosphere), the water vapour field is typically determined by the forecast model alone. In this case, water vapour in the stratosphere is determined mainly by transport from below, turbulent mixing, and dehydration in the vicinity of the tropical cold point tropopause (e.g., Gettelman et al., 2010). Table 2.24 provides brief descriptions of special treatments and caveats affecting reanalysis estimates of water vapour in the upper troposphere and stratosphere. A more detailed discussion and assessment of reanalysis estimates of water vapour is provided in Chapter 4 of the S-RIP report.

Table 2.24: Notes on treatment of water vapour in the upper troposphere and stratosphere.

ERA-40	No adjustments due to data assimilation are applied in the stratosphere (above the diagnosed tropopause). Methane oxidation is included via a simple parameterization in the stratosphere.
ERA-Interim	The ERA-Interim system contains a parameterization that allows supersaturation with respect to ice in the cloud-free portions of grid cells with temperatures less than 250 K. The inclusion of this parameterization results in a substantial increase of RH in the upper troposphere and stratospheric polar cap when compared with ERA-40 (Dee et al., 2011). No adjustments due to data assimilation are applied in the stratosphere (above the diagnosed tropopause). Methane oxidation is included via a simple parameterization in the stratosphere.
ERA-20C	ERA-20C does not assimilate any water vapour observations. Supersaturation with respect to ice is permitted in cloud-free portions of grid cells with temperatures less than 250 K, and methane oxidation is included via a simple parameterization in the stratosphere.
ERA5	Like ERA-Interim, the ERA5 system contains a parameterization that allows supersaturation with respect to ice in cloud-free portions of grid cells, but for all temperatures below 273 K (rather than 250 K for ERA-Interim). A more consistent treatment of potentially negative values in the stratosphere has been added. Methane oxidation is included via a simple parameterization in the stratosphere.

JRA-25 / JCDAS	Observations of humidity are not assimilated and analyses of moisture variables are not provided at pressures less than 100 hPa. Vertical correlations of humidity background errors are set to zero at pressures less than 50 hPa to prevent spurious analysis increments above this level. No moisture source due to methane oxidation is applied to water vapour in the stratosphere. The radiation scheme assumes a constant volume mixing ratio of 2.5 ppm in the stratosphere.
JRA-55	Analyses of moisture variables are not provided at pressures less than 100 hPa in the pressure-level analysis (anl_p), although analyses of moisture variables are provided for all model levels in the model-level analysis (anl_mdl). Observations of humidity are not assimilated at pressures less than 100 hPa, and vertical correlations of humidity background errors are set to zero at pressures less than 5 hPa to prevent spurious analysis increments above this level. No moisture source due to methane oxidation is applied to water vapour in the stratosphere. The radiation scheme uses climatological annual mean mixing ratios observed by HALOE and UARS MLS during 1991–1997 (without seasonal variations) in the stratosphere.
MERRA	The MERRA system tightly constrains stratospheric water vapour to a specified profile, which is based on zonal mean climatologies from HALOE and Aura MLS (Jiang et al., 2010; Rienecker et al., 2011). Water vapour does not undergo physically meaningful variations at pressures less than ~50 hPa.
MERRA-2	Like MERRA, MERRA-2 tightly constrains stratospheric water vapour to a specified profile, which is based on zonal mean climatologies from HALOE and Aura MLS (Jiang et al., 2010; Rienecker et al., 2011). Water vapour does not undergo physically meaningful variations at pressures less than ~50 hPa.
NCEP-NCAR R1	Analyses of moisture variables are not provided at pressures less than 300 hPa. Satellite humidity retrievals are not assimilated.
NCEP-DOE R2	Satellite humidity retrievals are not assimilated.
CFSR / CFSv2	Although there is no upper limit to assimilated GNSS-RO data, radiosonde humidities are only assimilated at pressures 250 hPa and greater. Moisture variables are provided in the stratosphere, but dehydration processes in the tropopause layer may yield negative values. Negative values are artificially replaced by very small positive values for the radiation calculations, but are not replaced in the analysis. CFSR does not include a parameterization of methane oxidation.

NOAA-CIRES 20CR v2	Moisture variables are provided in the stratosphere, but dehydration processes in the tropopause layer may yield negative values. Negative values are artificially replaced by very small positive values for the radiation calculations, but are not replaced in the analysis. 20CR does not include a parameterization of methane oxidation.

2.5 Execution streams

2.5.1 What is an 'execution stream'?

The production of reanalyses often must be completed under strict deadlines determined by external factors. To meet these deadlines, most reanalyses have been executed in two or more distinct 'streams', which are then combined. Discontinuities in the time series of some analyzed variables may occur when streams are joined. These potential discontinuities should be considered (along with the changes in assimilated observations described in Section 2.4) when reanalysis variables are used for assessments of climate variability and/or trends.

2.5.2 Summary of stream execution

Table 2.25 and Figure 2.19 briefly summarize the streams used for generating each set of reanalysis products. Refer to the reference papers listed in Table 2.1 for the procedures used to transition between streams in creating the final data product, as different reanalysis systems may use different approaches. Certain periods have been reprocessed to correct errors in the input data. The reprocessed periods and associated potential discontinuities listed in Table 2.25 and shown in Figure 2.19 may be incomplete, and are also likely to change subsequent to the publication of this report. Users are therefore recommended to contact the reanalysis centres directly if they encounter unexplained shifts or jumps in reanalysis products.

Table 2.25: Information on the execution streams for each reanalysis system.

ERA-40	ERA-40 was planned for execution in three streams covering 1989–2002, 1957–1972, and 1972–1988. In practice, a small number of parallel-running sub-streams bridging gaps between the main streams had to be run in order to meet the production deadline.
ERA-Interim	ERA-Interim was carried out in two main streams, the first from 1989 to present and the second from 1979 to 1988. The period of the first stream covering January 1989 to August 1993 was rerun to include from the outset all changes made on the fly in the original production for this period; these changes were also included in the second main production stream. The second stream was extended to the end of 1989 to check consistency during the overlap period (see also discussion by Simmons et al., 2014).
ERA-20C	The reanalysis consists of 22 streams, all but the last of which are six years in length. The first stream starts on 1 January 1899 and extends through 31 December 1904. Each subsequent stream starts on 1 January in years ending in 4 or 9 and ends on 31 December of the next year ending in 4 or 9. The final stream starts on 1 January 2004 and extends seven years through the end of the reanalysis. The first year of each stream is used for spin-up and is discarded from the final product.

ERA5	ERA5 consists of one high-resolution (31-km) analysis (termed HRES) and a 10-member reduced-resolution (62-km) ensemble of data assimilations (EDA). Production is planned to proceed in parallel streams, one per decade (1950–1959, 1960–1969, etc.), with one year of spin-up for each stream. As of this writing, the public release consists of two streams covering 2000–2009 and 2010–present. Actual production may differ from this planned approach.
JRA-25 / JCDAS	JRA-25 was conducted in two main streams: the first covers January 1979–December 1990, and the second covers January 1991–January 2014. Note also the transition from JRA-25 (conducted jointly by JMA and CRIEPI) to JCDAS (conducted by JMA only) in January 2005. The execution of JCDAS was conducted entirely in real time. Two periods (January 1994–December 1999 and January 2000–January 2002) were recalculated and replaced to fix problems with data quality; these two periods may be considered as separate sub-streams in addition to the two main streams.
JRA-55	JRA-55 has been executed in two streams. Stream A covers January 1958 through August 1980, while stream B covers September 1980 through the present. Three periods have also been reprocessed after errors were identified: January to June 1958, December 1974 to August 1980 and June 1987 to September 1992 (see also Kobayashi et al., 2015, their Figure 7). JRA-55C has been executed in three streams: Stream A covers 1 November 1972 through 31 August 1980, Stream B covers 1 September 1980 through 31 August 2005, and Stream C covers 1 September 2005 through 31 December 2012. JRA-55AMIP has been executed in one continuous stream.
MERRA	MERRA was executed in three streams. Stream 1 covers January 1979–December 1992, stream 2 covers January 1993–December 2000, and stream 3 covers January 2001–February 2016. Each stream was spun up in two stages: a 2-year analysis at 2°×2.5° followed by a 1-year analysis on the native MERRA grid (see Table 2.2). The production version of stream 2 (after spin-up) overlaps with the final four years of stream 1 (January 1989–December 1992), while the production version of stream 3 overlaps with the final three years of stream 2 (January 1998–December 2000).
MERRA-2	MERRA-2 was executed in four streams covering January 1980–December 1990, January 1991–December 2000, January 2001–December 2010, and January 2011–present. Each stream was spun up for one year on the full MERRA-2 system.

NCEP-NCAR R1	R1 was run in three streams. The first stream, which produced data covering 1982–present, started in December 1978. The second stream covers 1958–1981 (post-IGY). The third and final stream covers 1948–1957 (pre-IGY), with analyses conducted at 03UTC, 09UTC, 15UTC and 21UTC (rather than 00UTC, 06UTC, 12UTC and 18UTC). There may be additional discontinuities involving updates. For example, if the original analyses were affected by a problem with the sea ice boundary condition, a second simulation may have been run to replace the analyses during the problematic period. Transitions between the original product and these "patches" may cause discontinuities.
NCEP-DOE R2	R2 was executed in one continuous stream; however, like R1, there may be discontinuities involving updates.
CFSR / CFSv2	CFSR was produced by running six simultaneous streams covering the following periods: Stream 1: 1 December 1978 to 31 December 1986 Stream 2: 1 November 1985 to 31 December 1989 Stream 5: 1 January 1989 to 31 December 1994 Stream 6: 1 January 1994 to 31 March 1999 Stream 3: 1 April 1998 to 31 March 2005 Stream 4: 1 April 2004 to 31 December 2009 A full 1-year overlap between the streams was used to spin-up the deep ocean, the upper stratosphere, and the deep soil. The entire CFSR thus covers 31 years (1979–2009) plus five overlap years. Each earlier stream is used to its end, so that the switch to the next stream occurs at the end of the overlap period. A separate one-year stream was run for 2010, after which the analysis system was updated to CFSv2 (with an increase in horizontal resolution from T382 to T574). CFSv2 is intended as an extension of CFSR, but users should be cautious when conducting analyses that span the transitional period from the end of 2009 to the beginning of 2011.

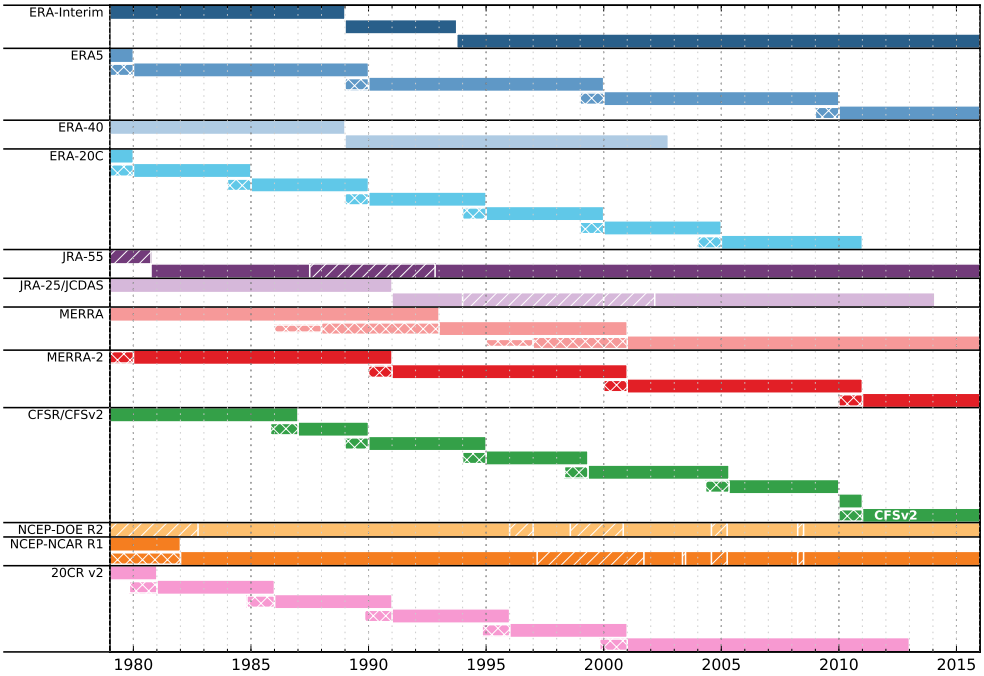

Figure 2.19: Summary of the execution streams of the reanalyses for the period 1979–2016, including the planned execution of ERA5 (which is not completed as of this writing). Hatching indicates known re-processed 'patches'. The narrowest cross-hatched segments indicate documented spin-up periods, while the medium-narrow cross-hatched segments indicate overlap periods. See also Table 2.25.

NOAA-CIRES 20CR v2

20CR v2 was executed in 28 streams. With some exceptions, each stream typically produced five years of data with 14 months of spin-up. The following text gives the data coverage provided by each stream (the streams are numbered sequentially), with the spin-up start year provided in parentheses: 1871–1875 (1869), 1876–1880 (1874), 1881–1885 (1879), 1886–1890 (1884), 1891–1895 (1889), 1896–1900 (1894), 1901–1905 (1899), 1906–1910 (1904), 1911–1915 (1909), 1916–1920 (1914), 1921–1925 (1919), 1926–1930 (1924), 1931–1935 (1929), 1936–1940 (1934), 1941–1945 (1939), 1946–1951 (1944), 1952–1955 (1949), 1956–1960 (1954), 1961–1965 (1959), 1966–1970 (1964), 1971–1975 (1969), 1976–1980 (1974), 1981–1985 (1979), 1986–1990 (1984), 1991–1995 (1989), 1996–2000 (1994), and 2001–2012 (1999). The spin-up start date for each stream was 00UTC 1 November, the production start date was 00UTC 1 January, and the production end date was 21UTC 31 December.

2.6 Archived data

The original data at model resolution and model levels (Table 2.2) are converted by each reanalysis centre to data on regular horizontal grids (sometimes at multiple resolutions) and on pressure levels (see Appendix A) for public release. The converted data (and sometimes the original data) can often be obtained via the reanalysis centre websites (see the list of links provided on the S-RIP website). Some other institutes or projects, such as the NCAR RDA, have also constructed public archives of one or more of the reanalysis datasets. Such institutes may have used independent conversions for the data grid, levels, and/or units. Pre-processed data sets have also been produced for the S-RIP activity, including zonal-mean data sets containing dynamical (Martineau, 2017) and diabatic (Wright, 2017) diagnostics on pressure levels, which are stored together with detailed documentation in the S-RIP archive at CEDA (http://data.ceda.ac.uk/badc/srip/; see also Martineau et al., 2018). Additional data produced for S-RIP include supplementary data files for this chapter (or access an earlier version provided as a supplement to Fujiwara et al., 2017), common grid files containing core variables, and CFSR/CFSv2 products on model levels. The latter two data sets are curated by Sean Davis and hosted at NOAA; steps for access are described on the S-RIP website. Data users of these or any other public release of reanalysis or reanalysis-based products should always read the documentation for that release carefully.

It is particularly important to check unit information, as different reanalysis centres or public archives may use different units for the same variable. For example, temperature is usually provided in units of K but is occasionally provided in °C. Some centres provide geopotential height in meters (or 'gpm'), while others provide geopotential in $m^2\,s^{-2}$. For water vapour, specific humidity (not mass or volume mixing ratio) is provided in most cases, in units of either $kg\,kg^{-1}$ or $g\,kg^{-1}$. Some reanalyses do not provide vertical pressure velocity (ω, in $Pa\,s^{-1}$) and/or specific humidity data in the stratosphere. Ozone is provided as mass mixing ratio (not volume mixing ratio) in most cases, in units of either $kg\,kg^{-1}$ or $mg\,kg^{-1}$ (i.e., ppmm). Care is also recommended when using precipitation or other 'flux' data, for which the integration time period may not be explicitly documented in the data file. Precipitation data may also be divided into multiple categories (such as anvil, convective, and large-scale), the exact definitions of which vary by reanalysis.

The file formats for archived data include GRIB, GRIB2, NetCDF, and HDF. Grid boundaries and orientations, such as the starting point for longitude (0°E or 180°W), the order of latitudes (from the North Pole or from the South Pole), and the vertical orientation (from the surface or from the TOA) may also vary by reanalysis and/or data source.

Most reanalyses (with the exceptions of MERRA and MERRA-2) provide data below the surface (e.g., at 1000 hPa over the continents). These data are calculated via vertical extrapolation, and are provided for two reasons. First, they enable the use of a complete field when plotting or taking derivatives on pressure surfaces. Second, they allow data users to visualize variability over the whole globe (including features over mountains) using data from a single pressure surface. The extrapolation procedure may differ by variable and/or reanalysis system. Users of data in the lower part of the troposphere should be aware of this feature and take steps to account for it, particularly in regions of complex topography.

Acknowledgements

The materials contained in the tables and figures have been compiled from a variety of sources, for which we acknowledge the contributions of Santha Akella, Peter Bechtold, Christine Bloecker,

Michael Bosilovich, Dick Dee, John Derber, Ron Gelaro, Yun-Tai Hou, Robert Kistler, Daryl Kleist, Shinya Kobayashi, Shrinivas Moorthi, Eric Nielsen, Yvan Orsolini, Saroja Polavarapu, Paul Poli, Bill Putman, Suranjana Saha, Jack Woollen, Fanglin Yang, and Valery Yudin. We thank Wenhao Dong, Suqin Duan, and Jacob Smith for providing comments on advance drafts of this document, an anonymous reviewer for detailed and insightful comments on the first submitted draft, and Xiaolin Jin for assistance with typesetting.

A Vertical Levels

ERA-40 and ERA-Interim

ERA-40 and ERA-Interim both use a hybrid sigma–pressure (hybrid σ-p) vertical coordinate (Simmons and Burridge, 1981), which are also sometimes referred to as an eta (η) vertical coordinate (see also http://rda.ucar.edu/datasets/ds627.0/docs/Eta_coordinate). Both systems use the same vertical resolution with 60 levels. The pressure on each level is calculated as $p_k = A_k + B_k \times p_{\mathrm{srf}}$, where p_{srf} is surface pressure. Table A1 provides example pressures at layer interfaces ($k - {}^1/_2$) and layer midpoints (k) for a surface pressure of 1013.25 hPa, from TOA to surface. Pressures at layer midpoints are defined as the average of pressures at layer interfaces. Pressure levels in brackets are used for ERA-Interim products but not for ERA-40 products.

Table A1: List of vertical levels used by ERA-40 and ERA-Interim.

	Model levels				Pressure levels
k	$A_{k-1/2}$ (hPa)	$B_{k-1/2}$	$p_{k-1/2}$ (hPa)	p_k (hPa)	p (hPa)
1	0.00	0.00000	0.00	0.10	
2	0.20	0.00000	0.20	0.29	
3	0.38	0.00000	0.38	0.51	
4	0.64	0.00000	0.64	0.80	
5	0.96	0.00000	0.96	1.15	1
6	1.34	0.00000	1.34	1.58	
7	1.81	0.00000	1.81	2.08	2
8	2.35	0.00000	2.35	2.67	3
9	2.98	0.00000	2.98	3.36	
10	3.74	0.00000	3.74	4.19	
11	4.65	0.00000	4.65	5.20	5
12	5.76	0.00000	5.76	6.44	7
13	7.13	0.00000	7.13	7.96	
14	8.84	0.00000	8.84	9.89	10
15	10.95	0.00000	10.95	12.26	
16	13.56	0.00000	13.56	15.19	
17	16.81	0.00000	16.81	18.81	20
18	20.82	0.00000	20.82	23.31	
19	25.80	0.00000	25.80	28.88	30
20	31.96	0.00000	31.96	35.78	
21	39.60	0.00000	39.60	44.33	
22	49.07	0.00000	49.07	54.62	50
23	60.18	0.00000	60.18	66.62	70
24	73.07	0.00000	73.07	80.40	
25	87.65	0.00008	87.73	95.98	100
26	103.76	0.00046	104.23	113.42	
27	120.77	0.00182	122.61	132.76	(125)
28	137.75	0.00508	142.90	154.00	150
29	153.80	0.01114	165.09	177.12	(175)
30	168.19	0.02068	189.15	202.09	200
31	180.45	0.03412	215.03	228.84	(225)

32	190.28	0.05169	242.65	257.36	250
33	197.55	0.07353	272.06	287.64	300
34	202.22	0.09967	303.22	319.63	
35	204.30	0.13002	336.04	353.23	(350)
36	203.84	0.16438	370.41	388.27	400
37	200.97	0.20248	406.13	424.57	
38	195.84	0.24393	443.01	461.90	(450)
39	188.65	0.28832	480.79	500.00	500
40	179.61	0.33515	519.21	538.591	(550)
41	168.99	0.38389	557.97	577.38	
42	157.06	0.43396	596.78	616.04	600
43	144.11	0.48477	635.31	654.27	(650)
44	130.43	0.53571	673.24	691.75	700
45	116.33	0.58617	710.26	728.16	
46	102.10	0.63555	746.06	763.20	(750), 775
47	88.02	0.68327	780.35	796.59	(800)
48	74.38	0.72879	812.83	828.05	(825)
49	61.44	0.77160	843.26	857.34	850
50	49.42	0.81125	871.42	884.27	(875)
51	38.51	0.84737	897.11	908.65	(900)
52	28.88	0.87966	920.19	930.37	925
53	20.64	0.90788	940.55	949.35	(950)
54	13.86	0.93194	958.15	965.57	
55	8.55	0.95182	972.99	979.06	(975)
56	4.67	0.96765	985.14	989.95	
57	2.10	0.97966	994.75	998.39	1000
58	0.66	0.98827	1002.02	1004.64	
59	0.07	0.99402	1007.26	1009.06	
60	0.00	0.99763	1010.85	1012.05	
	0.00	1.00000	1013.25		

ERA-20C

ERA-20C uses a hybrid sigma–pressure (hybrid σ-p) vertical coordinate (Simmons and Burridge, 1981), also sometimes referred to as an eta (η) vertical coordinate, with 91 levels. The pressure on each level is calculated as $p_k = A_k + B_k \times p_{\text{srf}}$, where p_{srf} is surface pressure. Table A2 provides example pressures at layer interfaces ($k - {}^1/_2$) and layer midpoints (k) for a surface pressure of 1013.25 hPa, from TOA to surface. Pressures at layer midpoints are defined as the average of pressures at layer interfaces.

Table A2: List of vertical levels used by ERA-20C.

	Model levels				Pressure levels
k	$A_{k-1/2}$ (hPa)	$B_{k-1/2}$	$p_{k-1/2}$ (hPa)	p_k (hPa)	p (hPa)
1	0	0	0	0.01	
2	0.02	0	0.02	0.03	
3	0.03980832	0	0.04	0.06	

4	0.07387186	0	0.07	0.10	
5	0.12908319	0	0.13	0.17	
6	0.21413612	0	0.21	0.28	
7	0.33952858	0	0.34	0.43	
8	0.51746601	0	0.52	0.64	
9	0.76167656	0	0.76	0.92	1
10	1.08715561	0	1.09	1.30	
11	1.50986023	0	1.51	1.78	2
12	2.04637451	0	2.05	2.38	
13	2.71356506	0	2.71	3.12	3
14	3.52824493	0	3.53	4.02	
15	4.50685791	0	4.51	5.09	5
16	5.66519226	0	5.67	6.34	7
17	7.01813354	0	7.02	7.80	
18	8.57945801	0	8.58	9.47	10
19	10.36166504	0	10.36	11.37	
20	12.37585449	0	12.38	13.50	
21	14.6316394	0	14.63	15.88	
22	17.13709595	0	17.14	18.52	
23	19.8987439	0	19.90	21.41	20
24	22.92155518	0	22.92	24.57	
25	26.20898438	0	26.21	27.99	
26	29.76302246	0	29.76	31.67	30
27	33.58425781	0	33.58	35.63	
28	37.67196045	0	37.67	39.85	
29	42.02416504	0	42.02	44.33	
30	46.63776367	0	46.64	49.07	50
31	51.50859863	0	51.51	54.07	
32	56.6315625	0	56.63	59.31	
33	61.99839355	0	62.00	64.80	
34	67.59727051	0	67.60	70.51	70
35	73.41469727	0	73.41	76.43	
36	79.4292627	0.000014	79.44	82.57	
37	85.64624023	0.000055	85.70	88.96	
38	92.08305664	0.000131	92.22	95.62	
39	98.73560547	0.000279	99.02	102.58	100
40	105.5888184	0.000548	106.14	109.89	
41	112.6248438	0.001	113.64	117.59	
42	119.8266211	0.001701	121.55	125.75	125
43	127.1389746	0.002765	129.94	134.40	
44	134.5322559	0.004267	138.86	143.59	
45	141.9200977	0.006322	148.33	153.35	150
46	149.2268555	0.009035	158.38	163.72	
47	156.3805371	0.012508	169.05	174.72	175
48	163.2956055	0.01686	180.38	186.38	

49	169.9062305	0.022189	192.39	198.76	200
50	176.1328125	0.02861	205.12	211.87	
51	181.910293	0.036227	218.62	225.77	225
52	187.1696875	0.045146	232.91	240.48	
53	191.8454492	0.055474	248.05	256.07	250
54	195.8751367	0.067316	264.08	272.56	
55	199.1979688	0.080777	281.05	290.02	
56	201.7539453	0.095964	298.99	308.48	300
57	203.4891602	0.112979	317.97	327.99	
58	204.341582	0.131935	338.02	348.62	350
59	204.2621875	0.152934	359.22	370.42	
60	203.1901172	0.176091	381.61	393.44	400
61	201.0703125	0.20152	405.26	417.73	
62	197.8535742	0.229315	430.21	443.34	450
63	193.4877539	0.259554	456.48	470.17	
64	187.9882227	0.291993	483.85	497.96	500
65	181.4129688	0.326329	512.07	526.46	
66	173.855957	0.362203	540.86	555.40	550
67	165.4458594	0.399205	569.94	584.49	
68	156.3356641	0.436906	599.03	613.50	600
69	146.6564551	0.475016	627.97	642.29	650
70	136.5321973	0.51328	656.61	670.73	
71	126.0838379	0.551458	684.85	698.70	700
72	115.4316699	0.589317	712.56	726.07	
73	104.7131055	0.626559	739.57	752.67	750
74	94.05222656	0.662934	765.77	778.40	775
75	83.5625293	0.698224	791.04	803.16	800
76	73.35164551	0.732224	815.28	826.81	825
77	63.53920898	0.764679	838.35	849.25	850
78	54.22802734	0.795385	860.15	870.38	875
79	45.5021582	0.824185	880.61	890.13	
80	37.43464355	0.85095	899.66	908.44	900
81	30.10146973	0.875518	917.22	925.22	925
82	23.56202637	0.897767	933.22	940.44	
83	17.84854614	0.917651	947.66	954.09	950
84	12.97656128	0.935157	960.52	966.17	
85	8.95193542	0.950274	971.82	976.67	975
86	5.76314148	0.963007	981.53	985.63	
87	3.36772369	0.973466	989.73	993.30	
88	1.62043427	0.982238	996.87	999.84	1000
89	0.54208336	0.989153	1002.80	1005.12	
90	0.06575628	0.994204	1007.44	1009.15	
91	0.0000316	0.99763	1010.85	1012.05	
	0	1	1013.25		

ERA5

ERA5 uses a hybrid sigma–pressure (hybrid σ-p) vertical coordinate (Simmons and Burridge, 1981), also sometimes referred to as an eta (η) vertical coordinate, with 137 levels. The pressure on each level is calculated as $p_k = A_k + B_k \times p_{\text{srf}}$, where p_{srf} is surface pressure. Table A3 provides example pressures at layer interfaces ($k - {}^1/_2$) and layer midpoints (k) for a surface pressure of 1013.25 hPa, from TOA to surface. Pressures at layer midpoints are defined as the average of pressures at layer interfaces.

Table A3: List of vertical levels used by ERA5.

Model levels					Pressure levels
k	$A_{k-1/2}$ (hPa)	$B_{k-1/2}$	$p_{k-1/2}$ (hPa)	p_k (hPa)	p (hPa)
1	0	0	0.00	0.01	
2	0.02000365	0	0.02	0.03	
3	0.03102241	0	0.03	0.04	
4	0.04666084	0	0.05	0.06	
5	0.06827977	0	0.07	0.08	
6	0.09746966	0	0.10	0.12	
7	0.13605424	0	0.14	0.16	
8	0.18608931	0	0.19	0.22	
9	0.24985718	0	0.25	0.29	
10	0.3298571	0	0.33	0.38	
11	0.42879242	0	0.43	0.49	
12	0.54955463	0	0.55	0.62	
13	0.69520576	0	0.70	0.78	
14	0.86895882	0	0.87	0.97	1
15	1.07415741	0	1.07	1.19	
16	1.31425507	0	1.31	1.45	
17	1.59279404	0	1.59	1.75	
18	1.91338562	0	1.91	2.10	2
19	2.27968948	0	2.28	2.49	
20	2.69539581	0	2.70	2.93	3
21	3.16420746	0	3.16	3.43	
22	3.68982361	0	3.69	3.98	
23	4.27592499	0	4.28	4.60	
24	4.92616028	0	4.93	5.29	5
25	5.64413452	0	5.64	6.04	
26	6.43339905	0	6.43	6.87	7
27	7.29744141	0	7.30	7.77	
28	8.23967834	0	8.24	8.75	
29	9.2634491	0	9.26	9.82	10
30	10.37201172	0	10.37	10.97	
31	11.56853638	0	11.57	12.21	
32	12.85610352	0	12.86	13.55	
33	14.23770142	0	14.24	14.98	
34	15.71622925	0	15.72	16.51	

35	17.29448975	0	17.29	18.13	
36	18.97519287	0	18.98	19.87	20
37	20.76095947	0	20.76	21.71	
38	22.65431641	0	22.65	23.66	
39	24.65770508	0	24.66	25.72	
40	26.77348145	0	26.77	27.89	
41	29.00391357	0	29.00	30.18	30
42	31.35119385	0	31.35	32.58	
43	33.81743652	0	33.82	35.11	
44	36.40468262	0	36.40	37.76	
45	39.11490479	0	39.11	40.53	
46	41.94930664	0	41.95	43.43	
47	44.90817383	0	44.91	46.45	
48	47.99149414	0	47.99	49.60	50
49	51.1989502	0	51.20	52.86	
50	54.52990723	0	54.53	56.26	
51	57.98344727	0	57.98	59.77	
52	61.56074219	0	61.56	63.42	
53	65.26946777	0	65.27	67.19	
54	69.11870605	0	69.12	71.12	70
55	73.11869141	0	73.12	75.20	
56	77.27412109	0.000007	77.28	79.45	
57	81.59354004	0.000024	81.62	83.88	
58	86.08525391	0.000059	86.15	88.51	
59	90.76400391	0.000112	90.88	93.35	
60	95.62682617	0.000199	95.83	98.42	
61	100.6597852	0.00034	101.00	103.71	100
62	105.8463184	0.000562	106.42	109.24	
63	111.1666211	0.00089	112.07	115.02	
64	116.6006738	0.001353	117.97	121.05	
65	122.1154785	0.001992	124.13	127.35	125
66	127.6687305	0.002857	130.56	133.92	
67	133.2466895	0.003971	137.27	140.77	
68	138.8133106	0.005378	144.26	147.91	150
69	144.3213965	0.007133	151.55	155.34	
70	149.7561523	0.009261	159.14	163.09	
71	155.0825684	0.011806	167.04	171.16	175
72	160.2611523	0.014816	175.27	179.55	
73	165.2732227	0.018318	183.83	188.29	
74	170.0878906	0.022355	192.74	197.37	200
75	174.6761328	0.026964	202.00	206.81	
76	179.0162109	0.032176	211.62	216.62	
77	183.0843359	0.038026	221.61	226.80	225
78	186.8571875	0.044548	232.00	237.38	
79	190.3128906	0.051773	242.77	248.36	250

80	193.4351172	0.059728	253.95	259.75	
81	196.2004297	0.068448	265.56	271.57	
82	198.5939063	0.077958	277.58	283.82	
83	200.5993164	0.088286	290.06	296.52	300
84	202.1966406	0.099462	302.98	309.67	
85	203.3786328	0.111505	316.36	323.29	
86	204.1230859	0.124448	330.22	337.39	
87	204.4207813	0.138313	344.57	351.99	350
88	204.2571875	0.153125	359.41	367.09	
89	203.6181641	0.16891	374.77	382.71	
90	202.4951172	0.185689	390.64	398.85	400
91	200.8708594	0.203491	407.06	415.54	
92	198.7402539	0.222333	424.02	432.78	
93	196.0857227	0.242244	441.54	450.59	450
94	192.9022656	0.263242	459.63	468.97	
95	189.1746094	0.285354	478.31	487.95	
96	184.8970703	0.308598	497.58	507.50	500
97	180.0692578	0.332939	517.42	527.57	
98	174.7183984	0.358254	537.72	548.03	550
99	168.886875	0.384363	558.34	568.77	
100	162.6204688	0.411125	579.19	589.68	600
101	155.9669531	0.438391	600.17	610.66	
102	148.9845313	0.466003	621.16	631.62	
103	141.7332422	0.4938	642.08	652.44	650
104	134.2776953	0.521619	662.81	673.03	
105	126.6825781	0.549301	683.26	693.30	700
106	119.0133984	0.576692	703.35	713.16	
107	111.3330469	0.603648	722.98	732.53	
108	103.7017578	0.630036	742.09	751.34	750
109	96.17515625	0.655736	760.60	769.53	775
110	88.80453125	0.680643	778.47	787.05	
111	81.63375	0.704669	795.64	803.86	800
112	74.7034375	0.727739	812.08	819.93	825
113	68.04421875	0.749797	827.78	835.24	
114	61.6853125	0.770798	842.70	849.77	850
115	55.64382813	0.790717	856.84	863.52	
116	49.93796875	0.809536	870.20	876.50	875
117	44.57375	0.827256	882.79	888.71	
118	39.55960938	0.843881	894.62	900.17	900
119	34.89234375	0.859432	905.71	910.90	
120	30.57265625	0.873929	916.08	920.92	925
121	26.59140625	0.887408	925.76	930.26	
122	22.94242188	0.8999	934.77	938.95	
123	19.615	0.911448	943.14	947.02	
124	16.59476563	0.922096	950.91	954.51	950

125	13.87546875	0.931881	958.10	961.43	
126	11.4325	0.94086	964.76	967.83	
127	9.26507813	0.949064	970.90	973.74	975
128	7.34992188	0.95655	976.57	979.19	
129	5.680625	0.963352	981.80	984.20	
130	4.24414063	0.969513	986.60	988.81	
131	3.02476563	0.975078	991.02	993.05	
132	2.02484375	0.980072	995.08	996.95	
133	1.22101563	0.984542	998.81	1000.52	1000
134	0.6278125	0.9885	1002.23	1003.79	
135	0.22835938	0.991984	1005.36	1006.79	
136	0.03757813	0.995003	1008.22	1009.54	
137	0	0.99763	1010.85	1012.05	
	0	1	1013.25		

JRA-25/JCDAS

JRA-25 and its extension JCDAS use a hybrid sigma–pressure (hybrid σ-p) vertical coordinate (Simmons and Burridge, 1981) with 40 levels. The pressure on each level is calculated as $p_k = A_k + B_k \times p_{\mathrm{srf}}$, where p_{srf} is surface pressure. Table A4 provides example pressures at layer interfaces ($k - {}^1/_2$) and layer midpoints (k) for a surface pressure of 1013.25 hPa, from TOA to surface. Pressures at layer midpoints are defined as the average of pressures at layer interfaces.

Table A4: List of vertical levels used by JRA-25/JCDAS.

Model levels					Pressure levels
k	$A_{k-1/2}$ (hPa)	$B_{k-1/2}$	$p_{k-1/2}$ (hPa)	p_k (hPa)	p (hPa)
1	0.000000	0.000000	0.00	0.40	0.4
2	0.800000	0.000000	0.80	1.13	1
3	1.460000	0.000000	1.46	2.01	2
4	2.560000	0.000000	2.56	3.45	3
5	4.330000	0.000000	4.33	5.72	5
6	7.100000	0.000000	7.10	9.15	7
7	11.200000	0.000000	11.20	14.10	10
8	17.000000	0.000000	17.00	21.00	20
9	25.000000	0.000000	25.00	30.15	30
10	35.299999	0.000000	35.30	41.70	
11	48.099998	0.000000	48.10	55.55	50
12	62.634430	0.000366	63.01	71.53	70
13	76.105057	0.003895	80.05	89.60	
14	88.363998	0.010636	99.14	109.71	100
15	98.876595	0.021123	120.28	131.88	
16	107.299492	0.035701	143.47	156.10	150
17	113.447090	0.054553	168.72	182.38	
18	117.259979	0.077740	196.03	210.71	200
19	118.777374	0.105223	225.39	241.10	250
20	118.113609	0.136886	256.81	273.55	

21	115.438545	0.172561	290.29	308.05	300
22	110.961449	0.212039	325.81	344.09	
23	105.094887	0.253905	362.36	381.16	
24	98.151306	0.297849	399.95	419.76	400
25	90.192863	0.344807	439.57	460.40	
26	81.437820	0.394562	481.23	502.57	500
27	72.323532	0.445676	523.90	545.75	
28	63.056015	0.497944	567.60	589.95	600
29	53.811684	0.551188	612.30	635.16	
30	44.741348	0.605259	658.02	680.87	700
31	36.158020	0.658842	703.73	726.58	
32	28.130577	0.711869	749.43	771.77	
33	20.862747	0.763137	794.11	815.43	
34	14.485500	0.811514	836.75	856.55	850
35	9.064261	0.855936	876.34	894.10	
36	4.611954	0.895388	911.86	932.15	925
37	1.105610	0.938894	952.44	960.05	
38	0.000000	0.955000	967.65	977.79	
39	0.000000	0.975000	987.92	995.52	1000
40	0.000000	0.990000	1003.12	1008.18	
	0.000000	1.000000	1013.25		

JRA-55 and companion products

JRA-55 and its companion products JRA-55C and JRA-55AMIP use a hybrid sigma–pressure (hybrid σ-p) vertical coordinate (Simmons and Burridge, 1981) with 60 levels. The pressure on each level is calculated as $p_k = A_k + B_k \times p_{\mathrm{srf}}$, where p_{srf} is surface pressure. Table A5 provides example pressures at layer interfaces ($k - {}^1/_2$) and layer midpoints (k) for a surface pressure of 1013.25 hPa, from TOA to surface. Pressures at layer midpoints are defined as the average of pressures at layer interfaces.

Table A5: List of vertical levels used by JRA-55.

Model levels					Pressure levels
k	$A_{k-1/2}$ (hPa)	$B_{k-1/2}$	$p_{k-1/2}$ (hPa)	p_k (hPa)	p (hPa)
1	0.000000	0.000000	0.00	0.10	
2	0.200000	0.000000	0.20	0.30	
3	0.390000	0.000000	0.39	0.52	
4	0.650000	0.000000	0.65	0.81	
5	0.970000	0.000000	0.97	1.17	1
6	1.360000	0.000000	1.36	1.59	
7	1.820000	0.000000	1.82	2.10	2
8	2.370000	0.000000	2.37	2.69	
9	3.010000	0.000000	3.01	3.39	3
10	3.770000	0.000000	3.77	4.23	
11	4.690000	0.000000	4.69	5.25	5
12	5.810000	0.000000	5.81	6.51	7

13	7.200000	0.000000	7.20	8.07	
14	8.930000	0.000000	8.93	9.99	10
15	11.050000	0.000000	11.05	12.38	
16	13.700000	0.000000	13.70	15.35	
17	17.000000	0.000000	17.00	19.03	20
18	21.050000	0.000000	21.05	23.58	
19	26.100000	0.000000	26.10	29.20	30
20	32.300000	0.000000	32.30	36.15	
21	40.000000	0.000000	40.00	44.75	
22	49.500000	0.000000	49.50	55.25	50
23	60.886730	0.000113	61.00	67.77	70
24	72.015690	0.002484	74.53	81.81	
25	82.262449	0.006738	89.09	97.13	100
26	91.672470	0.013328	105.18	114.24	
27	100.146151	0.022854	123.30	133.39	125
28	107.299494	0.035701	143.47	154.58	150
29	112.854041	0.052146	165.69	177.82	175
30	116.633554	0.072366	189.96	203.12	200
31	118.554343	0.096446	216.28	230.46	225
32	118.612531	0.124387	244.65	259.35	250
33	116.953716	0.155046	274.05	289.78	300
34	113.696478	0.189304	305.51	321.75	
35	109.126384	0.225874	337.99	355.26	350
36	103.294362	0.265706	372.52	390.30	400
37	96.561819	0.307438	408.07	426.36	
38	89.140822	0.350859	444.65	463.45	450
39	81.221598	0.395778	482.24	501.55	500
40	72.974699	0.442025	520.86	540.16	550
41	64.767182	0.488233	559.47	578.77	
42	56.718242	0.534282	598.08	617.38	600
43	48.918808	0.580081	636.69	655.48	650
44	41.629564	0.62437	674.27	693.06	700
45	34.688715	0.668311	711.85	729.63	750
46	28.474848	0.709525	747.40	764.16	775
47	22.948417	0.748052	780.91	797.16	800
48	17.909074	0.785091	813.40	828.63	825
49	13.4768	0.819523	843.86	858.07	850
50	9.597972	0.851402	872.28	884.97	875
51	6.346027	0.879654	897.66	908.82	900
52	3.649041	0.904351	919.98	930.13	925
53	1.33051	0.926669	940.28	949.41	950
54	0	0.946	958.53	965.63	
55	0	0.96	972.72	978.80	975
56	0	0.972	984.88	989.95	
57	0	0.982	995.01	998.56	1000

58	0	0.989	1002.10	1004.64	
59	0	0.994	1007.17	1008.69	
60	0	0.997	1010.21	1011.73	
	0	1	1013.25		

MERRA and MERRA-2

MERRA and MERRA-2 use a hybrid sigma–pressure (hybrid σ-p) vertical coordinate (Simmons and Burridge, 1981) with 72 levels. The pressure on each level is calculated as $p_k = A_k + B_k \times p_{\text{srf}}$, where p_{srf} is surface pressure. Table A6 provides example pressures at layer interfaces ($k-{}^1/_2$) and layer midpoints (k) for a surface pressure of 1013.25 hPa, from TOA to surface. Pressures at layer midpoints are defined as the average of pressures at layer interfaces. NASA GMAO is planning to transition away from this vertical grid and recommends that data users use the three-dimensional pressure fields provided with MERRA and MERRA-2 model level products instead.

Table A6: List of vertical levels used by MERRA and MERRA-2.

Model levels					Pressure levels
k	$A_{k-1/2}$ (hPa)	$B_{k-1/2}$	$p_{k-1/2}$ (hPa)	p_k (hPa)	p (hPa)
1	0.0100	0	0.01	0.015	
2	0.0200	0	0.02	0.026	
3	0.0327	0	0.03	0.040	
4	0.0476	0	0.05	0.057	
5	0.0660	0	0.07	0.078	
6	0.0893	0	0.09	0.105	0.1
7	0.1197	0	0.12	0.140	
8	0.1595	0	0.16	0.185	
9	0.2113	0	0.21	0.245	
10	0.2785	0	0.28	0.322	0.3
11	0.3650	0	0.37	0.420	0.4
12	0.4758	0	0.48	0.546	0.5
13	0.6168	0	0.62	0.706	0.7
14	0.7951	0	0.80	0.907	1
15	1.0194	0	1.02	1.160	
16	1.3005	0	1.30	1.476	
17	1.6508	0	1.65	1.868	2
18	2.0850	0	2.08	2.353	
19	2.6202	0	2.62	2.948	3
20	3.2764	0	3.28	3.677	4
21	4.0766	0	4.08	4.562	5
22	5.0468	0	5.05	5.632	
23	6.2168	0	6.22	6.918	7
24	7.6198	0	7.62	8.456	
25	9.2929	0	9.29	10.29	10
26	11.2769	0	11.28	12.46	
27	13.6434	0	13.64	15.05	
28	16.4571	0	16.46	18.12	

29	19.7916	0	19.79	21.76	20
30	23.7304	0	23.73	26.05	
31	28.3678	0	28.37	31.09	30
32	33.8100	0	33.81	36.99	40
33	40.1754	0	40.18	43.91	
34	47.6439	0	47.64	52.02	50
35	56.3879	0	56.39	61.50	
36	66.6034	0	66.60	72.56	70
37	78.5123	0	78.51	85.44	
38	92.3657	0	92.37	100.51	100
39	108.6630	0	108.66	118.25	
40	127.8370	0	127.84	139.12	150
41	150.3930	0	150.39	163.66	
42	176.9300	0	176.93	192.59	200
43	201.1920	0.006960	208.24	226.75	
44	216.8650	0.028010	245.25	267.09	250
45	224.3630	0.063720	288.93	313.97	300
46	223.8980	0.113602	339.01	358.04	350
47	218.7760	0.156224	377.07	396.11	400
48	212.1500	0.200350	415.15	434.21	450
49	203.2590	0.246741	453.27	472.34	
50	193.0970	0.294403	491.40	510.48	500
51	181.6190	0.343381	529.55	548.63	550
52	169.6090	0.392891	567.71	586.79	600
53	156.2600	0.443740	605.88	624.97	
54	142.9100	0.494590	644.05	663.15	650
55	128.6960	0.546304	682.24	694.97	700
56	118.9590	0.581041	707.70	720.43	725
57	109.1820	0.615818	733.16	745.89	750
58	99.3652	0.650635	758.62	771.36	775
59	89.0999	0.685900	784.09	796.82	800
60	78.8342	0.721166	809.56	819.74	825
61	70.6220	0.749378	829.93	837.57	
62	64.3626	0.770637	845.21	852.85	850
63	58.0532	0.791947	860.49	868.14	875
64	51.6961	0.813304	875.78	883.42	
65	45.3390	0.834661	891.06	898.70	900
66	38.9820	0.856018	906.34	913.98	
67	32.5708	0.877429	921.63	929.27	925
68	26.0920	0.898908	936.91	944.55	950
69	19.6131	0.920387	952.20	959.84	
70	13.1348	0.941865	967.48	975.12	975
71	6.5938	0.963406	982.76	990.41	
72	0.0480	0.984952	998.05	1005.65	1000

	0	1	1013.25		

NCEP-NCAR R1 and NCEP-DOE R2

NCEP-NCAR R1 and NCEP-DOE R2 use a sigma (σ) vertical coordinate (Simmons and Burridge, 1981) with 28 levels. The pressure on each level is calculated as $p_k = \sigma_k \times p_{\text{srf}}$, where p_{srf} is surface pressure. Table A7 provides example pressures at each level for a surface pressure of 1013.25 hPa, from TOA to surface.

Table A7: List of vertical levels used by R1 and R2.

Model levels			Pressure levels
k	σ_k	p_k (hPa)	p (hPa)
1	0.00273	2.77	3
2	0.01006	10.19	10
3	0.01834	18.58	20
4	0.02875	29.13	30
5	0.04179	42.34	
6	0.05805	58.82	50
7	0.07815	79.19	70
8	0.10278	104.14	100
9	0.13261	134.37	
10	0.16823	170.46	150
11	0.21006	212.84	200
12	0.25823	261.65	250
13	0.31248	316.62	300
14	0.37205	376.98	400
15	0.43568	441.45	
16	0.50168	508.33	500
17	0.56809	575.62	
18	0.63290	641.29	
19	0.69426	703.46	700
20	0.75076	760.71	
21	0.80142	812.04	
22	0.84579	857.00	850
23	0.88384	895.55	
24	0.91592	928.06	925
25	0.94255	955.04	
26	0.96437	977.15	
27	0.98208	995.09	
28	0.99500	1008.18	1000
	1.00000	1013.25	

CFSR/CFSv2

CFSR and CFSv2 use a hybrid sigma–pressure (hybrid σ-p) vertical coordinate (Simmons and Burridge, 1981) with 64 levels. The pressure on each level is calculated as $p_k = A_k + B_k \times p_{\text{srf}}$, where p_{srf} is surface pressure. Table A8 provides example pressures at layer interfaces ($k - {}^1/_2$)

and layer midpoints (k) for a surface pressure of 1013.25 hPa, from TOA to surface. Pressures at layer midpoints are defined as the average of pressures at layer interfaces.

Table A8: List of vertical levels used by CFSR and CFSv2.

Model levels					Pressure levels
k	$A_{k-1/2}$ (hPa)	$B_{k-1/2}$	$p_{k-1/2}$ (hPa)	p_k (hPa)	p (hPa)
1	0.00000	0.000000	0.00	0.32	
2	0.64247	0.000000	0.64	1.01	1
3	1.37790	0.000000	1.38	1.80	2
4	2.21958	0.000000	2.22	2.70	3
5	3.18266	0.000000	3.18	3.73	
6	4.28434	0.000000	4.28	4.91	5
7	5.54424	0.000000	5.54	6.26	
8	6.98457	0.000000	6.98	7.81	7
9	8.63058	0.000000	8.63	9.57	10
10	10.51080	0.000000	10.51	11.58	
11	12.65752	0.000000	12.66	13.88	
12	15.10711	0.000000	15.11	16.50	
13	17.90051	0.000000	17.90	19.49	20
14	21.08366	0.000000	21.08	22.90	
15	24.70788	0.000000	24.71	26.77	
16	28.83038	0.000000	28.83	31.17	30
17	33.51460	0.000000	33.51	36.17	
18	38.83052	0.000000	38.83	41.84	
19	44.85493	0.000000	44.85	48.26	50
20	51.67146	0.000000	51.67	55.52	
21	59.37050	0.000000	59.37	63.71	
22	68.04874	0.000000	68.05	72.93	70
23	77.77150	0.000037	77.81	83.29	
24	88.32537	0.000431	88.76	94.89	100
25	99.36614	0.001636	101.02	107.87	
26	110.54853	0.004107	114.71	122.32	125
27	121.52937	0.008294	129.93	138.37	
28	131.97065	0.014637	146.80	156.11	150
29	141.54316	0.023556	165.41	175.63	175
30	149.93074	0.035442	185.84	197.00	200
31	156.83489	0.050647	208.15	220.26	225
32	161.97967	0.069475	232.37	245.44	250
33	165.11736	0.092167	258.51	272.50	
34	166.11603	0.118812	286.50	301.39	300
35	165.03144	0.149269	316.28	331.99	
36	161.97315	0.183296	347.70	364.14	350
37	157.08893	0.220570	380.58	397.64	400
38	150.56342	0.260685	414.70	432.25	
39	142.61435	0.303164	449.80	467.68	450

40	133.48671	0.347468	485.56	503.61	500
41	123.44490	0.393018	521.67	539.73	550
42	112.76348	0.439211	557.79	575.69	
43	101.71712	0.485443	593.59	611.17	600
44	90.57051	0.531135	628.74	645.84	650
45	79.56908	0.575747	662.94	679.44	
46	68.93117	0.618800	695.93	711.70	700
47	58.84206	0.659887	727.47	742.43	750
48	49.45029	0.698683	757.39	771.47	775
49	40.86614	0.734945	785.55	798.70	800
50	33.16217	0.768515	811.86	824.07	825
51	26.37553	0.799310	836.28	847.53	850
52	20.51150	0.827319	858.79	869.11	875
53	15.54789	0.852591	879.44	888.85	
54	11.43988	0.875224	898.26	906.80	900
55	8.12489	0.895355	915.34	923.06	925
56	5.52720	0.913151	930.78	937.72	
57	3.56223	0.928797	944.67	950.89	950
58	2.14015	0.942491	957.12	962.68	
59	1.16899	0.954434	968.25	973.21	975
60	0.55712	0.964828	978.17	982.58	
61	0.21516	0.973868	986.99	990.90	
62	0.05741	0.981742	994.81	998.27	1000
63	0.00575	0.988627	1001.73	1004.79	
64	0.00000	0.994671	1007.85	1010.55	
	0.00000	1.000000	1013.25		

NOAA-CIRES 20CR v2

NOAA-CIRES 20CR v2 uses a hybrid sigma–pressure (hybrid σ-p) vertical coordinate (Simmons and Burridge, 1981) with 28 levels. The pressure on each level is calculated as $p_k = A_k + B_k \times p_{\text{srf}}$, where p_{srf} is surface pressure. Table A9 provides example pressures at layer interfaces ($k - {}^1/_2$) and layer midpoints (k) for a surface pressure of 1013.25 hPa, from TOA to surface. Pressures at layer midpoints are defined as the average of pressures at layer interfaces.

Table A9: List of vertical levels used by 20CR.

	Model levels				Pressure levels
k	$A_{k-1/2}$ (hPa)	$B_{k-1/2}$	$p_{k-1/2}$ (hPa)	p_k (hPa)	p (hPa)
1	0.00000	0.000000	0.00	2.83	
2	5.66898	0.000000	5.67	9.29	10
3	12.90533	0.000000	12.91	17.51	20
4	22.10979	0.000000	22.11	27.94	30
5	33.76516	0.000000	33.77	41.10	
6	48.44036	0.000000	48.44	57.61	50
7	66.78608	0.000000	66.79	78.15	70
8	89.13767	0.000379	89.52	103.47	100

9	113.43654	0.003933	117.42	134.33	150
10	136.71427	0.014326	151.23	171.39	
11	156.13564	0.034950	191.55	215.13	200
12	169.12130	0.068675	238.71	265.66	250
13	173.64658	0.117418	292.62	322.64	300,350
14	169.59994	0.180667	352.66	385.13	400
15	158.12926	0.256084	417.61	451.65	450
16	140.89535	0.340293	485.70	520.25	500,550
17	119.91428	0.429195	554.80	588.72	600
18	97.31807	0.518457	622.64	654.89	650
19	75.08532	0.604055	687.14	716.87	700
20	54.81144	0.682747	746.60	773.25	750
21	37.57142	0.752347	799.89	823.16	800
22	23.89205	0.811785	846.43	866.32	850
23	13.81526	0.860975	886.20	902.86	900
24	7.01453	0.900581	919.53	933.27	
25	2.92577	0.931750	947.02	958.21	950
26	0.86457	0.955872	969.40	978.42	
27	0.11635	0.974402	987.43	994.63	1000
28	0.00009	0.988726	1001.83	1007.54	
	0.00000	1.000000	1013.25		

B List of Acronyms and Terms

20CR	20th Century Reanalysis.
2D-Var	2-dimensional variational assimilation scheme.
3D-FGAT	3-dimensional variational assimilation scheme with FGAT.
3D-Var	3-dimensional variational assimilation scheme.
4D-Var	4-dimensional variational assimilation scheme.
ABL	atmospheric boundary layer.
ACARS	Aircraft Communications Addressing and Reporting System.
ACRE	Atmospheric Circulation Reconstructions over the Earth.
AER	Atmospheric and Environmental Research.
AERONET	Aerosol Robotic Network.
AGCM	atmospheric general circulation model.
AHI	Advanced Himawari Imager.
AIRS	Atmospheric Infrared Sounder.
AMDAR	Aircraft Meteorological Data Relay.
AMIP	Atmospheric Model Intercomparison Project.
AMSR	Advanced Microwave Scanning Radiometer.
AMSR-E	Advanced Microwave Scanning Radiometer for EOS.
AMSU	Advanced Microwave Sounding Unit.
AMV	atmospheric motion vectors.
ANA	"analyzed" state produced prior to IAU for MERRA and MERRA-2.
AOD	aerosol optical depth.
Aqua	a satellite in NASAs EOS A-Train constellation.
ASCAT	Advanced Scatterometer.
ASM	"assimilated" state produced by IAU for MERRA and MERRA-2.
ATMS	Advanced Technology Microwave Sounder.
ATOVS	Advanced TIROS Operational Vertical Sounder.
Aura	a satellite in NASAs EOS A-Train constellation.
AVHRR	Advanced Very High Resolution Radiometer.
BAS	British Antarctic Survey.
BOM	Bureau of Meteorology (Australia).
BUOY	Surface meteorological observation report from buoys.
C/NOFS	Communication/Navigation Outage Forecast System.
CAMSiRA	Copernicus Atmosphere Monitoring Service Interim Reanalysis.
CAPE	convective available potential energy.
CCARDS	Comprehensive Aerological Reference Dataset, Core Subset.
CCI	Climate Change Initiative (ESA).
CEDA	Centre for Environmental Data Analysis.
CERA	a coupled atmosphere–ocean data assimilation system developed by ECMWF.
CFC	chlorofluorocarbon.

CFS	Climate Forecast System developed by NCEP.
CFSR	Climate Forecast System Reanalysis (NCEP).
CFSv2	Climate Forecast System Version 2 (NCEP).
CHAMP	CHAllenging Minisatellite Payload.
CIRES	Cooperative Institute for Research in Environmental Sciences (a cooperation between NOAA and the University of Colorado at Boulder).
CLIRAD	models for shortwave and longwave radiative transfer developed at NASA GMAO.
CMA	China Meteorological Administration.
CMAP	CPC Merged Analysis of Precipitation.
CMIP5	Coupled Model Intercomparison Project Phase 5.
CNSA	China National Space Administration.
COBE	Centennial in-situ Observation-Based Estimates of variability of SST and marine meteorological variables.
conventional input	a class of reanalysis that assimilates surface and upper-air conventional data but does not assimilate satellite data.
CORISS	C/NOFS Occultation Receiver for Ionospheric Sensing and Specification.
COSMIC	Constellation Observing System for Meteorology, Ionosphere, and Climate.
CPC	Climate Prediction Center (NOAA).
CRIEPI	Central Research Institute of Electric Power Industry.
CrIS	Cross-track Infrared Sounder.
CRTM	Community Radiative Transfer Model.
CRUTEM	Climatic Research Unit Air Temperature Anomalies.
CTM	chemical transport model.
DAO	Data Assimilation Office (NASA; now GMAO).
DAS	data assimilation system.
DMSP	Defense Meteorological Satellite Program.
DOAS	Differential Optical Absorption Spectroscopy.
DOE	Department of Energy.
ECMWF	European Centre for Medium-Range Weather Forecasts.
EDA	the 10-member "ensemble of data assimilations" produced for ERA5.
EDMF	eddy-diffusivity mass-flux.
EMC	Ensemble Modeling Center.
EnKF	Ensemble Kalman Filter assimilation scheme.
EOS	Earth Observing System (NASA).
ERA-15	ECMWF 15-year reanalysis.
ERA-20C	ECMWF 20th century reanalysis.
ERA-20CM	an AMIP ensemble using the same atmospheric model as ERA-20C.
ERA-40	ECMWF 40-year reanalysis.
ERA-CLIM	European Reanalysis of Global Climate Observations.
ERA-Interim	ECMWF interim reanalysis.
ERA5	the fifth major global reanalysis produced by ECMWF.

ERA5L	a land surface reanalysis with atmospheric forcing from ERA5.
ERS	European Remote Sensing satellite.
ESA	European Space Agency.
EUMETSAT	European Organisation for the Exploitation of Meteorological Satellites.
extended	a descriptor for reanalyses that provide data for dates before January 1979.
FGAT	first guess at appropriate time.
FGGE	First GARP Global Experiment.
FORMOSAT	Name given to the Republic of China Satellite (ROCSat) following a public naming competition.
full input	a class of reanalysis that assimilates both upper-air conventional and satellite data as well as surface data.
FY-3	FengYun-3 (a series of polar-orbiting meteorological satellites launched by the CMA and CNSA).
GAAS	Goddard Aerosol Assimilation System.
GARP	Global Atmospheric Research Program.
GATE	GARP (Global Atmospheric Research Program) Atlantic Tropical Experiment.
GAW	Global Atmosphere Watch.
GCM	general circulation model.
GEO	geostationary satellites.
GEOS	Goddard Earth Observing System Model (NASA).
GFDL	Geophysical Fluid Dynamics Laboratory (NOAA).
GFS	Global Forecast System (NCEP).
GISST	a Global Ice and Sea Surface Temperature dataset produced by UKMO.
GLATOVS	Goddard Laboratory for Atmospheres TOVS (a radiative transfer model).
GLCC	Global Land Cover Characteristics data base.
GLDAS	Global Land Data Assimilation System.
GMAO	Global Modeling and Assimilation Office (NASA).
GMI	GPM Microwave Imager.
GMS	Geostationary Meteorological Satellite.
GNSS-RO	Global Navigation Satellite System Radio Occultation (see also GPS-RO).
GOCART	Goddard Chemistry, Aerosol, Radiation, and Transport model.
GODAS	NCEP Global Ocean Data Assimilation System.
GOES	Geostationary Operational Environmental Satellite.
GOME	Global Ozone Monitoring Experiment.
GPCP	Global Precipitation Climatology Project.
GPM	Global Precipitation Measurement mission.
gpm	geopotential metres.
GPS-RO	Global Positioning System Radio Occultation (see also GNSS-RO).
GRACE	Gravity Recovery and Climate Experiment.
GRAS	GNSS Receiver for Atmospheric Sounding.
GRIB	General Regularly-distributed Information in Binary form.
GRIB2	GRIB, Version 2.

GRUAN	Global Climate Observing System Reference Upper Air Network.
GSI	Gridpoint Statistical Interpolation (an assimilation scheme).
GSICS	Global Space-based Inter-calibration System.
GSM	Global Spectral Model of the JMA.
GTS	Global Telecommunication System.
GWD	gravity wave drag.
HadISST	UKMO Hadley Centre Sea Ice and SST dataset.
HALOE	Halogen Occultation Experiment.
HCFC	hydrochlorofluorocarbon.
HDF	Hierarchical Data Format.
HIRS	High-resolution Infrared Radiation Sounder.
HITRAN	High-resolution Transmission molecular absorption database.
HRES	the high-resolution analysis produced for ERA5.
IASI	Infrared Atmospheric Sounding Interferometer.
IAU	Incremental Analysis Update procedure (or products resulting from that procedure).
ICOADS	International Comprehensive Ocean-Atmosphere Data Set.
IFS	Integrated Forecast System of the ECMWF.
IGY	International Geophysical Year (July 1957–December 1958).
IMS	Interactive Multisensor Snow and Ice Mapping System.
IPCC	Intergovernmental Panel on Climate Change.
IR	infrared.
ISPD	International Surface Pressure Databank.
JAXA	Japan Aerospace Exploration Agency.
JCDAS	JMA Climate Data Assimilation System.
JCSDA	Joint Center for Satellite Data Assimilation.
JMA	Japan Meteorological Agency.
JRA-25	Japanese 25-year Reanalysis.
JRA-55	Japanese 55-year Reanalysis.
JRA-55AMIP	Japanese 55-year Reanalysis based on AMIP-type simulations.
JRA-55C	Japanese 55-year Reanalysis assimilating Conventional observations only.
KNMI	Royal Netherlands Meteorological Institute.
LAI	leaf area index.
LCL	lifting condensation level.
LEO/GEO	Low Earth Orbit / Geostationary.
LFC	level of free convection.
LIE	Line Islands Experiment.
LSM	land surface model.
MARS	Meteorological Archival and Retrieval System of the ECMWF.

McICA	Monte Carlo Independent Column Approximation.
MERRA	Modern Era Retrospective-Analysis for Research.
MERRA-2	Modern Era Retrospective-Analysis for Research Version 2.
Met Office	see UKMO.
METEOSAT	geostationary meteorological satellites operated by EUMETSAT.
MetOp	A series of three polar orbiting meteorological satellites operated by EUMETSAT.
MHS	Microwave Humidity Sounder.
MIPAS	Michelson Interferometer for Passive Atmospheric Sounding.
MISR	Multiangle Imaging Spectroradiometer.
MIT	Massachusetts Institute of Technology.
MLS	Microwave Limb Sounder.
MODIS	MODerate resolution Imaging Spectroradiometer.
MOM	Modular Ocean Model.
MRF	Medium Range Forecast Version of the NCEP GFS.
MRI	Meteorological Research Institute (JMA).
MRI-CCM1	MRI Chemistry Climate Model version 1.
MSE	moist static energy.
MSU	Microwave Sounding Unit.
MTSAT	Multi-functional Transport Satellite.
MW	microwave.
NASA	National Aeronautics and Space Administration.
NCAR	National Center for Atmospheric Research.
NCDC	National Climatic Data Center (NOAA).
NCEP	National Centers for Environmental Prediction (NOAA).
NCEP-DOE R2	Reanalysis 2 of the NCEP and DOE.
NCEP-NCAR R1	Reanalysis 1 of the NCEP and NCAR.
NESDIS	National Environmental Satellite, Data, and Information Service (NOAA).
NetCDF	Network Common Data Form.
NH	Northern Hemisphere.
NIST	National Institute of Standards and Technology.
NMC	National Meteorological Center.
NOAA	National Oceanic and Atmospheric Administration.
NOAA-CIRES 20CR v2	20th Century Reanalysis of the NOAA and CIRES, version 2.
NSIDC	National Snow and Ice Data Center.
OI	optimal interpolation.
OISST	NOAA Optimum Interpolation Sea Surface Temperature.
OMI	Ozone Monitoring Instrument.
OSI SAF	Ocean and Sea Ice Satellite Application Facility (EUMETSAT).
OSTIA	Operational Sea Surface Temperature and Sea-Ice Analysis.
OSU LSM	Oregon State University LSM.

PAOBS	Bogus surface pressure data for the Southern Hemisphere produced by the Australian BOM.
PCMDI	Program of Climate Model Diagnosis and Intercomparison.
PDF	probability distribution function.
PIBAL	pilot balloon.
QBO	Quasi-Biennial Oscillation.
QC	quality control.
QuikSCAT	Quick Scatterometer.
R1	see NCEP-NCAR R1.
R2	see NCEP-DOE R2.
RAOBCORE	Radiosonde Observation Correction using Reanalyses.
RCP	representative concentration pathway (IPCC).
RDA	Research Data Archive (NCAR).
RH	relative humidity.
RICH	Radiosonde Innovation Composite Homogenization.
RO	radio occultation.
RRTM	Rapid Radiative Transfer Model developed by AER.
RRTM-G	Rapid Radiative Transfer Model for application to GCMs developed by AER.
RTG	NCEP Real-Time Global SST.
RTTOV	Radiative Transfer for TOVS.
S-RIP	SPARC Reanalysis Intercomparison Project.
SAC-C	Satélite de Aplicaciones Científicas-C (Scientific Application Satellite-C).
SAR	Synthetic Aperture Radar.
satellite era	the period 1979–present, starting from the first full calendar year with TOVS.
SBUV	Solar Backscatter Ultraviolet Radiometer.
SCIAMACHY	SCanning Imaging Absorption spectroMeter for Atmospheric CHartographY.
SEVIRI	Spinning Enhanced Visible and Infrared Imager (EUMETSAT).
SH	Southern Hemisphere.
SHIP	surface meteorological observation report(s) from ships.
SiB	Simple Biosphere model.
SIC	sea ice concentration.
SMMR	Scanning Multichannel Microwave Radiometer.
SNDR	Sounder (for radiance measurements by the GOES 8 to 12).
SNO	Simultaneous Nadir Overpass method.
SOLARIS-HEPPA	Solar Influences for SPARC–High Energy Partical Precipitation in the Atmosphere.
SPARC	Stratosphere-troposphere Processes And their Role in Climate (previously Stratospheric Processes And their Role in Climate).
SSI	Spectral Statistical Interpolation (an assimilation scheme).

SSM/I	(or SSMI) Special Sensor Microwave Imager.
SSMIS	Special Sensor Microwave Imager Sounder.
SST	sea surface temperature.
SSU	Stratospheric Sounding Unit.
STAR	NOAA NESDIS Center for Satellite Applications and Research.
surface input	a class of reanalysis that assimilates only surface data.
SYNOP	Surface meteorological observation report from manned and automated weather stations.
TCWV	total column water vapour.
TD	tape deck ('TD' is a name of a rawinsonde dataset. For example, TD54 is a dataset of mandatory level data from rawinsondes during 1946–1972 prepared by the USAF; see (accessed 29 May 2015).
Terra	a satellite in NASAs EOS program.
TerraSAR-X	a German satellite with a phased array SAR antenna at the X-band wavelength.
TIM	Total Irradiance Monitor.
TIROS	Television InfraRed Observation Satellite.
TIROS-N	Television InfraRed Operational Satellite–Next-generation.
TMI	TRMM Microwave Imager.
TOA	top of atmosphere.
TOMS	Total Ozone Mapping Spectrometer.
TOVS	TIROS Operational Vertical Sounder.
TRMM	Tropical Rainfall Measuring Mission.
TSI	total solar irradiance.
UARS	Upper Atmosphere Research Satellite.
UKMO	United Kingdom Meteorological Office (see also Met Office).
USAF	United States Air Force.
USCNTRL	United States controlled ocean weather stations.
USGS	United States Geological Survey.
UTC	Universal Coordinated Time.
VTPR	Vertical Temperature Profile Radiometer.
WMO	World Meteorological Organization.

Bibliography

Alexander, M. J., Geller, M., McLandress, C., Polavarapu, S., Preusse, P., Sassi, F., Sato, K., Eckermann, S., Ern, M., Hertzog, A., Kawatani, Y., Pulido, M., Shaw, T. A., Sigmond, M., Vincent, R., and Watanabe, S.: Recent developments in gravity-wave effects in climate models and the global distribution of gravity-wave momentum flux from observations and models, Q. J. Roy. Meteor. Soc., 136, 1103–1124, doi: 10.1002/qj.637, 2010.

Allan, P., Brohan, P., Compo, G. P., Stone, R., Luterbacher, J., and Brönnimann, S.: The international Atmospheric Circulation Reconstructions over the Earth (ACRE) initiative, Bull. Am. Meteor. Soc., 92, 1421–1425, doi: 10.1175/2011BAMS3218.1, 2011.

Allen, R. J. and Zender, C. S.: Forcing of the Arctic Oscillation by Eurasian snow cover, J. Climate, 24, 6528–6539, doi: 10.1175/2011JCLI4157.1, 2011.

Anderson, E. and Järvinen, H.: Variational quality control, Q. J. Roy. Meteor. Soc., 125, 697–722, doi: 10.1002/qj.49712555416, 1999.

Andræ, U., Sokka, N., and Onogi, K.: The radiosonde temperature bias corrections used in ERA-40, ERA-40 Project Report Series, No. 15, ECMWF, Shinfield Park, Reading, UK, available at https://www.ecmwf.int/en/elibrary/7773-radiosonde-temperature-bias-corrections-used-era-40 (accessed August 2018), 2004.

Aonashi, K., Kuma, K., and Matsushita, Y.: A physical initialization method for the economical prognostic Arakawa-Schubert scheme, J. Meteorol. Soc. Jpn., 75, 597–618, doi: 10.2151/jmsj1965.75.2_597, 1997.

Arakawa, A.: The cumulus parameterization problem: past, present, and future, J. Climate, 17, 2493–2525, 2004.

Arakawa, A. and Schubert, W. H.: Interaction of a cumulus cloud ensemble with the large-scale environment, part I, J. Atmos. Sci., 31, 674–701, 1974.

Auligné, T., McNally, A. P., and Dee, D. P.: Adaptive bias correction for satellite data in a numerical weather prediction system, Q. J. Roy. Meteor. Soc., 133, 631–642, doi: 10.1002/qj.56, 2007.

Bacmeister, J. T. and Stephens, G. L.: Spatial statistics of likely convective clouds in CloudSat data, J. Geophys. Res. Atmos., 116, D04104, doi: 10.1029/2010JD014444, 2011.

Bacmeister, J. T., Suarez, M. J., and Robertson, F. R.: Rain reevaporation, boundary layer–convection interactions, and Pacific rainfall patterns in an AGCM, J. Atmos. Sci., 63, 3383–3403, doi: 10.1175/JAS3791.1, 2006.

Baines, P. G. and Palmer, T. N.: Rationale for a new physically-based parametrization of subgrid-scale orographic effects, Technical Memorandum 169, ECMWF, Shinfield Park, Reading, UK, available at https://www.ecmwf.int/en/elibrary/7875-rationale-new-physically-based-parametrization-subgrid-scale-orographic-effects (accessed August 2018), 1990.

Ballish, B. A. and Kumar, V. K.: Systematic differences in aircraft and radiosonde temperatures, Bull. Am. Meteor. Soc., 89, 1689–1708, doi: 10.1175/2008BAMS2332.1, 2008.

Balsamo, G., Albergel, C., Beljaars, A., Boussetta, S., Brun, E., Cloke, H., Dee, D., Dutra, E., Muñoz Sabater, J., Pappenberger, F., de Rosnay, P., Stockdale, T., and Vitart, F.: ERA-Interim/Land: a global land surface reanalysis data set, Hydrol. Earth Syst. Sci., 19, 389–407, doi: 10.5194/hess-19-389-2015, 2015.

Bechtold, P., Chaboureau, J.-P., Beljaars, A., Betts, A. K., Köhler, M., Miller, M., and Redelsperger, J.-L.: The simulation of the diurnal cycle of convective precipitation over land in a global model, Q. J. Roy. Meteor. Soc., 130, 3119–3137, doi: 10.1256/qj.03.103, 2006.

Bechtold, P., Semane, N., Lopez, P., Chaboureau, J.-P., Beljaars, A., and Bormann, N.: Representing equilibrium and nonequilibrium convection in large-scale models, J. Atmos. Sci., 71, 734–753, doi: 10.1175/JAS-D-13-0163.1, 2014.

Beljaars, A.: The impact of some aspects of the boundary layer scheme in the ECMWF model, Seminar on Parametrization of Sub-grid Scale Physical Processes, 5–9 September 1994, ECMWF, Shinfield Park, Reading, UK, available at https://www.ecmwf.int/en/elibrary/8035-impact-some-aspects-boundary-layer-scheme-ecmwf-model (accessed August 2018), 1994.

Bengtsson, L., Kanamitsu, M., Kållberg, P., and Uppala, S.: FGGE research activities at ECMWF, Bull. Am. Meteor. Soc., 63, 277–303, 1982.

Birner, T., Sankey, D., and Shepherd, T. G.: The tropopause inversion layer in models and analyses, Geophys. Res. Lett., 33, L14804, doi: 10.1029/2006GL026549, 2006.

Bloom, S. C., Takacs, L. L., da Silva, A. M., and Ledvina, D.: Data assimilation using incremental analysis updates, Mon. Wea. Rev., 124, 1256–1271, 1996.

Bodeker, G. E., Bojinski, S., Cimini, D., Dirksen, R. J., Haeffelin, M., Hannigan, J. W., Hurst, D. F., Leblanc, T., Madonna, F., Maturilli, M., Mikalsen, A. C., Philipona, R., Reale, T., Seidel, D. J., Tan, D. G. H., Thorne, P. W., Vömel, H., and Wang, J.: Reference upper-air observations for climate: from concept to reality, Bull. Am. Meteor. Soc., 97, 123–135, doi: 10.1175/BAMS-D-14-00072.1, 2016.

Boussetta, S., Balsamo, G., Beljaars, A., Kral, T., and Jarlan, L.: Impact of a satellite-derived leaf area index monthly climatology in a global numerical weather prediction model, Int. J. Remote Sens., 34, 3520–3542, doi: 10.1080/01431161.2012.716543, 2013.

Bouttier, F. and Courtier, P.: Data assimilation concepts and methods, Meteorological Training Course Lecture Series, ECMWF, Shinfield Park, Reading, UK, available at https://www.ecmwf.int/en/elibrary/16928-data-assimilation-concepts-and-methods (accessed August 2018), 2002.

Briegleb, B. P.: Delta-Eddington approximation for solar radiation in the NCAR community climate model, J. Geophys. Res. Atmos., 97, 7603–7612, doi: 10.1029/92JD00291, 1992.

Buchard, V., da Silva, A. M., Colarco, P. R., Darmenov, A., Randles, C. A., Govindaraju, R., Torres, O., Campbell, J., and Spurr, R.: Using the OMI aerosol index and absorption aerosol optical depth to evaluate the NASA MERRA Aerosol Reanalysis, Atmos. Chem. Phys., 15, 5743–5760, doi: 10.5194/acp-15-5743-2015, 2015.

Buchard, V., Randles, C. A., da Silva, A. M., Darmenov, A., Colarco, P. R., Govindaraju, R., Ferrare, R., Hair, J., Beyersdorf, A. J., Ziemba, L. D., and Yu, H.: The MERRA-2 Aerosol Reanalysis, 1980 onward. Part II: evaluation and case studies, J. Climate, 30, 6851–6872, doi: 10.1175/JCLI-D-16-0613.1, 2017.

Buehner, M., Houtekamer, P. L., Charette, C., Mitchell, H. L., and He, B.: Intercomparison of variational data assimilation and the ensemble Kalman filter for global deterministic NWP. Part I: description and single-observation experiments, Mon. Wea. Rev., 138, 1550–1566, doi: 10.1175/2009MWR3157.1, 2010a.

Buehner, M., Houtekamer, P. L., Charette, C., Mitchell, H. L., and He, B.: Intercomparison of variational data assimilation and the ensemble Kalman filter for global deterministic NWP. Part II: one-month experiments with real observations, Mon. Wea. Rev., 138, 1567–1586, doi: 10.1175/2009MWR3158.1, 2010b.

Buizza, R., Brnnimann, S., Haimberger, L., Laloyaux, P., Martin, M. J., Fuentes, M., Alonso-Balmaseda, M., Becker, A., Blaschek, M., Dahlgren, P., de Boisseson, E., Dee, D., Doutriaux-Boucher, M., Feng, X., John, V. O., Haines, K., Jourdain, S., Kosaka, Y., Lea, D., Lemari, F., Mayer, M., Messina, P., Perruche, C., Peylin, P., Pullainen, J., Rayner, N., Rustemeier, E., Schepers, D., Saunders, R., Schulz, J., Sterin, A., Stichelberger, S., Storto, A., Testut, C.-E., Valente, M.-A., Vidard, A., Vuichard, N., Weaver, A., While, J., and Ziese, M.: The EU-FP7 ERA-CLIM2 project contribution to advancing science and production of Earth system climate reanalyses, Bull. Am. Meteor. Soc., 99, 1003–1014, doi: 10.1175/BAMS-D-17-0199.1, 2018.

Campbell, W. F., Bishop, C. H., and Hodyss, D.: Vertical covariance localization for satellite radiances in ensemble Kalman filters, Mon. Wea. Rev., 138, 282–290, doi: 10.1175/2009MWR3017.1, 2010.

Cariolle, D. and Déqué, M.: Southern hemisphere medium-scale waves and total ozone disturbances in a spectral general circulation model, J. Geophys. Res. Atmos., 91, 10 825–10 846, doi: 10.1029/JD091iD10p10825, 1986.

Cariolle, D. and Teyssèdre, H.: A revised linear ozone photochemistry parameterization for use in transport and general circulation models: multi-annual simulations, Atmos. Chem. Phys., 7, 2183–2196, doi: 10.5194/acp-7-2183-2007, 2007.

Charnock, H.: Wind stress on a water surface, Q. J. Roy. Meteor. Soc., 81, 639–640, doi: 10.1002/qj.49708135027, 1955.

Chou, M.-D. and Lee, K.-T.: Parameterizations for the absorption of solar radiation by water vapor and ozone, J. Atmos. Sci., 53, 1203–1208, 1996.

Chou, M.-D. and Suarez, M.: A solar radiation parameterization for atmospheric studies, Technical Report Series on Global Modeling and Data Assimilation, No. 15, NASA/TM-1999-104606, Greenbelt, Maryland, available at https://ntrs.nasa.gov/search.jsp?R=19990060930 (accessed August 2018), 1999.

Chou, M.-D., Suarez, M., Liang, X.-Z., and Yan, M. M.-H.: A thermal infrared radiation parameterization for atmospheric studies, Technical Report Series on Global Modeling and Data Assimilation, No. 19, NASA/TM-2001-104606, Greenbelt, Maryland, available at https://ntrs.nasa.gov/search.jsp?R=20010072848 (accessed August 2018), 2001.

Chun, H.-Y. and Baik, J.-J.: Momentum flux by thermally induced internal gravity waves and its approximation for large-scale models, J. Atmos. Sci., 55, 3299–3310, 1998.

Cionni, I., Eyring, V., Lamarque, J. F., Randel, W. J., Stevenson, D. S., Wu, F., Bodeker, G. E., Shepherd, T. G., Shindell, D. T., and Waugh, D. W.: Ozone database in support of CMIP5 simulations: results and corresponding radiative forcing, Atmos. Chem. Phys., 11, 11 267–11 292, doi: 10.5194/acp-11-11267-2011, 2011.

Clough, S., Shephard, M., Mlawer, E., Delamere, J., Iacono, M., Cady-Pereira, K., Boukabara, S., and Brown, P.: Atmospheric radiative transfer modeling: a summary of the AER codes, J. Quant. Spectrosc. Radiat. Transfer, 91, 233–244, doi: 10.1016/j.jqsrt.2004.05.058, 2005.

Cohen, J. and Entekhabi, D.: Eurasian snow cover variability and Northern Hemisphere climate predictability, Geophys. Res. Lett., 26, 345–348, doi: 10.1029/1998GL900321, 1999.

Cohen, J., Furtado, J. C., Jones, J., Barlow, M., Whittleston, D., and Entekhabi, D.: Linking Siberian snow cover to precursors of stratospheric variability, J. Climate, 27, 5422–5432, doi: 10.1175/JCLI-D-13-00779.1, 2014.

Colarco, P., da Silva, A., Chin, M., and Diehl, T.: Online simulations of global aerosol distributions in the NASA GEOS-4 model and comparisons to satellite and ground-based aerosol optical depth, J. Geophys. Res. Atmos., 115, D14207, doi: 10.1029/2009JD012820, 2010.

Collins, W. D.: Parameterization of generalized cloud overlap for radiative calculations in general circulation models, J. Atmos. Sci., 58, 3224–3242, 2001.

Collow, A. B. M., Mahanama, S. P., Bosilovich, M. G., Koster, R. D., and Schubert, S. D.: An evaluation of teleconnections over the United States in an ensemble of AMIP simulations with the MERRA-2 configuration of the GEOS atmospheric model, Technical Report Series on Global Modeling and Data Assimilation, No. 47, NASA/TM-2017-104606, Greenbelt, Maryland, available at https://ntrs.nasa.gov/search.jsp?R=20180001607 (accessed November 2018), 2017.

Compo, G. P., Whitaker, J. S., Sardeshmukh, P. D., Matsui, N., Allan, R. J., Yin, X., Gleason, B. E., Vose, R. S., Rutledge, G., Bessemoulin, P., Brnnimann, S., Brunet, M., Crouthamel, R. I., Grant, A. N., Groisman, P. Y., Jones, P. D., Kruk, M. C., Kruger, A. C., Marshall, G. J.,

Maugeri, M., Mok, H. Y., Nordli, ., Ross, T. F., Trigo, R. M., Wang, X. L., Woodruff, S. D., and Worley, S. J.: The Twentieth Century Reanalysis Project, Q. J. Roy. Meteor. Soc., 137, 1–28, doi: 10.1002/qj.776, 2011.

Courtier, P., Thépaut, J.-N., and Naughton, M.: A strategy for operational implementation of 4D-Var, using an incremental approach, Q. J. Roy. Meteor. Soc., 120, 1367–1387, doi: 10.1002/qj.49712051912, 1994.

Coy, L., Wargan, K., Molod, A. M., McCarty, W. R., and Pawson, S.: Structure and dynamics of the Quasi-Biennial Oscillation in MERRA-2, J. Climate, 29, 5339–5354, doi: 10.1175/JCLI-D-15-0809.1, 2016.

Cram, T. A., Compo, G. P., Yin, X., Allan, R. J., McColl, C., Vose, R. S., Whitaker, J. S., Matsui, N., Ashcroft, L., Auchmann, R., Bessemoulin, P., Brandsma, T., Brohan, P., Brunet, M., Comeaux, J., Crouthamel, R., Gleason, B. E., Groisman, P. Y., Hersbach, H., Jones, P. D., Jònsson, T., Jourdain, S., Kelly, G., Knapp, K. R., Kruger, A., Kubota, H., Lentini, G., Lorrey, A., Lott, N., Lubker, S. J., Luterbacher, J., Marshall, G. J., Maugeri, M., Mock, C. J., Mok, H. Y., Nordli, Ø., Rodwell, M. J., Ross, T. F., Schuster, D., Srnec, L., Valente, M. A., Vizi, Z., Wang, X. L., Westcott, N., Woollen, J. S., and Worley, S. J.: The International Surface Pressure Databank version 2, Geosci. Data J., 2, 31–46, doi: 10.1002/gdj3.25, 2015.

Cressman, G. P.: An operational objective analysis system, Mon. Wea. Rev., 87, 367–374, 1959.

Daley, R.: Normal mode initialization, Rev. Geophys., 19, 450–468, doi: 10.1029/RG019i003p00450, 1981.

de Rosnay, P., Balsamo, G., Albergel, C., Muñoz-Sabater, J., and Isaksen, L.: Initialisation of land surface variables for numerical weather prediction, Surv. Geophys., 35, 607–621, doi: 10.1007/s10712-012-9207-x, 2014.

de Rosnay, P., Isaksen, L., and Dahoui, L.: Snow data assimilation at ECMWF, ECMWF Newsletter No. 143, Spring 2015, available at https://www.ecmwf.int/en/elibrary/17328-snow-data-assimilation-ecmwf (accessed September 2018), 2015.

Dee, D. P.: Bias and data assimilation, Q. J. Roy. Meteor. Soc., 131, 3323–3343, doi: 10.1256/qj.05.137, 2005.

Dee, D. P., Uppala, S. M., Simmons, A. J., Berrisford, P., Poli, P., Kobayashi, S., Andrae, U., Balmaseda, M. A., Balsamo, G., Bauer, P., Bechtold, P., Beljaars, A. C. M., van de Berg, L., Bidlot, J., Bormann, N., Delsol, C., Dragani, R., Fuentes, M., Geer, A. J., Haimberger, L., Healy, S. B., Hersbach, H., Hlm, E. V., Isaksen, L., Kllberg, P., Khler, M., Matricardi, M., McNally, A. P., Monge-Sanz, B. M., Morcrette, J.-J., Park, B.-K., Peubey, C., de Rosnay, P., Tavolato, C., Thpaut, J.-N., and Vitart, F.: The ERA-Interim reanalysis: configuration and performance of the data assimilation system, Q. J. Roy. Meteor. Soc., 137, 553–597, doi: 10.1002/qj.828, 2011.

Derber, J. C. and Wu, W.-S.: The use of TOVS cloud-cleared radiances in the NCEP SSI analysis system, Mon. Wea. Rev., 126, 2287–2299, 1998.

Dethof, A. and Hólm, E. V.: Ozone assimilation in the ERA-40 reanalysis project, Q. J. Roy. Meteor. Soc., 130, 2851–2872, doi: 10.1256/qj.03.196, 2004.

Donlon, C., Martin, M. J., Stark, J., Roberts-Jones, J., Fiedler, E., and Wimmer, W.: The Operational Sea Surface Temperature and Sea Ice Analysis (OSTIA) system, Remote Sens. Environ., 116, 140–158, doi: 10.1016/j.rse.2010.10.017, 2012.

Dorman, J. L. and Sellers, P. J.: A global climatology of albedo, roughness length and stomatal resistance for atmospheric general circulation models as represented by the Simple Biosphere Model (SiB), J. Appl. Meteorol., 28, 833–855, 1989.

Dragani, R.: On the quality of the ERA-Interim ozone reanalyses: comparisons with satellite data, Q. J. Roy. Meteor. Soc., 137, 1312–1326, doi: 10.1002/qj.821, 2011.

Dutra, E., Balsamo, G., Viterbo, P., Miranda, P. M. A., Beljaars, A., Schr, C., and Elder, K.: An improved snow scheme for the ECMWF land surface model: description and offline validation, J. Hydrometeorol., 11, 899–916, doi: 10.1175/2010JHM1249.1, 2010.

Ebita, A., Kobayashi, S., Ota, Y., Moriya, M., Kumabe, R., Onogi, K., Harada, Y., Yasui, S., Miyaoka, K., Takahashi, K., Kamahori, H., Kobayashi, C., Endo, H., Soma, M., Oikawa, Y., and Ishimizu, T.: The Japanese 55-year Reanalysis "JRA-55": an interim report, SOLA, 7, 149–152, doi: 10.2151/sola.2011-038, 2011.

Ek, M. B., Mitchell, K. E., Lin, Y., Rogers, E., Grunmann, P., Koren, V., Gayno, G., and Tarpley, J. D.: Implementation of Noah land surface model advances in the National Centers for Environmental Prediction operational mesoscale Eta model, J. Geophys. Res. Atmos., 108, 8851, doi: 10.1029/2002JD003296, 2003.

Evensen, G.: Data Assimilation: The Ensemble Kalman Filter, Springer–Verlag, Berlin, doi: 10.1007/978-3-642-03711-5, 307 pp., 2009.

Evensen, G. and van Leeuwen, P. J.: An ensemble Kalman smoother for nonlinear dynamics, Mon. Wea. Rev., 128, 1852–1867, 2000.

Fels, S. B. and Schwarzkopf, M. D.: The simplified exchange approximation: a new method for radiative transfer calculations, J. Atmos. Sci., 32, 1475–1488, 1975.

Flannaghan, T. J. and Fueglistaler, S.: Vertical mixing and the temperature and wind structure of the tropical tropopause layer, J. Atmos. Sci., 71, 1609–1622, doi: 10.1175/JAS-D-13-0321.1, 2014.

Flemming, J., Benedetti, A., Inness, A., Engelen, R. J., Jones, L., Huijnen, V., Remy, S., Parrington, M., Suttie, M., Bozzo, A., Peuch, V.-H., Akritidis, D., and Katragkou, E.: The CAMS interim Reanalysis of carbon monoxide, ozone and aerosol for 2003–2015, Atmos. Chem. Phys., 17, 1945–1983, doi: 10.5194/acp-17-1945-2017, 2017.

Forbes, R., Tompkins, A. M., and Untch, A.: A new prognostic bulk microphysics scheme for the IFS, ECMWF Technical Memorandum, No. 649, ECMWF,

, available at https://www.ecmwf.int/en/elibrary/9441-new-prognostic-bulk-microphysics-scheme-ifs (accessed August 2018), 2011.

Fortuin, J. P. and Langematz, U.: An update on the current ozone climatology and on concurrent ozone and temperature trends, Proc. SPIE, 2311, 207–216, doi: 10.1117/12.198578, 1995.

Fouquart, Y. and Bonnel, B.: Computation of solar heating of the Earths atmosphere: a new parameterization, Beitr. Phys., 53, 35–62, 1980.

Freidenreich, S. M. and Ramaswamy, V.: Solar radiation absorption by CO_2, overlap with H_2O, and a parameterization for general circulation models, J. Geophys. Res. Atmos., 98, 7255–7264, doi: 10.1029/92JD02887, 1993.

Freidenreich, S. M. and Ramaswamy, V.: A new multiple-band solar radiative parameterization for general circulation models, J. Geophys. Res. Atmos., 104, 31 389–31 409, doi: 10.1029/1999JD900456, 1999.

Fujiwara, M., Wright, J. S., Manney, G. L., Gray, L. J., Anstey, J., Birner, T., Davis, S., Gerber, E. P., Harvey, V. L., Hegglin, M. I., Homeyer, C. R., Knox, J. A., Krüger, K., Lambert, A., Long, C. S., Martineau, P., Molod, A., Monge-Sanz, B. M., Santee, M. L., Tegtmeier, S., Chabrillat, S., Tan, D. G. H., Jackson, D. R., Polavarapu, S., Compo, G. P., Dragani, R., Ebisuzaki, W., Harada, Y., Kobayashi, C., McCarty, W., Onogi, K., Pawson, S., Simmons, A., Wargan, K., Whitaker, J. S., and Zou, C.-Z.: Introduction to the SPARC Reanalysis Intercomparison Project (S-RIP) and overview of the reanalysis systems, Atmos. Chem. Phys., 17, 1417–1452, doi: 10.5194/acp-17-1417-2017, 2017.

Gandin, L. S.: Objective analysis of meteorological fields, *Gidrometerologischeskoe Izdatelstvo*, Leningrad, translated (1965) by the Israel Program for Scientific Translations, Jerusalem, 1963.

Garcia, R. R. and Boville, B. A.: Downward control of the mean meridional circulation and temperature distribution of the polar winter stratosphere, J. Atmos. Sci., 51, 2238–2245, 1994.

Gelaro, R., McCarty, W., Surez, M. J., Todling, R., Molod, A., Takacs, L., Randles, C. A., Darmenov, A., Bosilovich, M. G., Reichle, R., Wargan, K., Coy, L., Cullather, R., Draper, C., Akella, S., Buchard, V., Conaty, A., da Silva, A. M., Gu, W., Kim, G.-K., Koster, R., Lucchesi, R., Merkova, D., Nielsen, J. E., Partyka, G., Pawson, S., Putman, W., Rienecker, M., Schubert, S. D., Sienkiewicz, M., and Zhao, B.: The Modern-Era Retrospective Analysis for Research and Applications, Version 2 (MERRA-2), J. Climate, 30, 5419–5454, doi: 10.1175/JCLI-D-16-0758.1, 2017.

Gettelman, A., Hegglin, M. I., Son, S.-W., Kim, J., Fujiwara, M., Birner, T., Kremser, S., Rex, M., Añel, J. A., Akiyoshi, H., Austin, J., Bekki, S., Braesike, P., Brühl, C., Butchart, N., Chipperfield, M., Dameris, M., Dhomse, S., Garny, H., Hardiman, S. C., Jöckel, P., Kinnison, D. E., Lamarque, J. F., Mancini, E., Marchand, M., Michou, M., Morgenstern, O., Pawson, S., Pitari, G., Plummer, D., Pyle, J. A., Rozanov, E., Scinocca, J., Shepherd, T. G., Shibata, K., Smale, D., Teyssèdre, H., and Tian, W.: Multimodel assessment of the upper troposphere and lower stratosphere: Tropics and global trends, J. Geophys. Res. Atmos., 115, D00M08, doi: 10.1029/2009JD013638, 2010.

Gibson, J. K., Kållberg, P., Uppala, S. M., Nomura, A., Hernandez, A., and Serrano, E.: ERA description, ERA-15 Report Series, No. 1, ECMWF, Shinfield Park, Reading, UK, available at https://www.ecmwf.int/en/elibrary/9584-era-description (accessed August 2018), 1997.

Goldberg, M., Ohring, G., Butler, J., Cao, C., Datla, R., Doelling, D., Gärtner, V., Hewison, T., Iacovazzi, B., Kim, D., Kurino, T., Lafeuille, J., Minnis, P., Renaut, D., Schmetz, J., Tobin, D., Wang, L., Weng, F., Wu, X., Yu, F., Zhang, P., and Zhu, T.: The Global Space-Based Inter-Calibration System, Bull. Am. Meteor. Soc., 92, 467–475, doi: 10.1175/2010BAMS2967.1, 2011.

Goody, R. M.: A statistical model for water-vapour absorption, Q. J. Roy. Meteor. Soc., 78, 165–169, doi: 10.1002/qj.49707833604, 1952.

Gregory, D. and Rowntree, P. R.: A mass flux convection scheme with representation of cloud ensemble characteristics and stability-dependent closure, Mon. Wea. Rev., 118, 1483–1506, 2000.

Gustafsson, N.: Discussion on "4D-Var or EnKF?", Tellus A, 59, 774–777, doi: 10.1111/j.1600-0870.2007.00262.x, 2007.

Haimberger, L., Tavolato, C., and Sperka, S.: Toward elimination of the warm bias in historic radiosonde temperature records — some new results from a comprehensive intercomparison of upper-air data, J. Climate, 21, 4587–4606, doi: 10.1175/2008JCLI1929.1, 2008.

Haimberger, L., Tavolato, C., and Sperka, S.: Homogenization of the global radiosonde temperature dataset through combined comparison with reanalysis background series and neighboring stations, J. Climate, 25, 8108–8131, doi: 10.1175/JCLI-D-11-00668.1, 2012.

Harada, Y., Kamahori, H., Kobayashi, C., Endo, H., Kobayashi, S., Ota, Y., Onoda, H., Onogi, K., Miyaoka, K., and Takahashi, K.: The JRA-55 Reanalysis: Representation of atmospheric circulation and climate variability, J. Meteorol. Soc. Jpn., 94, 269–302, doi: 10.2151/jmsj.2016-015, 2016.

Helfand, H. M. and Schubert, S. D.: Climatology of the simulated Great Plains low-level jet and its contribution to the continental moisture budget of the United States, J. Climate, 8, 784–806, 1995.

Helfand, H. M., Jusem, J. C., Pfaendtner, J., Tenenbaum, J., and Kalnay, E.: The effect of a gravity wave drag parameterization scheme on GLA fourth-order GCM forecasts, Collection of papers presented at the WMO/IUGG NWP Symposium, Tokyo, 4–8 August 1986, available at https://ntrs.nasa.gov/search.jsp?R=19880050777 (accessed August 2018), 1987.

Hering, W. S. and Borden, Jr., T. R.: Mean distributions of ozone density over North America, 1963–1964, Tech. Rep. AFCRL-65-913, Air Force Cambridge Research Laboratories, 1965.

Hersbach, H. and Dee, D.: ERA5 reanalysis is in production, ECMWF Newsletter No. 147, Spring 2016, available at https://www.ecmwf.int/en/newsletter/147/news/era5-reanalysis-production (accessed August 2018), 2016.

Hersbach, H., Peubey, C., Simmons, A., Berrisford, P., Poli, P., and Dee, D.: ERA-20CM: a twentieth-century atmospheric model ensemble, Q. J. Roy. Meteor. Soc., 141, 2350–2375, doi: 10.1002/qj.2528, 2015.

Holton, J. R. and Wehrbein, W. M.: A numerical model of the zonal mean circulation of the middle atmosphere, Pure Appl. Geophys., 118, 284–306, doi: 10.1007/BF01586455, 1980.

Hong, S.-Y. and Pan, H.-L.: Nonlocal boundary layer vertical diffusion in a medium-range forecast model, Mon. Wea. Rev., 124, 2322–2339, 1996.

Hong, S.-Y. and Pan, H.-L.: Convective trigger function for a mass-flux cumulus parameterization scheme, Mon. Wea. Rev., 126, 2599–2620, 1998.

Hortal, M. and Simmons, A. J.: Use of reduced Gaussian grids in spectral models, Mon. Wea. Rev., 119, 1057–1074, 1991.

Iacono, M. J., Delamere, J. S., Mlawer, E. J., Shephard, M. W., Clough, S. A., and Collins, W. D.: Radiative forcing by long-lived greenhouse gases: Calculations with the AER radiative transfer models, J. Geophys. Res. Atmos., 113, D13103, doi: 10.1029/2008JD009944, 2008.

Ingleby, N. B., Lorenc, A. C., Ngan, K., Rawlins, F., and Jackson, D. R.: Improved variational analyses using a nonlinear humidity control variable, Q. J. Roy. Meteor. Soc., 139, 1875–1887, doi: 10.1002/qj.2073, 2013.

IPCC: Climate Change 1995: The Science of Climate Change. Contribution of Working Group I to the Second Assessment Report of the Intergovernmental Panel on Climate Change, Houghton, J.T., L.G. Meira Filho, B.A. Callander, N. Harris, A. Kattenberg, and K. Maskell (eds.), Cambridge University Press, Cambridge, United Kingdom and New York, NY, USA, 572 pp., available at https://www.ipcc.ch/publications_and_data/publications_and_data_reports.shtml (accessed August 2018), 1996.

Ishii, M., Shouji, A., Sugimoto, S., and Matsumoto, T.: Objective analyses of sea-surface temperature and marine meteorological variables for the 20th century using ICOADS and the Kobe Collection, Int. J. Climatol., 25, 865–879, doi: 10.1002/joc.1169, 2005.

Iwasaki, T., Yamada, S., and Tada, K.: A parameterization scheme of orographic gravity wave drag with two different vertical partitionings, part I: impact on medium-range forecasts, J. Meteorol. Soc. Jpn., 67, 11–27, doi: 10.2151/jmsj1965.67.1_11, 1989a.

Iwasaki, T., Yamada, S., and Tada, K.: A parameterization scheme of orographic gravity wave drag with two different vertical partitionings, part II: zonally averaged budget analyses based on transformed Eulerian-mean method, J. Meteorol. Soc. Jpn., 67, 29–41, doi: 10.2151/jmsj1965.67.1_29, 1989b.

Janssen, P. A. E. M., Doyle, J., Bidlot, J.-R., Hansen, B., Isaksen, L., and Viterbo, P.: Impact and feedback of ocean waves on the atmosphere, Technical Memorandum 341, ECMWF, Shinfield Park, Reading, UK, available at https://www.ecmwf.int/en/elibrary/10225-impact-and-feedback-ocean-waves-atmosphere (accessed August 2018), 2001.

Jiang, J. H., Su, H., Pawson, S., Liu, H.-C., Read, W. G., Waters, J. W., Santee, M. L., Wu, D. L., Schwartz, M. J., Livesey, N. J., Lambert, A., Fuller, R. A., and Lee, J. N.: Five year (2004–2009) observations of upper tropospheric water vapor and cloud ice from MLS and comparisons with GEOS-5 analyses, J. Geophys. Res. Atmos., 115, D15103, doi: 10.1029/2009JD013256, 2010.

JMA: Outline of the operational numerical weather prediction at the Japan Meteorological Agency, appendix to WMO Technical Progress Report on the Global Data-Processing and Forecasting System and Numerical Weather Prediction, Japan Meteorological Agency, Tokyo, available at http://www.jma.go.jp/jma/jma-eng/jma-center/nwp/outline-nwp/index.htm (accessed August 2018), 2007.

JMA: Outline of the operational numerical weather prediction at the Japan Meteorological Agency, appendix to WMO Technical Progress Report on the Global Data-Processing and Forecasting System and Numerical Weather Prediction, Japan Meteorological Agency, Tokyo, available at http://www.jma.go.jp/jma/jma-eng/jma-center/nwp/outline2013-nwp/index.htm (accessed August 2018), 2013.

Kalman, R. E.: A new approach to linear filtering and prediction problems, J. Basic Eng., 82, 35–45, 1960.

Kalnay, E.: Atmospheric Modeling, Data Assimilation, and Predictability, Cambridge University Press, Cambridge, 341 pp., 2003.

Kalnay, E., Kanamitsu, M., Kistler, R., Collins, W., Deaven, D., Gandin, L., Iredell, M., Saha, S., White, G., Woollen, J., Zhu, Y., Chelliah, M., Ebisuzaki, W., Higgins, W., Janowiak, J., Mo, K. C., Ropelewski, C., Wang, J., Leetmaa, A., Reynolds, R., Jenne, R., and Joseph, D.: The NCEP/NCAR 40-Year reanalysis project, Bull. Am. Meteor. Soc., 77, 437–472, 1996.

Kalnay, E., Li, H., Miyoshi, T., Yang, S.-C., and Ballabrera-Poy, J.: 4-D-Var or ensemble Kalman filter?, Tellus A, 59, 758–773, doi: 10.1111/j.1600-0870.2007.00261.x, 2007a.

Kalnay, E., Li, H., Miyoshi, T., Yang, S.-C., and Ballabrera-Poy, J.: Response to the discussion on “4-D-Var or EnKF?” by Nils Gustafsson, Tellus A, 59, 778–780, doi: 10.1111/j.1600-0870.2007.00263.x, 2007b.

Kanamitsu, M., Ebisuzaki, W., Woollen, J., Yang, S.-K., Hnilo, J. J., Fiorino, M., and Potter, G. L.: NCEPDOE AMIP-II Reanalysis (R-2), Bull. Am. Meteor. Soc., 83, 1631–1644, doi: 10.1175/BAMS-83-11-1631, 2002.

Kawai, H. and Inoue, T.: A simple parameterization scheme for subtropical marine stratocumulus, SOLA, 2, 17–20, doi: 10.2151/sola.2006-005, 2006.

Kim, Y.-J. and Arakawa, A.: Improvement of orographic gravity wave parameterization using a mesoscale gravity wave model, J. Atmos. Sci., 52, 1875–1902, 1995.

Kistler, R., Kalnay, E., Collins, W., Saha, S., White, G., Woollen, J., Chelliah, M., Ebisuzaki, W., Kanamitsu, M., Kousky, V., van den Dool, H., Jenne, R., and Fiorino, M.: The NCEP–NCAR 50-Year Reanalysis: monthly means CD-ROM and documentation, Bull. Am. Meteor. Soc., 82, 247–268, 2001.

Kobayashi, C., Endo, H., Ota, Y., Kobayashi, S., Onoda, H., Harada, Y., Onogi, K., and Kamahori, H.: Preliminary results of the JRA-55C, an atmospheric reanalysis assimilating conventional observations only, SOLA, 10, 78–82, doi: 10.2151/sola.2014-016, 2014.

Kobayashi, S., Ota, Y., Harada, Y., Ebita, A., Moriya, M., Onoda, H., Onogi, K., Kamahori, H., Kobayashi, C., Endo, H., Miyaoka, K., and Takahashi, K.: The JRA-55 Reanalysis: General specifications and basic characteristics, J. Meteorol. Soc. Jpn., 93, 5–48, doi: 10.2151/jmsj.2015-001, 2015.

Koepke, P., Hess, M., Schult, I., and Shettle, E. P.: Global Aerosol Data Set, Report No. 243, Max-Planck-Institut für Meteorologie, Hamburg, 44 pp., available at http://opac.userweb.mwn.de/radaer/gads.html (accessed August 2018), 1997.

Köhler, M., Ahlgrimm, M., and Beljaars, A.: Unified treatment of dry convective and stratocumulus-topped boundary layers in the ECMWF model, Q. J. Roy. Meteor. Soc., 137, 43–57, doi: 10.1002/qj.713, 2011.

Komen, G. J., Cavaleri, L., Donelan, M., Hasselman, K., Hasselman, S., and Janssen, P. A. E. M.: Dynamics and Modelling of Ocean Waves, Cambridge University Press, Cambridge, 532 pp., 1994.

Kondo, J.: Air-sea bulk transfer coefficients in diabatic conditions, Bound.-Lay. Meteorol., 9, 91–112, doi: 10.1007/BF00232256, 1975.

Koren, V., Schaake, J., Mitchell, K., Duan, Q.-Y., Chen, F., and Baker, J. M.: A parameterization of snowpack and frozen ground intended for NCEP weather and climate models, J. Geophys. Res. Atmos., 104, 19 569–19 585, doi: 10.1029/1999JD900232, 1999.

Koster, R. D., Suarez, M. J., Ducharne, A., Stieglitz, M., and Kumar, P.: A catchment-based approach to modeling land surface processes in a general circulation model: 1. Model structure, J. Geophys. Res. Atmos., 105, 24 809–24 822, doi: 10.1029/2000JD900327, 2000.

Krishnamurti, T. N. and Bounoua, L.: An Introduction to Numerical Weather Prediction Techniques, CRC Press, Florida, USA, 293 pp., 1996.

Lacis, A. A. and Hansen, J.: A parameterization for the absorption of solar radiation in the Earth's atmosphere, J. Atmos. Sci., 31, 118–133, 1974.

Laloyaux, P., Balmaseda, M., Dee, D., Mogensen, K., and Janssen, P.: A coupled data assimilation system for climate reanalysis, Q. J. Roy. Meteor. Soc., 142, 65–78, doi: 10.1002/qj.2629, 2016.

Lamarque, J.-F., Bond, T. C., Eyring, V., Granier, C., Heil, A., Klimont, Z., Lee, D., Liousse, C., Mieville, A., Owen, B., Schultz, M. G., Shindell, D., Smith, S. J., Stehfest, E., Van Aardenne, J., Cooper, O. R., Kainuma, M., Mahowald, N., McConnell, J. R., Naik, V., Riahi, K., and van Vuuren, D. P.: Historical (1850–2000) gridded anthropogenic and biomass burning emissions of reactive gases and aerosols: methodology and application, Atmos. Chem. Phys., 10, 7017–7039, doi: 10.5194/acp-10-7017-2010, 2010.

Large, W. G. and Pond, S.: Open ocean momentum flux measurements in moderate to strong winds, J. Phys. Oceanogr., 11, 324–336, 1981.

Lawless, A. S.: A note on the analysis error associated with 3D-FGAT, Q. J. Roy. Meteor. Soc., 136, 1094–1098, doi: 10.1002/qj.619, 2010.

Lawrence, Z. D., Manney, G. L., Minschwaner, K., Santee, M. L., and Lambert, A.: Comparisons of polar processing diagnostics from 34 years of the ERA-Interim and MERRA reanalyses, Atmos. Chem. Phys., 15, 3873–3892, doi: 10.5194/acp-15-3873-2015, 2015.

Lin, S.-J.: A "vertically Lagrangian" finite-volume dynamical core for global models, Mon. Wea. Rev., 132, 2293–2307, 2004.

Lindzen, R. S. and Holton, J. R.: A theory of the Quasi-Biennial Oscillation, J. Atmos. Sci., 25, 1095–1107, 1968.

Lindzen, R. S., Batten, E. S., and Kim, J.-W.: Oscillations in atmospheres with tops, Mon. Wea. Rev., 96, 133–140, 1968.

Liu, Q., Marchok, T., Pan, H., Bender, M., and Lord, S.: Improvements in hurricane initialization and forecasting at NCEP with global and regional (GFDL) models, Technical Procedures Bulletin, No. 472, NOAA National Weather Service, Silver Spring, MD, 1999.

Lock, A. P., Brown, A. R., Bush, M. R., Martin, G. M., and Smith, R. N. B.: A new boundary layer mixing scheme. Part I: scheme description and single-column model tests, Mon. Wea. Rev., 128, 3187–3199, 2000.

London, J.: Mesospheric dynamics, part III. The distribution of total ozone in the Northern Hemisphere, Final Report, Dept. of Meteorology and Oceanography, New York University, 99 pp., 1962.

Lorenc, A. C. and Rawlins, F.: Why does 4D-Var beat 3D-Var?, Q. J. Roy. Meteor. Soc., 131, 3247–3257, doi: 10.1256/qj.05.85, 2005.

Lott, F. and Miller, M. J.: A new subgrid-scale orographic drag parametrization: its formulation and testing, Q. J. Roy. Meteor. Soc., 123, 101–127, doi: 10.1002/qj.49712353704, 1997.

Louis, J.-F.: A parametric model of vertical eddy fluxes in the atmosphere, Bound.-Lay. Meteorol., 17, 187–202, doi: 10.1007/BF00117978, 1979.

Louis, J.-F., Tiedtke, M., and Geleyn, J.-F.: A short history of the PBL parameterization at ECMWF, Workshop on Planetary Boundary Layer Parameterization, 25-27 November 1981, Shinfield Park, Reading, UK, available at https://www.ecmwf.int/en/elibrary/10845-short-history-pbl-parameterization-ecmwf (accessed August 2018), 1982.

Lynch, P.: Digital filters for numerical weather prediction, HIRLAM Technical Reports, No. 10, 55 pp., available at http://hirlam.org/index.php/publications-54/hirlam-technical-reports-a/doc_download/1563-hirlam-technical-report-no-10-digital-filters-for-numerical-weather-prediction (accessed August 2018), 1993.

Lynch, P. and Huang, X.-Y.: Initialization of the HIRLAM model Using a digital filter, Mon. Wea. Rev., 120, 1019–1034, 1992.

Machenhauer, B.: On the dynamics of gravity oscillations in a shallow water model with applications to normal mode initialization, Contrib. Atmos. Phys., 50, 253–271, 1977.

Machenhauer, B.: The spectral method, in: Numerical Methods used in Atmospheric Models, vol. II, *GARP Publication Series*, vol. 17, pp. 121–275, World Meteorological Organization, Geneva, 1979.

Mahfouf, J.-F., Manzi, A. O., Noilhan, J., Giordani, H., and DéQué, M.: The land surface scheme ISBA within the Météo-France climate model ARPEGE. Part I. Implementation and preliminary results, J. Climate, 8, 2039–2057, 1995.

Mahrt, L. and Pan, H.: A two-layer model of soil hydrology, Bound.-Lay. Meteorol., 29, 1–20, doi: 10.1007/BF00119116, 1984.

Martineau, P.: S-RIP: Zonal-mean dynamical variables of global atmospheric reanalyses on pressure levels, doi: 10.5285/b241a7f536a244749662360bd7839312, URL http://catalogue.ceda.ac.uk/uuid/b241a7f536a244749662360bd7839312, 2017.

Martineau, P., Wright, J. S., Zhu, N., and Fujiwara, M.: Zonal-mean data set of global atmospheric reanalyses on pressure levels, Earth Syst. Sci. Data Disc., doi: 10.5194/essd-2018-71, 2018.

Matsumoto, T., Ishii, M., Fukuda, Y., and Hirahara, S.: Sea ice data derived from microwave radiometer for climate monitoring, Proceedings of the 14th Conference on Satellite Meteorology and Oceanography, Atlanta, USA, p2.21, 2006.

McCarty, W., Coy, L., Gelaro, R., Merkova, D., Smith, E. B., Sienkiewicz, M., and Wargan, K.: MERRA-2 input observations: Summary and assessment, Technical Report Series on Global Modeling and Data Assimilation, No. 46, NASA/TM-2016-104606, Greenbelt, Maryland, 64 pp., available at https://ntrs.nasa.gov/search.jsp?R=20160014544 (accessed August 2018), 2016.

McCormack, J. P., Eckermann, S. D., Siskind, D. E., and McGee, T. J.: CHEM2D-OPP: A new linearized gas-phase ozone photochemistry parameterization for high-altitude NWP and climate models, Atmos. Chem. Phys., 6, 4943–4972, doi: 10.5194/acp-6-4943-2006, 2006.

McFarlane, N. A.: The effect of orographically excited gravity wave drag on the general circulation of the lower stratosphere and troposphere, J. Atmos. Sci., 44, 1775–1800, 1987.

Meinshausen, M., Smith, S. J., Calvin, K., Daniel, J. S., Kainuma, M. L. T., Lamarque, J.-F., Matsumoto, K., Montzka, S. A., Raper, S. C. B., Riahi, K., Thomson, A., Velders, G. J. M., and van Vuuren, D. P.: The RCP greenhouse gas concentrations and their extensions from 1765 to 2300, Clim. Change, 109, 213, doi: 10.1007/s10584-011-0156-z, 2011.

Mellor, G. L. and Yamada, T.: A hierarchy of turbulence closure models for planetary boundary layers, J. Atmos. Sci., 31, 1791–1806, 1974.

Miller, M. J., Palmer, T. N., and Swinbank, R.: Parametrization and influence of subgrid-scale orography in general circulation and numerical weather prediction models, Meteorol. Atmos. Phys., 40, 84–109, doi: 10.1007/BF01027469, 1989.

Mlawer, E. J., Taubman, S. J., Brown, P. D., Iacono, M. J., and Clough, S. A.: Radiative transfer for inhomogeneous atmospheres: RRTM, a validated correlated-*k* model for the longwave, J. Geophys. Res. Atmos., 102, 16 663–16 682, doi: 10.1029/97JD00237, 1997.

Molod, A.: Constraints on the profiles of total water PDF in AGCMs from AIRS and a high-resolution model, J. Climate, 25, 8341–8352, doi: 10.1175/JCLI-D-11-00412.1, 2012.

Molod, A., Takacs, L., Suarez, M., and Bacmeister, J.: Development of the GEOS-5 atmospheric general circulation model: evolution from MERRA to MERRA2, Geosci. Model Dev., 8, 1339–1356, doi: 10.5194/gmd-8-1339-2015, 2015.

Moninger, W. R., Mamrosh, R. D., and Pauley, P. M.: Automated meteorological reports from commercial aircraft, Bull. Am. Meteor. Soc., 84, 203–216, doi: 10.1175/BAMS-84-2-203, 2003.

Moorthi, S. and Suarez, M. J.: Relaxed Arakawa-Schubert. A parameterization of moist convection for general circulation models, Mon. Wea. Rev., 120, 978–1002, 1992.

Moorthi, S., Pan, H.-L., and Caplan, P.: Changes to the 2001 NCEP operational MRF/AVN global analysis/forecast system, Technical Procedures Bulletin, No. 484, NOAA National Weather Service, Silver Spring, MD, 14 pp., available at https://rda.ucar.edu/datasets/ds093.0/docs/ (accessed August 2018), 2001.

Moorthi, S., Sun, R., Xiao, H., and Mechoso, C. R.: Low-cloud simulation in the Southeast Pacific in the NCEP GFS: Role of vertical mixing and shallow convection, NCEP Office Note 463, 28 pp., available at http://www.emc.ncep.noaa.gov/officenotes/FullTOC.html (accessed August 2018), 2010.

Morcrette, J.-J., Barker, H. W., Cole, J. N. S., Iacono, M. J., and Pincus, R.: Impact of a new radiation package, McRad, in the ECMWF Integrated Forecasting System, Mon. Wea. Rev., 136, 4773–4798, doi: 10.1175/2008MWR2363.1, 2008.

Murai, S., Yabu, S., and Kitagawa, H.: Development of a new radiation scheme for the global atmospheric NWP model, American Meteorological Society 21st Conference on Weather Analysis and Forecasting and 17th Conference on Numerical Weather Prediction, 1–5 August 2005, Washington D.C., 5 pp., available at https://ams.confex.com/ams/pdfpapers/94316.pdf (accessed November 2019), 2005.

Nash, J. and Saunders, R.: A review of Stratospheric Sounding Unit radiance observations for climate trends and reanalyses, Q. J. Roy. Meteor. Soc., 141, 2103–2113, doi: 10.1002/qj.2505, 2015.

Nash, J., Oakley, T., Vömel, H., and Li, W.: WMO intercomparison of high quality radiosonde systems, Yangjiang, China, 12 July–3 August 2010, Instruments and Observing Methods Report No. 107, WMO/TD-No. 1580, 238 pp., available at

http://www.wmo.int/pages/prog/www/IMOP/publications-IOM-series.html (accessed August 2018), 2011.

Nieuwstadt, F. T. M.: The turbulent structure of the stable, nocturnal boundary layer, J. Atmos. Sci., 41, 2202–2216, 1984.

Onogi, K.: A data quality control method using forecasted horizontal gradient and tendency in a NWP system, J. Meteorol. Soc. Jpn., 76, 497–516, doi: 10.2151/jmsj1965.76.4_497, 1998.

Onogi, K., Tsutsui, J., Koide, H., Sakamoto, M., Kobayashi, S., Hatsushika, H., Matsumoto, T., Yamazaki, N., Kamahori, H., Takahashi, K., Kadokura, S., Wada, K., Kato, K., Oyama, R., Ose, T., Mannoji, N., and Taira, R.: The JRA-25 Reanalysis, J. Meteorol. Soc. Jpn., 85, 369–432, doi: 10.2151/jmsj.85.369, 2007.

Orbe, C., Oman, L. D., Strahan, S. E., Waugh, D. W., Pawson, S., Takacs, L. L., and Molod, A. M.: Large-scale atmospheric transport in GEOS replay simulations, J. Adv. Model. Earth Syst., 9, 2545–2560, doi: 10.1002/2017MS001053, 2017.

Orr, A., Bechtold, P., Scinocca, J., Ern, M., and Janiskova, M.: Improved middle atmosphere climate and forecasts in the ECMWF model through a nonorographic gravity wave drag parameterization, J. Climate, 23, 5905–5926, doi: 10.1175/2010JCLI3490.1, 2010.

Orsolini, Y. J. and Kvamstø, N. G.: Role of Eurasian snow cover in wintertime circulation: Decadal simulations forced with satellite observations, J. Geophys. Res. Atmos., 114, D19108, doi: 10.1029/2009JD012253, 2009.

Osborn, T. J. and Jones, P. D.: The CRUTEM4 land-surface air temperature data set: construction, previous versions and dissemination via Google Earth, Earth Syst. Sci. Data, 6, 61–68, doi: 10.5194/essd-6-61-2014, 2014.

Palmer, T. N., Shutts, G. J., and Swinbank, R.: Alleviation of a systematic westerly bias in general circulation and numerical weather prediction models through an orographic gravity wave drag parametrization, Q. J. Roy. Meteor. Soc., 112, 1001–1039, doi: 10.1002/qj.49711247406, 1986.

Paltridge, G. W. and Platt, C. M. R.: Radiative Processes in Meteorology and Climatology, Elsevier, New York, 336 pp., 1976.

Pan, H.-L. and Mahrt, L.: Interaction between soil hydrology and boundary-layer development, Bound.-Lay. Meteorol., 38, 185–202, doi: 10.1007/BF00121563, 1987.

Pan, H.-L. and Wu, W.: Implementing a mass flux convective parameterization package for the NMC Medium-Range Forecast model, NMC Office Note 409, 43 pp., available at http://www.emc.ncep.noaa.gov/officenotes/FullTOC.html (accessed August 2018), 1995.

Park, S. K. and Županski, D.: Four-dimensional variational data assimilation for mesoscale and storm-scale applications, Meteorol. Atmos. Phys., 82, 173–208, doi: 10.1007/s00703-001-0586-7, 2003.

Parrish, D. F. and Derber, J. C.: The National Meteorological Center's Spectral Statistical-Interpolation analysis system, Mon. Wea. Rev., 120, 1747–1763, 1992.

Petersen, R. A.: On the impact and benefits of AMDAR observations in operational forecasting – part I: a review of the impact of automated aircraft wind and temperature reports, Bull. Am. Meteor. Soc., 97, 585–602, doi: 10.1175/BAMS-D-14-00055.1, 2016.

Pierrehumbert, R. T.: An essay on the parameterization of orographic gravity wave drag, Seminar/Workshop on Observation, Theory and Modelling of Orographic Effects. 15-20 September 1986, ECMWF, Shinfield Park, Reading, UK, available at https://www.ecmwf.int/en/elibrary/11673-essay-parameterization-orographic-gravity-wave-drag (accessed August 2018), 1986.

Pincus, R., Barker, H. W., and Morcrette, J.-J.: A fast, flexible, approximate technique for computing radiative transfer in inhomogeneous cloud fields, J. Geophys. Res. Atmos., 108, 4376, doi: 10.1029/2002JD003322, 2003.

Polavarapu, S. and Pulido, M.: Stratospheric and mesospheric data assimilation: the role of middle atmospheric dynamics, in: Data Assimilation for Atmospheric, Oceanic and Hydrologic Applications (Vol. III), edited by Park, S. K. and Xu, L., pp. 429–454, Springer International Publishing, Cham, doi: 10.1007/978-3-319-43415-5_19, 2017.

Polavarapu, S., Shepherd, T. G., Rochon, Y., and Ren, S.: Some challenges of middle atmosphere data assimilation, Q. J. Roy. Meteor. Soc., 131, 3513–3527, doi: 10.1256/qj.05.87, 2005.

Poli, P., Healy, S. B., and Dee, D. P.: Assimilation of Global Positioning System radio occultation data in the ECMWF ERA-Interim reanalysis, Q. J. Roy. Meteor. Soc., 136, 1972–1990, doi: 10.1002/qj.722, 2010.

Poli, P., Hersbach, H., Tan, D. G. H., Dee, D. P., Thépaut, J.-N., Simmons, A., Peubey, C., Laloyaux, P., Komori, T., Berrisford, P., Dragani, R., Trémolet, Y., Hólm, E. V., Bonavita, M., Isaksen, L., and Fisher, M.: An essay on the parameterization of orographic gravity wave drag, ERA Report Series, No. 14, ECMWF, Shinfield Park, Reading, UK, available at https://www.ecmwf.int/en/elibrary/11699-data-assimilation-system-and-initial-performance-evaluation-ecmwf-pilot-reanalysis (accessed August 2018), 2013.

Poli, P., Hersbach, H., Dee, D. P., Berrisford, P., Simmons, A. J., Vitart, F., Laloyaux, P., Tan, D. G. H., Peubey, C., Thpaut, J.-N., Trmolet, Y., Hlm, E. V., Bonavita, M., Isaksen, L., and Fisher, M.: ERA-20C: An atmospheric reanalysis of the twentieth century, J. Climate, 29, 4083–4097, doi: 10.1175/JCLI-D-15-0556.1, 2016.

Putman, W. M. and Lin, S.-J.: Finite-volume transport on various cubed-sphere grids, J. Comput. Phys., 227, 55–78, doi: 10.1016/j.jcp.2007.07.022, 2007.

Randel, W., Udelhofen, P., Fleming, E., Geller, M., Gelman, M., Hamilton, K., Karoly, D., Ortland, D., Pawson, S., Swinbank, R., Wu, F., Baldwin, M., Chanin, M.-L., Keckhut, P., Labitzke, K., Remsberg, E., Simmons, A., and Wu, D.: The SPARC intercomparison of middle-atmosphere climatologies, J. Climate, 17, 986–1003, 2004.

Randles, C. A., da Silva, A. M., Buchard, V., Colarco, P. R., Darmenov, A., Govindaraju, R., Smirnov, A., Holben, B., Ferrare, R., Hair, J., Shinozuka, Y., and Flynn, C. J.: The MERRA-2 Aerosol Reanalysis, 1980 onward. Part I: system description and data assimilation evaluation, J. Climate, 30, 6823–6850, doi: 10.1175/JCLI-D-16-0609.1, 2017.

Reale, A. L.: NOAA operational sounding products from Advanced-TOVS polar orbiting environmental satellites, NOAA Technical Report NESDIS 102, Washington, DC, 59 pp., available at https://repository.library.noaa.gov/view/noaa/1123 (accessed August 2018), 2001.

Reichle, R. H., Koster, R. D., De Lannoy, G. J. M., Forman, B. A., Liu, Q., Mahanama, S. P. P., and Touré, A.: Assessment and enhancement of MERRA land surface hydrology estimates, J. Climate, 24, 6322–6338, doi: 10.1175/JCLI-D-10-05033.1, 2011.

Reichle, R. H., Draper, C. S., Liu, Q., Girotto, M., Mahanama, S. P. P., Koster, R. D., and De Lannoy, G. J. M.: Assessment of MERRA-2 land surface hydrology estimates, J. Climate, 30, 2937–2960, doi: 10.1175/JCLI-D-16-0720.1, 2017a.

Reichle, R. H., Liu, Q., Koster, R. D., Draper, C. S., Mahanama, S. P. P., and Partyka, G. S.: Land surface precipitation in MERRA-2, J. Climate, 30, 1643–1664, doi: 10.1175/JCLI-D-16-0570.1, 2017b.

Reynolds, R. W. and Smith, T. M.: Improved global sea surface temperature analyses using optimum interpolation, J. Climate, 7, 929–948, 1994.

Reynolds, R. W., Rayner, N. A., Smith, T. M., Stokes, D. C., and Wang, W.: An improved in situ and satellite SST analysis for climate, J. Climate, 15, 1609–1625, 2002.

Reynolds, R. W., Smith, T. M., Liu, C., Chelton, D. B., Casey, K. S., and Schlax, M. G.: Daily high-resolution-blended analyses for sea surface temperature, J. Climate, 20, 5473–5496, doi: 10.1175/2007JCLI1824.1, 2007.

Riehl, H. and Malkus, J. S.: On the heat balance in the equatorial trough zone, Geophysica, 6, 503–538, 1958.

Rienecker, M. M., Suarez, M. J., Todling, R., Bacmeister, J., Takacs, L., Liu, H.-C., Gu, W., Sienkiewicz, M., Koster, R. D., Gelaro, R., Stajner, I., and Nielsen, J. E.: The GEOS-5 Data Assimilation System—Documentation of versions 5.0.1 and 5.1.0, and 5.2.0, Technical Report Series on Global Modeling and Data Assimilation, No. 27, NASA/TM-2008-104606, Greenbelt, Maryland, 92 pp., available at https://ntrs.nasa.gov/search.jsp?R=20120011955 (accessed August 2018), 2008.

Rienecker, M. M., Suarez, M. J., Gelaro, R., Todling, R., Bacmeister, J., Liu, E., Bosilovich, M. G., Schubert, S. D., Takacs, L., Kim, G.-K., Bloom, S., Chen, J., Collins, D., Conaty, A., da Silva, A., Gu, W., Joiner, J., Koster, R. D., Lucchesi, R., Molod, A., Owens, T., Pawson, S., Pegion, P., Redder, C. R., Reichle, R., Robertson, F. R., Ruddick, A. G., Sienkiewicz, M., and Woollen, J.: MERRA: NASAs Modern-Era Retrospective Analysis for Research and Applications, J. Climate, 24, 3624–3648, doi: 10.1175/JCLI-D-11-00015.1, 2011.

Rosenfield, J. E., Schoeberl, M. R., and Geller, M. A.: A computation of the stratospheric diabatic circulation using an accurate radiative transfer model, J. Atmos. Sci., 44, 859–876, 1987.

Saha, S., Moorthi, S., Pan, H.-L., Wu, X., Wang, J., Nadiga, S., Tripp, P., Kistler, R., Woollen, J., Behringer, D., Liu, H., Stokes, D., Grumbine, R., Gayno, G., Wang, J., Hou, Y.-T., Chuang, H.-y., Juang, H.-M. H., Sela, J., Iredell, M., Treadon, R., Kleist, D., Van Delst, P., Keyser, D., Derber, J., Ek, M., Meng, J., Wei, H., Yang, R., Lord, S., van den Dool, H., Kumar, A., Wang, W., Long, C., Chelliah, M., Xue, Y., Huang, B., Schemm, J.-K., Ebisuzaki, W., Lin, R., Xie, P., Chen, M., Zhou, S., Higgins, W., Zou, C.-Z., Liu, Q., Chen, Y., Han, Y., Cucurull, L., Reynolds, R. W., Rutledge, G., and Goldberg, M.: The NCEP Climate Forecast System Reanalysis, Bull. Am. Meteor. Soc., 91, 1015–1058, doi: 10.1175/2010BAMS3001.1, 2010.

Saha, S., Moorthi, S., Wu, X., Wang, J., Nadiga, S., Tripp, P., Behringer, D., Hou, Y.-T., Chuang, H.-y., Iredell, M., Ek, M., Meng, J., Yang, R., Mendez, M. P., van den Dool, H., Zhang, Q., Wang, W., Chen, M., and Becker, E.: The NCEP Climate Forecast System Version 2, J. Climate, 27, 2185–2208, doi: 10.1175/JCLI-D-12-00823.1, 2014.

Sakamoto, M. and Christy, J. R.: The influences of TOVS radiance assimilation on temperature and moisture tendencies in JRA-25 and ERA-40, J. Atmos. Ocean. Tech., 26, 1435–1455, doi: 10.1175/2009JTECHA1193.1, 2009.

Sankey, D., Ren, S., Polavarapu, S., Rochon, Y. J., Nezlin, Y., and Beagley, S.: Impact of data assimilation filtering methods on the mesosphere, J. Geophys. Res. Atmos., 112, D24104, doi: 10.1029/2007JD008885, 2007.

Sato, M., Hansen, J. E., McCormick, M. P., and Pollack, J. B.: Stratospheric aerosol optical depths, 1850–1990, J. Geophys. Res. Atmos., 98, 22 987–22 994, doi: 10.1029/93JD02553, 1993.

Sato, N., Sellers, P., Randall, D., Schneider, E., Shukla, J., Kinter, J., Hou, Y.-T., and Albertazzi, E.: Effects of implementing the Simple Biosphere model in a general circulation model, J. Atmos. Sci., 46, 2757–2782, 1989.

Schoeberl, M. R., Douglass, A. R., Zhu, Z., and Pawson, S.: A comparison of the lower stratospheric age spectra derived from a general circulation model and two data assimilation systems, J. Geophys. Res. Atmos., 108, 4113, doi: 10.1029/2002JD002652, 2003.

Schubert, S. D., Rood, R. B., and Pfaendtner, J.: An assimilated dataset for Earth science applications, Bull. Am. Meteor. Soc., 74, 2331–2342, 1993.

Schubert, S. D., Park, C.-K., Wu, C.-Y., Higgins, W., Kondratyeva, Y., Molod, A., Takacs, L. L., Seablom, M., and Rood, R. B.: A multiyear assimilation with the GEOS-1 system: Overview and results, Technical Report Series on Global Modeling and Data Assimilation, No. 6, NASA/TM-104606, Greenbelt, Maryland, 201 pp., available at https://ntrs.nasa.gov/search.jsp?R=19950020003 (accessed August 2018), 1995.

Schwarzkopf, M. D. and Fels, S. B.: The simplified exchange method revisited: an accurate, rapid method for computation of infrared cooling rates and fluxes, J. Geophys. Res. Atmos., 96, 9075–9096, doi: 10.1029/89JD01598, 1991.

Scinocca, J. F.: An accurate spectral nonorographic gravity wave drag parameterization for general circulation models, J. Atmos. Sci., 60, 667–682, 2003.

Seidel, D. J., Berger, F. H., Diamond, H. J., Dykema, J., Goodrich, D., Immler, F., Murray, W., Peterson, T., Sisterson, D., Sommer, M., Thorne, P., Vömel, H., and Wang, J.: Reference upper-air observations for climate: rationale, progress, and plans, Bull. Am. Meteor. Soc., 90, 361–369, doi: 10.1175/2008BAMS2540.1, 2009.

Sellers, P. J., Mintz, Y., Sud, Y. C., and Dalcher, A.: A Simple Biosphere model (SIB) for use within general circulation models, J. Atmos. Sci., 43, 505–531, 1986.

Shepherd, T. G. and Shaw, T. A.: The angular momentum constraint on climate sensitivity and downward influence in the middle atmosphere, J. Atmos. Sci., 61, 2899–2908, doi: 10.1175/JAS-3295.1, 2004.

Shepherd, T. G., Semeniuk, K., and Koshyk, J. N.: Sponge layer feedbacks in middle-atmosphere models, J. Geophys. Res. Atmos., 101, 23 447–23 464, doi: 10.1029/96JD01994, 1996.

Simmons, A. J. and Burridge, D. M.: An energy and angular-momentum conserving vertical finite-difference scheme and hybrid vertical coordinates, Mon. Wea. Rev., 109, 758–766, 1981.

Simmons, A. J., Jones, P. D., da Costa Bechtold, V., Beljaars, A. C. M., Kållberg, P. W., Saarinen, S., Uppala, S. M., Viterbo, P., and Wedi, N.: Comparison of trends and low-frequency variability in CRU, ERA-40, and NCEP/NCAR analyses of surface air temperature, J. Geophys. Res. Atmos., 109, D24115, doi: 10.1029/2004JD005306, 2004.

Simmons, A. J., Poli, P., Dee, D. P., Berrisford, P., Hersbach, H., Kobayashi, S., and Peubey, C.: Estimating low-frequency variability and trends in atmospheric temperature using ERA-Interim, Q. J. Roy. Meteor. Soc., 140, 329–353, doi: 10.1002/qj.2317, 2014.

Smith, R. N. B.: A scheme for predicting layer clouds and their water content in a general circulation model, Q. J. Roy. Meteor. Soc., 116, 435–460, doi: 10.1002/qj.49711649210, 1990.

Sommeria, G. and Deardorff, J. W.: Subgrid-scale condensation in models of nonprecipitating clouds, J. Atmos. Sci., 34, 344–355, 1977.

Spencer, J. W.: Fourier series representation of the position of the sun, Search, 2, 172, available at https://www.mail-archive.com/sundial@uni-koeln.de/msg01050.html (accessed August 2018), 1971.

Stajner, I., Wargan, K., Pawson, S., Hayashi, H., Chang, L.-P., Hudman, R. C., Froidevaux, L., Livesey, N., Levelt, P. F., Thompson, A. M., Tarasick, D. W., Stübi, R., Andersen, S. B., Yela, M., König-Langlo, G., Schmidlin, F. J., and Witte, J. C.: Assimilated ozone from EOS-Aura: evaluation of the tropopause region and tropospheric columns, J. Geophys. Res. Atmos., 113, D16S32, doi: 10.1029/2007JD008863, 2008.

Stieglitz, M., Ducharne, A., Koster, R., and Suarez, M.: The impact of detailed snow physics on the simulation of snow cover and subsurface thermodynamics at continental scales, J. Hydrometeorol., 2, 228–242, 2001.

Sundqvist, H.: A parameterization scheme for non-convective condensation including prediction of cloud water content, Q. J. Roy. Meteor. Soc., 104, 677–690, doi: 10.1002/qj.49710444110, 1978.

Takacs, L. L., Suarez, M. J., and Todling, R.: Maintaining atmospheric mass and water balance within reanalysis, Technical Report Series on Global Modeling and Data Assimilation, No. 37, NASA/TM-2014-104606, Greenbelt, Maryland, 46 pp., available at https://ntrs.nasa.gov/search.jsp?R=20150007977 (accessed August 2018), 2015.

Talagrand, O.: Variational assimilation, in: Data Assimilation: Making Sense of Observations, edited by Lahoz, W., Khattatov, B., and Menard, R., pp. 41–67, Springer–Verlag, Berlin, doi: 10.1007/978-3-540-74703-1_3, 2010.

Tan, W. W., Geller, M. A., Pawson, S., and da Silva, A.: A case study of excessive subtropical transport in the stratosphere of a data assimilation system, J. Geophys. Res. Atmos., 109, D11102, doi: 10.1029/2003JD004057, 2004.

Tanré, D., Geleyn, J.-F., and Slingo, J. M.: First results of the introduction of an advanced aerosol-radiation interaction in the ECMWF low resolution global model, in: Aerosols and their Climatic Effects, edited by Gerber, H. E. and Deepak, A., pp. 133–177, Deepak Publishing, Hampton, VA, USA, 1984.

Tavolato, C. and Isaksen, L.: Data usage and quality control for ERA-40, ERA-Interim and the operational ECMWF data assimilation system, ERA Report Series, No. 7, ECMWF, Shinfield Park, Reading, UK, 43 pp., available at https://www.ecmwf.int/en/elibrary/12573-data-usage-and-quality-control-era-40-era-interim-and-operational-ecmwf-data (accessed August 2018), 2011.

Taylor, K. E., Williamson, D., and Zwiers, F.: The sea surface temperature and sea ice concentration boundary conditions for AMIP II simulations, Program for Climate Model Diagnosis and Intercomparison (PCMDI) Report 60, Lawrence Livermore National Laboratory, available at https://pcmdi.llnl.gov/mips/amip (accessed August 2018), 2000.

Tegen, I., Hollrig, P., Chin, M., Fung, I., Jacob, D., and Penner, J.: Contribution of different aerosol species to the global aerosol extinction optical thickness: estimates from model results, J. Geophys. Res. Atmos., 102, 23 895–23 915, doi: 10.1029/97JD01864, 1997.

Tiedtke, M.: A comprehensive mass flux scheme for cumulus parameterization in large-scale models, Mon. Wea. Rev., 117, 1779–1800, 1989.

Tiedtke, M.: Representation of clouds in large-scale models, Mon. Wea. Rev., 121, 3040–3061, 1993.

Titchner, H. A. and Rayner, N. A.: The Met Office Hadley Centre sea ice and sea surface temperature data set, version 2: 1. Sea ice concentrations, J. Geophys. Res. Atmos., 119, 2864–2889, doi: 10.1002/2013JD020316, 2014.

Tompkins, A. M., Gierens, K., and Rädel, G.: Ice supersaturation in the ECMWF integrated forecast system, Q. J. Roy. Meteor. Soc., 133, 53–63, doi: 10.1002/qj.14, 2007.

Troen, I. B. and Mahrt, L.: A simple model of the atmospheric boundary layer; sensitivity to surface evaporation, Bound.-Lay. Meteorol., 37, 129–148, doi: 10.1007/BF00122760, 1986.

Tsuyuki, T. and Miyoshi, T.: Recent progress of data assimilation methods in meteorology, J. Meteorol. Soc. Jpn., 85B, 331–361, doi: 10.2151/jmsj.85B.331, 2007.

Uppala, S. M., Kllberg, P. W., Simmons, A. J., Andrae, U., Bechtold, V. D. C., Fiorino, M., Gibson, J. K., Haseler, J., Hernandez, A., Kelly, G. A., Li, X., Onogi, K., Saarinen, S., Sokka, N., Allan, R. P., Andersson, E., Arpe, K., Balmaseda, M. A., Beljaars, A. C. M., Berg, L. V. D., Bidlot, J., Bormann, N., Caires, S., Chevallier, F., Dethof, A., Dragosavac, M., Fisher, M., Fuentes, M., Hagemann, S., Hlm, E., Hoskins, B. J., Isaksen, L., Janssen, P. A. E. M., Jenne, R., Mcnally, A. P., Mahfouf, J.-F., Morcrette, J.-J., Rayner, N. A., Saunders, R. W., Simon, P., Sterl, A., Trenberth, K. E., Untch, A., Vasiljevic, D., Viterbo, P., and Woollen, J.: The ERA-40 re-analysis, Q. J. Roy. Meteor. Soc., 131, 2961–3012, doi: 10.1256/qj.04.176, 2005.

USGS: Global land cover characteristics data base, version 2.0, available at https://lta.cr.usgs.gov/glcc/globdoc2_0 (accessed August 2018), 2000.

van den Hurk, B. J. J., Viterbo, P., Beljaars, A., and Betts, A.: Offline validation of the ERA40 surface scheme, Technical Memorandum 295, ECMWF, Shinfield Park, Reading, UK, available at https://www.ecmwf.int/en/elibrary/12900-offline-validation-era40-surface-scheme (accessed August 2018), 2000.

van Vuuren, D. P., Edmonds, J., Kainuma, M., Riahi, K., Thomson, A., Hibbard, K., Hurtt, G. C., Kram, T., Krey, V., Lamarque, J.-F., Masui, T., Meinshausen, M., Nakicenovic, N., Smith, S. J., and Rose, S. K.: The representative concentration pathways: an overview, Clim. Change, 109, 5, doi: 10.1007/s10584-011-0148-z, 2011.

Walsh, J. E. and Chapman, W. L.: 20th-century sea-ice variations from observational data, Ann. Glaciol., 33, 444–448, doi: 10.3189/172756401781818671, 2001.

Wang, L., Zou, C.-Z., and Qian, H.: Construction of stratospheric temperature data records from Stratospheric Sounding Units, J. Climate, 25, 2931–2946, doi: 10.1175/JCLI-D-11-00350.1, 2012.

Wargan, K., Labow, G., Frith, S., Pawson, S., Livesey, N., and Partyka, G.: Evaluation of the ozone fields in NASAs MERRA-2 reanalysis, J. Climate, 30, 2961–2988, doi: 10.1175/JCLI-D-16-0699.1, 2017.

Whitaker, J. S., Compo, G. P., and Thépaut, J.-N.: A comparison of variational and ensemble-based data assimilation systems for reanalysis of sparse observations, Mon. Wea. Rev., 137, 1991–1999, doi: 10.1175/2008MWR2781.1, 2009.

WMO: A preliminary cloudless standard atmosphere for radiation computation, world Climate Programme (WCP), 112, 53 pp., 1986.

Woodruff, S. D., Worley, S. J., Lubker, S. J., Ji, Z., Eric Freeman, J., Berry, D. I., Brohan, P., Kent, E. C., Reynolds, R. W., Smith, S. R., and Wilkinson, C.: ICOADS Release 2.5: extensions

and enhancements to the surface marine meteorological archive, Int. J. Climatol., 31, 951–967, doi: 10.1002/joc.2103, 2011.

Wright, J.: S-RIP: Zonal-mean heating rates of global atmospheric reanalyses on pressure levels, doi: 10.5285/70146c789eda4296a3c3ab6706931d56, URL http://catalogue.ceda.ac.uk/uuid/70146c789eda4296a3c3ab6706931d56, 2017.

Wright, J. S. and Fueglistaler, S.: Large differences in reanalyses of diabatic heating in the tropical upper troposphere and lower stratosphere, Atmos. Chem. Phys., 13, 9565–9576, doi: 10.5194/acp-13-9565-2013, 2013.

Xie, S. and Zhang, M.: Impact of the convection triggering function on single-column model simulations, J. Geophys. Res. Atmos., 105, 14 983–14 996, doi: 10.1029/2000JD900170, 2000.

Xu, K.-M. and Krueger, S. K.: Evaluation of cloudiness parameterizations using a cumulus ensemble model, Mon. Wea. Rev., 119, 342–367, 1991.

Xu, K.-M. and Randall, D. A.: A semiempirical cloudiness parameterization for use in climate models, J. Atmos. Sci., 53, 3084–3102, 1996a.

Xu, K.-M. and Randall, D. A.: Evaluation of statistically based cloudiness parameterizations used in climate models, J. Atmos. Sci., 53, 3103–3119, 1996b.

Zhao, Q. and Carr, F. H.: A prognostic cloud scheme for operational NWP models, Mon. Wea. Rev., 125, 1931–1953, 1997.

Zou, C.-Z. and Qian, H.: Stratospheric temperature climate data record from merged SSU and AMSU-A observations, J. Atmos. Ocean Tech., 33, 1967–1984, doi: 10.1175/JTECH-D-16-0018.1, 2016.

Zou, C.-Z. and Wang, W.: Intersatellite calibration of AMSU-A observations for weather and climate applications, J. Geophys. Res. Atmos., 116, D23113, doi: 10.1029/2011JD016205, 2011.

Zou, C.-Z., Goldberg, M. D., Cheng, Z., Grody, N. C., Sullivan, J. T., Cao, C., and Tarpley, D.: Recalibration of microwave sounding unit for climate studies using simultaneous nadir overpasses, J. Geophys. Res. Atmos., 111, D19114, doi: 10.1029/2005JD006798, 2006.

Zou, C.-Z., Qian, H., Wang, W., Wang, L., and Long, C.: Recalibration and merging of SSU observations for stratospheric temperature trend studies, J. Geophys. Res. Atmos., 119, 13 180–13 205, doi: 10.1002/2014JD021603, 2014.